ACTIVE STEREO VISION: DEPTH PERCEPTION FOR NAVIGATION, ENVIRONMENTAL MAP FORMATION AND OBJECT RECOGNITION

A THESIS SUBMITTED TO
THE GRADUATE SCHOOL OF NATURAL AND APPLIED SCIENCES
OF
THE MIDDLE EAST TECHNICAL UNIVERSITY

BY

İLKAY ULUSOY

IN PARTIAL FULLFILLMENT OF THE REQUIREMENTS FOR THE

DEGREE OF

DOCTOR OF PHILOSOPHY

IN

THE DEPARTMENT OF ELECTRICAL AND ELECTRONICS

ENGINEERING

SEPTEMBER 2003

Approval of the Graduate School of Natural and Applied Sciences

_____

Prof. Dr. Canan Özgen
Director

I certify that this thesis satisfies all the requirements as a thesis for the degree of Doctor of Philosophy.

_____

Prof. Dr. Mübeccel Demirekler
Head of Department

This is to certify that we have read this thesis and that in our opinion it is fully adequate, in scope and quality, as a thesis for the degree of Doctor of Philosophy.

_____

Prof. Dr. Uğur Halıcı
Supervisor

Examining Committee Members

Prof. Dr. Kemal Leblebicioğlu _____

Prof. Dr. Uğur Halıcı _____

Prof. Dr. Hasan Güran _____

Assoc. Prof. Dr. Volkan Atalay _____

Prof. Dr. Erhan Nalçacı _____

ABSTRACT

ACTIVE STEREO VISION: DEPTH PERCEPTION FOR NAVIGATION, ENVIRONMENTAL MAP FORMATION AND OBJECT RECOGNITION

Ulusoy, İlkay

Ph. D., Department of Electrical and Electronics Engineering

Supervisor: Prof. Dr. Uğur Halıcı

September 2003, 148 pages

In very few mobile robotic applications stereo vision based navigation and mapping is used because dealing with stereo images is very hard and very time consuming. Despite all the problems, stereo vision still becomes one of the most important resources of knowing the world for a mobile robot because imaging provides much more information than most other sensors. Real robotic applications are very complicated because besides the problems of finding how the robot should behave to complete the task at hand, the problems faced while controlling the robot's internal parameters bring high computational load. Thus, finding the strategy to be followed in a simulated world and then applying this on real robot for real applications is preferable. In this study, we describe an algorithm for object

recognition and cognitive map formation using stereo image data in a 3D virtual world where 3D objects and a robot with active stereo imaging system are simulated. Stereo imaging system is simulated so that the actual human visual system properties are parameterized. Only the stereo images obtained from this world are supplied to the virtual robot. By applying our disparity algorithm, depth map for the current stereo view is extracted. Using the depth information for the current view, a cognitive map of the environment is updated gradually while the virtual agent is exploring the environment. The agent explores its environment in an intelligent way using the current view and environmental map information obtained up to date. Also, during exploration if a new object is observed, the robot turns around it, obtains stereo images from different directions and extracts the model of the object in 3D. Using the available set of possible objects, it recognizes the object.

Keywords: stereo vision, active vision, disparity, depth perception, environmental map, object recognition

ÖZ

AKTİF STEREO GÖRME: İLERLEME, ÇEVRESEL HARİTA ÇIKARMA VE NESNE TANIMA AMAÇLARI İÇİN DERİNLİK ALGILANMASI

Ulusoy, İlkay

Doktora, Elektrik ve Elektronik Mühendisliği Bölümü

Tez Yöneticisi: Prof. Dr. Uğur Halıcı

Eylul 2003, 148 sayfa

Stereo görme analizi çok zor ve zaman alıcı olduğu için, robot çalışmalarında çok sık tercih edilen bir yöntem değildir. Buna rağmen, hareketli bir robot için çevrenin daha detaylı bilinmesi açısından stereo görüntüleme en temel kaynak olarak tercih edilmeye başlanmıştır. Bunun en temel nedeni, görüntülemenin analizi çok zor olmasına rağmen diğer sensörlere nazaran çok daha fazla bilgi sağlıyor olmasıdır. Gerçek robot uygulamaları çok karmaşıktır. Bu nedenle, robotun nasıl davranması gerektiğinin bulunması amaçlanıyorsa öncelikle simülasyonlar üzerinde çalışıp daha sonra bulunan stratejinin gerçek robot üzerinde uygulanması tercih edilen bir yöntemdir. Bu çalışmada, üç boyutlu sanal bir ortam oluşturulmuştur. Bu sanal ortamda üç boyutlu nesneler ve aktif stereo görme sistemine sahip sanal bir robot

yer almaktadır. Bu sanal ortamdan alınan stereo görüntüler kullanılarak sanal robotun nesne tanıması ve çevresel harita çıkarması hedeflenmiştir. Stereo görüntüleme sistemi, gerçek insan görme sistemi özelliklerine göre simüle edilmiştir. Sanal robot, sadece stereo görüntüleri kullanmaktadır. Farklılık algoritmamız kullanılarak stereo görüntülerden o anki görme alanı için derinlik bilgisi çıkarılmaktadır. Robot akıllı bir şekilde etrafı tararken, derinlik bilgisi kullanılarak kognitif harita sürekli doldurulmaktadır. Robot, ortamda ilerlemeyi o anki görsel bilgi ve o ana kadar oluşturulmuş kognitif harita yardımıyla gerçekleştirmektedir. Aynı zamanda robot, ortamda dolaşırken yeni bir nesne ile karşılaşırsa, nesnenin etrafında dönerek farklı yönlerden stereo görüntüsünü çekmekte ve üç boyutlu modelini çıkarmaktadır. Daha önceden tanımlanmış olabilecek nesneler arasından, görmüş olduğu nesneyi üç boyutlu yapı bilgisinden çıkarmaktadır.

Anahtar Kelimeler: stereo görme, aktif görme, farklılık, derinlik algısı, çevresel harita çıkarmak, nesne tanıma

To My Father, Mother, Brother and Lovely Daughter

ACKNOWLEDGEMENTS

I would like to express my gratitude to my supervisor Prof. Dr. Uğur Halıcı for her guidance and support throughout the research. I would also like to thank to Prof. Dr. Kemal Leblebicioğlu, Asst. Prof. Dr. Volkan Atalay and Prof. Dr. Edwin Hancock for their contributions.

I would like to acknowledge TUBİTAK-BAYG for the scholarship that covered my studies at the University of York, UK and thank to both my supervisor and TUBİTAK for providing me such a possibility.

TABLE OF CONTENTS

LIST OF FIGURES

FIGURE

LIST OF TABLES

TABLE

CHAPTER 1

INTRODUCTION

1.1 Problem Definition and Motivation

In this thesis the main goal is to develop a biologically inspired stereo vision system and to use this system in a robotic application where human-like activities such as cognitive map formation and object recognition are performed.

Navigation could not be achieved unless distance information is obtained. For other activities of human such as object recognition, shape extraction, etc., some other cues such as silhouette, shading, texture, etc., could also be used but for navigation and localization depth information is crucial.

Although monocular cues, such as previous familiarity, interposition, linear and size perspective, distribution of shadows and illumination and motion parallax, are effective for depth perception (See Appendix A for detailed information about depth perception), for many species with frontally located eyes including humans, binocular disparity provides a powerful and highly quantitative cue to near field (<100 ft) depth perception. Binocular disparity refers to a small positional difference between corresponding images features in the two eyes, and arises because the two eyes are separated horizontally. Depth perception based upon binocular disparities is known as stereopsis.

In many robotics applications depth is usually extracted by proximity sensors such as ultrasound or laser scanners. However, cameras have several desirable

properties compared to these proximity sensors. They are low cost sensors that provide a huge amount of information, they are easy to set-up and they are passive so that vision based navigation systems do not suffer from the interferences often observed when using active sound- or light-based proximity sensors.

For depth extraction, at least a stereo camera system is necessary. However, since dealing with stereo images is very hard and very time consuming, only in some recent mobile robotic applications stereovision is used. In spite of the fact that there are big problems in dealing with stereo images, stereovision is becoming one of the most important resources of knowing the world for a mobile robot. One of the reasons is that although imaging is very difficult to handle, it provides much more information of the world than most other sensors. The other reason is that with recent improvements in the hardware, time consuming applications are becoming faster and easier. Moreover, if robots are deployed in populated environment, it makes sense to base the perceptional skills on vision as humans do [98].

There are some commercial products as been used in [61]. However these require special hardware. Since on-body real-time systems are required for mobile robotics, using only standard PC hardware and simple image capture card system instead of systems which require special hardware is preferred [42].

Higher vertebrates like humans can perform navigation extending beyond sensory horizon. They can make short-cuts and can find other route to destination if the route they are following was blocked. This is called survey navigation and for such navigation some form of spatial representation is necessary. Higher vertebrates appear to construct representations (sometimes referred to as cognitive maps) which encode spatial relations between relevant locations in their environment. Hippocampus is known to be the place in the brain for such a representation. Many studies investigated hippocampus of rat brain and cognitive maps are modeled based on these physiological findings [49].

Real robotic applications are very complicated because besides the problems of finding how the robot should behave to complete the task at hand, the problems

faced while controlling the robot's internal parameters bring high computational load. Thus, first working in a simulated environment in order to find the strategy to be followed by the robot and then applying this on real robotic applications is preferable. Especially intelligent way finding, path planning and mapping algorithms are developed in simulated environments [41, 80, 90, 97, 79, 49]. Biologically inspired active vision system is also implemented in such a virtual environment in [90].

In this study we develop a multi-scale phase based disparity algorithm for the purpose of depth estimation which is very important for human navigation. Since dealing with stereovision and robot control at the same time is very hard, we also apply our stereovision algorithm in a simulated world with simulated cameras and objects where the goal is to construct three dimensional (3D) map of the environment. Then, in the future studies our algorithm can be applied on real robots.

In robotic research various systems for map construction have been proposed. Some uses metric measurements to construct the map. Some only extracts the topology of the environment [88]. Although metric maps suffer from big size, due to accuracy embedded in such maps they provide better localization for the robot. Because of this reason we have chosen grid-based mapping which is also a metric mapping. Some studies prefer robot centered maps versus world centered maps. However, since world centered maps are easier to construct we choose world centered maps. But such maps suffer from movement errors due to slippery and odometry errors, since this kind of errors add up in time. But since we use stereo vision in our map construction algorithm we assume that ego-motion extraction and localization could be performed easily. Thus, world centered maps can be constructed without major error. In our future studies algorithms for ego-motion extraction and localization for stereo-vision will be developed for real robotic applications in natural environments. All these different mapping methods and problems coming with them are explained in Chapter 2. In this thesis we construct a

world centric, grid based cognitive map which is very important for higher vertebrate survey navigation.

Our virtual world is a computer simulation of a very simple 3D environment. In this environment there is an agent which has a stereo imaging system modeled with the properties of human eye. There are also 3D objects each having two parts which are either sphere, ellipsoid, cylinder or cone of any size. Some of the 3D objects are as follows: a sphere on top of a cylinder is an apple tree, a cone on top of a small radius cylinder is a pine tree, a cone on top of a large radius cylinder is a cottage, etc. The agent uses only the stereo image pairs obtained form this virtual world and explores its environment based on some heuristics. It simultaneously builds up a 3D map and recognizes the objects it observes during exploration.

The schema of the complete system is given in Figure 1. Our system is composed of two main modules: 1) Simulation module (SM) where virtual environment exists, 2) Processor module (PM) where all kinds of control activities are achieved. Also, processor module is composed of two sub modules: 1) Map formation and object recognition sub-module, 2) Navigation and camera controller sub-module.

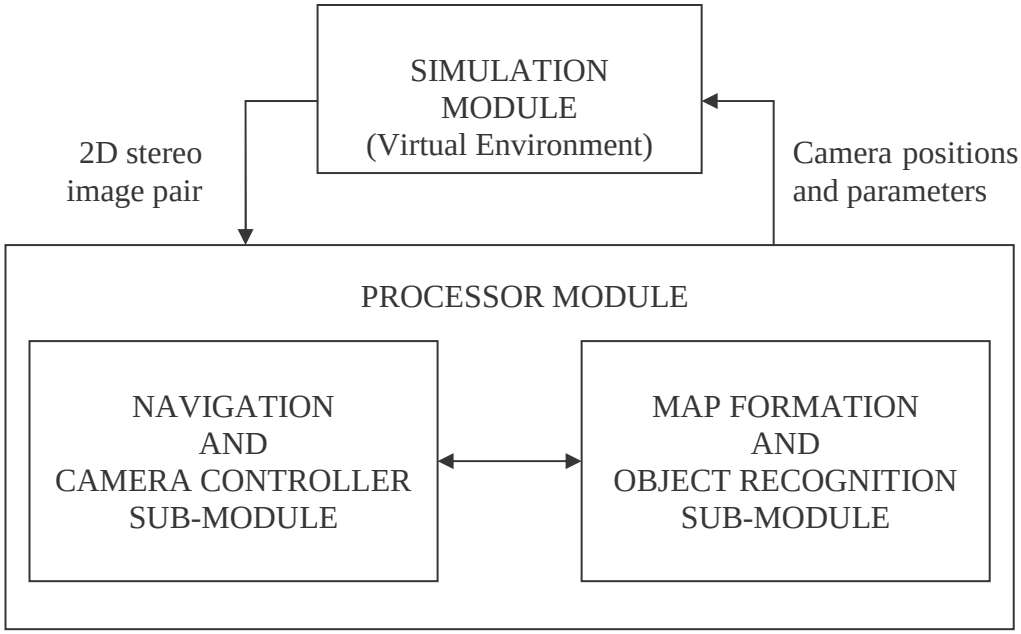

Figure 1 Modules of the whole system.

The system works as follows: First, 2D stereo images are rendered from the 3D virtual world and passed to PM. Then, using our multi-scale phase based disparity algorithm, depth map is extracted for the current view and environmental map is updated. From the environmental map formed up to date, navigation destination is decided and cameras are controlled. Finally, new camera locations and parameters are passed to the SM. All these activities are recursively done in a continuous manner until all of the environment is explored. Each time a new depth estimate is calculated, environmental map is updated and each time all the information about a new object is fully extracted, object is recognized. Thus, map formation and object recognition sub-module and navigation and camera controller sub-module works in parallel.

Our human-like stereo vision system does not require special hardware. Only a standard PC and a frame grabber would be enough for obtaining stereo images in

natural environments. We inspired from biological binocular cell models and use steerable filters to extract interest points, called feature points in this thesis. The feature used in order to match corresponding feature points is the multi-scale phase information. The flow chart which summarizes our stereo vision algorithm is shown in Figure 2. Using steerable filters, feature points are extracted from both of the stereo image pair. Using the oriented filters at different scales, we obtain multi-scale phase and magnitude information at each feature point. Then corresponding pairs are matched based on multi-scale phase similarity. Finally, depth and 3D location information are calculated from disparity with the help of known camera parameters and location information.

1.2 Contribution

In this study we propose a biological model for feature based disparity estimation and use this system in robotic applications. First of all a biological disparity estimation model is proposed. Then our disparity algorithm is modeled probabilistically. Finally our disparity algorithm is used on a virtual robot with stereo vision in a 3D virtual world in order to construct 3D map of the environment and recognize objects around.

The usual method for feature point matching is to compare vector of filter responses at different scales and orientations which requires many operations since the compared vector could be very large [99, 40]. Later, Lüdtke, Wilson and Hancock uses population coding method in order to estimate a single orientation value for each feature point which would make the comparison easier. In their work they inspired from hyper-column structure of the visual cortex. When population coding is used to represent the convolution responses of the filter bank, the outputs of only a small number of filters need to be combined in order to achieve a considerable improvement of the precision of orientation estimation. However in their case, they use only a single scale in finding the feature points and estimating the orientation values. In this study we use steerable filters at three different scales

in finding our feature points and estimating orientations. When a small number of oriented filter responses are used to obtain responses at other orientations this is called steerable filtering. In this study we used the method of [26] in designing our steerable filters. Also, by using filters tuned at various frequencies, feature points having high information content at different local frequencies are selected. Although feature points extracted from image pairs are sparse, since they are the points of high contrast edges in various scales that define the bounding contours of objects, they still prove to be informative.

Since phase is very sensitive to spatial differences and at the same time very stable to lighting, orientation and scale deformations, using phase information in order to find correspondences between feature points provides reliable solutions. Unfortunately, there are image locations where phase is singular and can not be reliably used [38-39]. Such points are the locations where local frequencies at these points are very different from the filter tuning. In this study, by selecting feature points using multi-scale analysis, performing phase comparisons at multiple scales and by using magnitude confidence information we overcome these difficulties. The confidence weighting is used to augment phase information with information concerning the magnitude of the steerable filtered image to improve the correspondence method.

Using phase in correspondence matching is also biologically grounded. The reason for this is that simple binocular cells occur in pairs that are in quadrature phase. In physiological modeling of binocular cells, phase-based disparity methods are highly appreciated. Physiological phase-based models can be classified into two: 1. Disparity is estimated from local phase difference between left and right images based on Fourier theorem as been done in [84]. 2. Phase shift model of binocular cells: Receptive fields of binocular cells have phase differences and this is used in energy models [25, 76]. Both models have some limitations. Because, when phase is used, disparity estimation is reliable only for the disparity values less than half of the filter wavelength. Nature has a solution for this problem: In experimental

studies, it is observed that there are also binocular cells which have similar receptive fields but located at different positions [25]. There are biological cell models based on this finding and they are called position-shift models. In position shift models of binocular cells, receptive fields are similar but positioned at different locations. By this model a large range of disparities can be estimated. In [38-39] hybrid model which has both position shift and phase shift is proposed. However it also has same kind of limitation. In this study, two routes to locating feature-point correspondences are explored. Inspired from the position shift model, corresponding pairs are found by checking the phase vector similarity along epipolar line. Rough disparity values are obtained and a large range of disparities can be calculated, but to a limited accuracy. Inspired from the phase shift model, local phase difference is used in calculating subpixel disparity which has the accuracy less than one pixel. Fine tuning is performed without encountering the quarter cycle limit. This tuning scheme also allows a continuum of disparity estimates to be obtained.

In [8] stability of phase for some deformations is investigated and in a later study [9] they applied their method to feature matching and conclude that in order to be sure for stability of phase through scale, multi-scaling should be included. The use of multiple scales is also biologically plausible. The reason for this is that binocular cells, which are encoding disparity, are sensitive to different spatial wavelengths. In all the studies given above, first disparities at different scales are computed and then the results are pooled in order to obtain a single disparity map. However in this study, we include multiple scaling at the beginning both in extracting features and in matching. Disparity is estimated only once using multi-scale phase directly in matching.

In the probabilistic modeling of our matching algorithm, mixture of von Mises distributions is used. The distribution of phase differences between matched pairs at each scale for Venus stereo image pair is modeled and the models at all scales are tested on other stereo pairs. The important thing here is that although modeling is

done by using Venus stereo pair data only, it works fine for many other images. By this probabilistic model, we not only reach a higher success rate for many image pairs, but bring flexibility to the disparity search region.

Finally, the disparity estimation is applied to map construction and object recognition in a virtual world. Other than the usually known 2D occupancy grid method, a 3D map is constructed in this study. Our heuristic exploration strategy uses the advantage of active vision property. The importance of using vision in robotic applications is also emphasized by including an object recognition task. In recognizing objects, first of all point cloud belonging to an object is considered. Then this point cloud is segmented into two parts by using proximity and color similarity. Then surfaces are fit to each part and finally object is recognized from the shape of the parts.

1.3 Organization of the Thesis

In Chapter 2 literature review of vision for mobile robot navigation, stereo vision for mobile robot, various disparity algorithms, biological and robotic navigation, robotic map formation, virtual environments and 3D reconstruction from multiple images are summarized. In Chapter 3 our biological disparity algorithm is given. Results are also presented in the same chapter. Our probabilistic model for disparity algorithm is also explained in Chapter 3. In Chapter 4 application of our stereovision to a virtual environment for the purpose of 3D cognitive map formation and object recognition is explained thoroughly. The related results are also given in this chapter. Chapter 5 is the conclusion chapter.

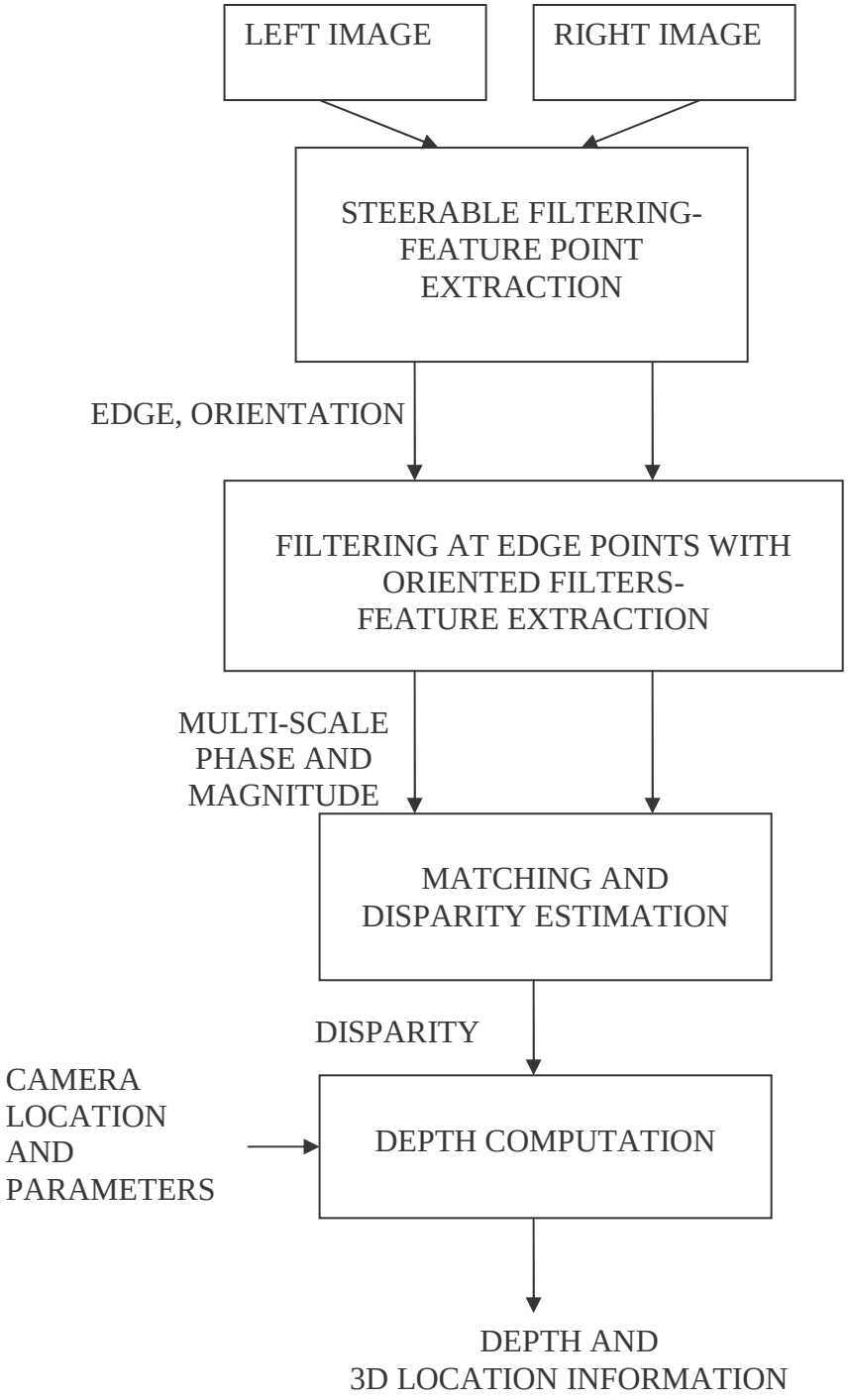

Figure 2 Flow chart of the stereo vision system.

CHAPTER 2

LITERATURE REVIEW

2.1 Vision for Mobile Robots

In this section, robot navigation in terms of vision researches is investigated. Robot navigation for which vision is used as sensors can be grouped into three classes [16]: 1. Map-based navigation which depends on user created models, e.g. CAD models, of the environment. 2. Mapless navigation where no map construction is required. 3. Map-building-based which uses sensors to construct a model of the environment.

2.1.1 Map-based Navigation

The robot is provided a model of the environment. These models may contain different degrees of detail. For example, occupancy map has the grid based information about the environment. It is easy to establish meaningful navigation goals for the robot. The human operator can use the internal map representation of a structured environment to conveniently specifying different destination points for the robot.

In this kind of navigation problems the basic issue is localization. The system tries to identify the observed landmarks by searching in the database for possible matches according to some measurement criteria. Once a match is obtained, the

system needs to calculate its position as a function of the observed landmarks and their positions in the database.

In probabilistic FINALE [60], the uncertainty in the position and orientation on the plane of the robot is represented by a Gaussian distribution and, thus, the uncertainty at each location of the robot is characterized by mean and covariance. In topological NEURONAV [58], a graph topologically representing a layout of the hallways is used for driving the vision process. Two modules, hallway follower and landmark detector are implemented using an ensemble of neural networks.

Most of the earlier methods use a single camera and a range sensor. In [73] monocular, trinocular vision based and laser based robot localization are compared and comparable precision levels are attained. Since vision provides much more information it is preferred by many recent studies although vision poses more complex matching problems than laser. In [98] images are retrieved and a data base is formed and then Monte-Carlo localization is used to find the similarity between the current image and the data base. In [89] triclops camera system is used and ego motion of the robot is calculated from the scale invariant features detected and matched through successive frames.

2.1.2 Map-less Navigation

Navigation is achieved without any prior description of the environment. No maps are ever created. Most robotic systems are limited to essentially just roaming in mapless systems. In most cases the robot only has access to a few sequences of images that help it to get to its destination or a few predefined images of target goals that it can use to track and pursue. Navigation using optical flow, appearance based matching, object recognition are some examples.

In navigation using optical flow, motion parallax is more useful and features such as “time-to-crash” are more relevant than distance when it is necessary to jump over an obstacle. In [65] N images of the same scene are obtained by N cameras

each having a different focal length where focal length is categorized in 3 steps, i.e. far, medium, close. Cameras are positioned together such that they see the same perspective. The scene is divided into regions and the best focus for each region is found by computing sharpness (i.e. intensity differences between all horizontally neighboring pixels). Thus, each region is assigned far, medium or close. The robot moves using the farness or closeness information in the regions of the image. In [45] active vision based control is used for collision avoidance as well as maintenance of clearance in a priori unknown textured environments. Change in image quality measure, which is defined in their study, is used in a fuzzy logic control.

In navigation using appearance based matching, memorizing the environment is done by storing images or templates of the environment and associating those images with commands or controls. In [30] the set of local views for a given panoramic image defines a “place” in the environment. Each place is associated with a direction (azimuth) to the goal. Finally, a neural network is used to learn this association and during actual navigation, it provides the controls that take the robot to its final destination. In [55] after a sequence of images is stored, the robot is required to repeat the same trajectory. The system compares the currently observed image with the images in the sequence database using correlation. The displacement in pixels between the view image and the template image is then used for steering. In [66], the robot is manually driven in the obstacle free hallway and expectation maps are rendered from the hallway model at regular intervals. First, the robot renders an expectation image using its current best estimate of where its present location is. Next, the model edges extracted from the expectation image are compared and matched with the edges extracted from the camera image through an extended Kalman filter. The Kalman filter automatically then yields updated values for the location and the orientation of the robot. Obstacles are found from the difference of vertical edges in the camera image and the expectation map immediately after each exercise in self localization.

In navigation using object recognition, instead of using appearance based approaches to memorize and recall locations, a symbolic navigation approach such as “go to the door” is used in [44]. In [5] vision based autonomous vehicle requires the ability to focus on the important features in an input scene. Task dependent emphasizing or deemphasizing is modeled by a neural network where hidden layer keeps important information for the task only.

2.1.3 Map Building

Automated or semi automated robots could explore their environment and build an internal representation of it. Occupancy grids are the basic methods. They allow measurements from multiple sensors to be incorporated. Even uncertainties can be embedded in the map. The extent to which the resulting geometry can be relied upon for subsequent navigation depends naturally on the accuracy of robot odometry and sensor uncertainties during map construction.

Additionally for large scale and complex spaces, the resulting representations may not be computationally efficient for path planning, localization, etc. Instead topological representations of space can be used [23]. These representations often have local metrical information embedded for node recognition and to facilitate navigational decision making after a map is constructed. Various proposed approaches differ with respect to what constitutes a node in a graph-based description of the space, how a node may be distinguished from other neighboring nodes, the effect of sensor uncertainty, the compactness of the representation. Major difficulty is the recognition of nodes previously visited.

In metrical approaches, on the other hand, if the odometry and the sensors are sufficiently accurate, the computed distances between the different features of space help in identifying places previously visited. The best of the occupancy grid based and topology based approaches are combined in [91] but using range sensors only. In [48] stereo camera system is used besides the laser range finder in map construction, object recognition and navigation. But the environment is a simple

indoor one and predefined special features are needed. In [42], on body depth generation system which requires only a PC and an image card is implemented.

After the formation of the map, the next problem is the localization. In [70] a map similarity measure is formed using the probability distribution of the distance from each occupied cell in the local map that is computed at the current robot position to the closest occupied cell in a previously computed map of the environment. This probability distribution function is used in a likelihood function for each robot pose. Some recent studies perform simultaneous mapping and localization as in [89] and [14].

2.2 Stereo Vision for Mobile Robots

Stereo cameras used in robotic applications are built to simulate the way human visual system works. Human visual system, having all its amazing powers, helps us to see the world, study the world and understand the world and is also very powerful in telling the depth of objects in the scene. Human visual system interprets depth in sensed images using both physiological and psychological cues. The physiological depth cues include accommodation, convergence, binocular parallax, and monocular movement parallax. The psychological cues are retinal image size, linear perspective, texture gradient, overlapping, aerial perspective, and shades and shadows. Among these cues, only convergence and binocular parallax are binocular depth cues (requiring both eyes to be open), while all others are monocular (one eye only). Detailed explanation of human depth perception can be found in Appendix A. Although stereo vision systems loses almost all the monocular cues as well as the binocular cue such as convergence and performs poorly so far compared to human visual system, stereo vision still becomes one of the most important resources of knowing the world for a mobile robot. One of the main reasons is that although it is very difficult to handle, imaging the world provides yet much more information of the world than most other sensors. Another reason is that as mobile robots are built to simulate or help human beings, it is important to make them look and work as

humans. With better and better stereo algorithms, advances in image processing, computer vision, artificial intelligence, etc., improvements in hardware, and with the belief that robot should act as human beings, we can anticipate that stereo vision will be one of the most widely used sensors for mobile robots.

In a standard setting of stereo imaging used on a robot, two cameras are bound together with a certain displacement. These stereo cameras have parallel optical axes and most likely the same focal lengths. In most application scenarios, by calculating the disparity map between the two captured images, stereo vision helps recover depth information of the environment, which can then be used by mobile robots to avoid obstacles, construct map, localize itself and recognize visual commands.

Stereo vision for mobile robots has some specific requirements. The first requirement is that the algorithm has to be real-time. The reason for this requirement can be miscellaneous, for example, to avoid obstacles or to recognize gestures. Second, mobile robots tend to move around and take pictures. This means the stereo algorithm needs to handle image sequences. This provides the algorithm a better chance to get the correct disparity map or refine it. Third, mobile robots are typically moving on a plane ground. To avoid obstacles on the ground, the disparity map can be calculated based on the plane ground (called horopter). Fourth, stereo is not the only sensor on a mobile robot. Fusion of multiple sensors needs to be studied to best estimate the environment the robot is in.

Some robotic applications where stereo is used are listed as follows:

Real time stereo processing and obstacle detection (horopter based stereo): Many approaches can be used to do stereo in real time especially when accuracy is not very important. For example, a hierarchical pyramid of the two stereo pair can be built and the matching can be refined step-by-step from coarse to fine level. As fine level disparity can be initialized by the coarse level disparity, this can improve the speed greatly. Another way to speed up stereo is to down sample the images, as well as the disparity levels. For mobile robot, sometimes ignoring the details may

actually help increase the stability of the system, especially when the task of the stereo does not require a lot of accuracy.

Localization, ego-motion and structure from motion: As the stereo cameras are mounted on the mobile robot and the robot is moving around, it is important to estimate the ego-motion and the structure at the same time. Although the ego motion can also be obtained from the motor meter, it might be very inaccurate. Stereo vision based approach can be a very good candidate for localization. In some studies the images of the landmarks are considered as feature points. When feature points between images can be well matched, the stereo matching algorithm will give a good estimation on the ego-motion of the robot [70, 89, 14].

Mapping and navigation: Instead of monocular or binocular cameras, the robot called Spinoza uses a trinocular stereo system for sensing in [61]. The trinocular cameras can normally achieve better results than a typical two camera stereo system because the second pair of cameras can resolve situations that are ambiguous to the first pair. In their study, Spinoza extracts the map of the environment.

Simultaneous mapping and localization: A series of seminal studies introduced a powerful statistical framework for simultaneously solving the mapping problem and the induced problem of localizing the robot relative to its growing map. Since then, robotic mapping has commonly been referred to as SLAM or CML, which is shortest form for simultaneous localization and mapping, and concurrent mapping and localization respectively. Some probabilistic approaches employ Kalman filters, expectation maximization (EM) algorithm etc. [91]. These approaches specifically address the correspondence problem in mapping, which is the problem of determining whether sensor measurement recorded at different points in time correspond to the same physical entity in the real world. A third family of probabilistic techniques seek to identify objects in the environment, which may correspond to ceilings, walls, doors that might be open or closed, of furniture and other objects that move. Usually such probabilistic algorithms are off-line and

can not be run in real time. In most recent studies map construction and localization and/or ego-motion extraction are simultaneously studied [89, 14].

2.3 Stereo Algorithms

2.3.1 Dense Stereo Algorithms

Recently there were some efforts by Scharstein and Szeliski [85] who tried to provide a common test bed for evaluating different stereo algorithms. In their work, they measure the performances of different algorithms based on known ground truth data. Four pairs of images were used in their system (Sawtooth, Tsukuba, Venus and Map). The two criteria they used were:

RMS (root mean square) error (measured in disparity units) between the computed disparity map $d_C(x,y)$ and the ground truth map $d_T(x,y)$:

$$R = \left(\frac{1}{N} \sum_{(x,y)} \left| d_C(x,y) - d_T(x,y) \right|^2 \right)^{\frac{1}{2}} \qquad \text{Eq 1}$$

Percentage of bad matching pixels (PBMP):

$$B = \frac{1}{N} \sum_{(x,y)} \left(\left| d_C(x,y) - d_T(x,y) \right| > \delta_d \right) \qquad \text{Eq 2}$$

where δ_d is currently set to be 1.0.

Stereo algorithms are compared on both accuracy and speed. Real time correlation based stereo is found to be the fastest one among all but also is the least accurate one. Sum of squared difference (SSD) and dynamic programming (DP)

take approximately one second for 384x288 Tsukuba stereo pair. However their percentage of bad matching pixel (PBMP) is less than the PBMP of real time algorithm. Graph cut (GC) takes around 23 seconds for the same image pair but its PBMP is nearly one third of SSD's PBMP. Layered stereo algorithm is the best performing one but takes the longest.

Here, some of the representative algorithms in the literature will be summarized.

Sum of squared difference (SSD): This is the most widely used technique in real applications. The algorithm handles the stereo pair row by row. A rectangular window is placed on an image and the window in the other image of the stereo pair that gives the minimum SSD compared with the window in the reference image is searched. Obviously the SSD of the two windows in the two images are a function of the disparity d. The disparity at a certain pixel d_0 is given by:

$$d_0 = \arg\min_{d} \sum_{(m,n)\in W} \left[I_{left}(m,n) - I_{right}(m+d,n) \right]^2 \qquad \text{Eq 3}$$

where I represents the image intensity, W is the comparing window. There are alternative criteria when searching for the best match such as sum of absolute difference (SAD) and normalized cross covariance.

Dynamic Programming (DP): Stereo matching can have many constraints about what a valid matching should be, based on our assumption about the scene. These constraints include the ordering constraint, the uniqueness constraint, the disparity limit, and the disparity continuity constraint, to name a few. [12]'s approach of dynamic programming uses ordering constraint and makes an assumption that if two pixels are corresponding to each other, their intensity difference follows the Gaussian distribution. The overall cost function is defined through a maximum likelihood criterion. The cross-correlation for two corresponding epipolar lines is calculated for all pairs of lines. The optimal path is found by searching a path that gives the minimum cost function.

Graph cut (GC): A problem with the above two approaches is that each epipolar line is processed independently. The solutions obtained on consecutive epipolar lines can vary significantly and create artifacts across epipolar lines, especially affecting object boundaries that are perpendicular to the epipolar lines. Graph cut is a different approach that optimizes the solution globally. The ordering constraint is replaced by a more general local coherence constraint, which claims that disparities tend to be locally very similar in any and all directions. To achieve the above constraint, epipolar lines are stacked together and form a correlation cube. The goal is to find the best surface in the cube that minimizes the overall cost. This problem can be reformulated as a maximum-flow problem in a graph. If a source and a sink are added to the cost cube, and all the discrete points in the cube are considered as vertices of the graph, the maximum flow between the source and sink is the minimum cut of the graph, which will be effectively the disparity surface.

Layered Stereo: [4]'s approach is very different from what have been discussed so far for the representation of the depth map. The scene is represented as a collection of approximately planar layers. Each layer consists of an explicit 3D plane equation, a colored image with per-pixel opacity (a sprite) and a per-pixel depth offset relative to the plane. The authors claim that using this kind of representation, the depth and color information can have high accuracy even in partially occluded regions, and the representation is very suitable for rendering and video parsing. The algorithm has two steps: initial estimate and layered refinement by re-synthesis. In the initial estimate state, with some manual interaction, the scene is segmented into different initial 'layers'. Each layer is then fitted by a planar equation in the least square sense. The layer sprite on each layer is then synthesized by image blending. As a plane model may not be able to describe the scene very well, the residue of the disparity is calculated with any normal stereo algorithm. In the re-synthesis stage, the original stereo images are re-generated with the layered model. The prediction error between the re-produced images and the original images is minimized. The authors believe that this kind of representation may be

helpful for mobile robots as well. A simple scenario is to represent the world with progressive level of details. The planar model may be the very first level of details for the scene, when the object is still far from the robot. When the robot gets closer to the object, finer model by adding the residue will be used for the robot to avoid obstacles.

Real-time correlation based stereo: For mobile robot, real time is more critical, as if the robot has obstacle avoidance algorithm that is based on stereo, better it can see the obstacle as early as it can. At early times, real-time performance was reached by using DSP board. Now that computers gets faster and faster, software based real-time stereo can be easily achieved.

Phase based stereo: Jenkin and Jepson [37-39] and Sanger [84] describe promising methods based on the output phase behavior of band-pass Gabor filters. Fleet and Jepson [39] discuss further justification for such techniques based on the stability of band-pass phase behavior as a function of typical distortions that exist between left and right views. They show that phase signals are occasionally very sensitive to spatial position and variations in scale, in which cases incorrect measurements occur. With the aid of the local frequency of the filter output (provided by the phase derivative) and the local amplitude information, the regions of phase instability, which are called singularities, are detected so that potentially incorrect measurements can be identified. They also show how the local frequency can be used away from the singularity neighborhoods to improve the accuracy of the disparity estimates. Recently, Carneiro and Jenkin provide multi-scale phase-based stable features [8, 9].

2.3.2 Sparse Stereo Algorithms

In sparse stereo algorithms [33, 52, 56, 57, 82], distinctive features from the images are extracted and corresponding pairs are matched using some feature-based criteria. The advantage of these methods is that they produce accurate results. The disadvantage is that the results are rather sparse and textureless regions are left

unmatched. Since disparity is calculated only for the feature points in sparse algorithms, some post processing such as interpolation, surface fitting is necessary in order to extract the dense depth map. In [27] a probabilistic model is proposed to fill the gaps.

Sparse stereo algorithms are usually used for estimating camera geometry [93]. Computations are concentrated on areas of the image where it is possible to get good correspondence and from these an initial estimate of camera geometry is made. This geometry is then used to guide correspondence in regions of the image where there is less information. Sparse stereo algorithms can also be used in robotic applications such as obstacle avoidance and mapping when a low precision is enough [14, 48, 61, 70, 89].

To be successful for stereo applications, local features must be robust to typical image deformations such as scale changes, noise, brightness changes, rotation and be highly distinctive to afford identity information. There are different types of features used both in stereo vision and object recognition field. Very early ones are zero crossings, peaks, simple definition of edges [56] and segments [57]. In recent years, informative edges, curves [82], corners [35], local extremes in the responses of difference of filters [50], auto-correlation function in order to determine locations where signal changes in two directions [86], contour detection [64], tangent fields [99, 51] are some other suggested local features and feature extraction algorithms for object recognition.

After detecting the feature locations, they should be described in a way that they should provide strong information and be stable to small changes. Some of the descriptions at feature points are as follows: Sets of derivatives that is invariant to rotation [86], scale invariant feature transform features [50], phase and amplitude [8]. Carneiro and Jepson builds on previous work [21] in which it was shown that the phase information provided by steerable filters is often locally stable with respect to scale changes, noise and common brightness changes and show that it is also possible to achieve stability under rotation by selecting steerable filters [8].

They deform a given image by changing the brightness, introducing non-uniform brightness variation, adding noise, changing scale and rotation and select interest points by Harris corner detector [35] on both the original and the deformed images. Then steerable quadrature filter pairs are used to obtain local amplitude and phase information. Since a pixel does not provide a distinctive response, they considered M sample points taken from a region around each interest point. At each spatial sample point (i.e. the interest point and the sample points taken from a region around it) the filters are steered to N equally spaced orientations starting from the main orientation of the pixel computed as described in [26]. The resulting phase-based, complex feature vector has M*N individual components specified by the complex filter responses. Finally, they computed the similarity between local features between the original and the deformed images using normalized phase correlation since this is known to provide some stability to typical image deformations. The detection rate is defined to be the proportion of interest points such that there are some interest points in the transformed image which is both sufficiently close to the mapped point and which has a similar local feature vector. They compared their results with differential invariant features [86] and showed that phase-based feature displays consistently better results.

In order to make the phase-based approach more comparable to the other approaches, Carneiro and Jepson also introduce a new form of multi-scale interest point detector [9]. Since Harris corner detector is not very robust to scale changes, they use an approach similar to [17], in which they check local spatial information to determine whether the current scale is appropriate. They calculate the local frequency of the response with the derivative of the phase signal and the interest points that have local frequency close to the mean frequency of all the interest points are selected to be locally stable. In order to achieve semi-invariance to scale changes, space is sampled at a discrete set of scales. Given a feature vector from a test image, they searched database for similar features, irrespective of the specific scales at which they were observed in the test and model images. Then the specific

scales belonging to the matched features provide some information about the relative scales of the target in the test and the database images. They conclude that although phase-based local feature performs better in terms of common illumination changes, 2D rotation and sub-pixel translation, for scale and large shear changes both shift invariant feature transformation and the differential invariants produce better results. However, they also suggest that the robustness of the phase-based feature to scale changes can be improved by using a denser sampling in the scale-space.

2.3.3 Biological Stereo Algorithms

In many recent studies, spatial filtering of the image pairs by Gabor filters is well accepted because Gabor filters are limited spatially and have finite bandwidth. Another attractive aspect of using Gabor filters is their orientation selectivity. The usage of Gabor filters is also supported by some physiological findings. A Gabor filter has a shape very similar to the receptive field profile of simple cells in primate visual cortex. It is also found that adjacent simple cells have the same orientation and spatial frequency and are in quadrature pairs. This observation also leads the researchers to think that phase of a complex Gabor filter can be internally encoded by such a pair of neighboring simple cells.

In their experimental studies, Freeman, Ohzawa and Anzai [25, 67, 68, 1-3] obtained monocular receptive fields and binocular interaction receptive fields for simple and complex cells in adult cats. And they showed that these cells could be modeled by Gabor-like functions. They also show experimentally that the receptive fields for the left and right eye can be similar in some cells, but are clearly different for the others and the degree of differences between receptive fields is quantified by using receptive field phase. This observation has lead to the use of Gabor filters to model the phase difference for the receptive fields to act as disparity decoders.

Inspired from all these findings, Anzai et. al. [1-3] models disparity selective complex cells. In this feed forward model of disparity extraction, complex cells are

the actual disparity detecting elements, each of which receives input from four binocularly innervated simple cells, all with the same preferred contour orientation. For a given cell, the left and right eye receptive fields have matching spatial profiles. These four simple cells are grouped into two pairs, with members of a pair having receptive fields modeled by Gabor filters that differ in spatial phase by 90° (i.e. they are quadrature pairs). The outputs of these simple cells are squared and then summed by the complex cell. Thus the complex cell response can be said to be the disparity energy and this energy becomes maximum when the disparity of the given stimulus is equal to the disparity between the receptive fields. In their model it is always zero. Although the model is promising, the phase selective complex cells just predict the zero disparity and they can not uniquely signal any given retinal disparity. Nor can they signal disparities beyond the quarter cycle limit of the input signals. Quarter cycle limit is the limit on disparity that can be found using Gabor filters at a specific spatial frequency. If a pattern of spatial frequency ω (i.e. period is $1/\omega$) is presented to the two eyes, left and right images of that pattern can be unambiguously matched so long as the disparity between the two images does not exceed one half the period of the grating, $1/2\omega$. Qian [76-78] has improved the complex cell model so that it can uniquely signal definite disparities.

Although studies of Anzai et. al. [1-3] clearly shows that phase differences do exist, their data do not rule out a contribution of position differences to disparity encoding. Besides phase shift model, position shift model is also available with the general receptive field structure of simple cells. In the position shift model, the receptive field profiles are assumed to have identical shape in the two eyes, but are centered at non-corresponding points on the retina. In the phase model, the range of disparities encoded by a population of neurons is inversely proportional to spatial frequency. This is because phase differences are limited to a range of 180° and because a particular phase difference corresponds to a large preferred disparity when the spatial frequency is low, but a small disparity when the spatial frequency is high. In contrast, for the position shift model, the range of disparities can be

encoded. Fleet et. al. [38-39] uses a hybrid model of disparity encoding cell which has its receptive field profiles differ by both an overall positional shift and a phase difference. In his model, when receptive fields are exactly the same, then the energy neuron is sensitive to zero disparity as in Ohzawa's model. If there is only a phase difference between receptive fields, then the energy neuron response reaches a maximum when the disparity is equal to the intraocular phase difference divided by the instantaneous frequency. If there is a position shift between the receptive fields, then the cell gives the maximum response when the disparity is equal to the position shift. In the hybrid model where receptive fields are shifted in position and also have phase shift, the binocular energy response of the neuron depends continuously on both the position shift and the phase shift. This hybrid model posits that the energy should be sampled at each spatial position, with several position shifts and with several different phase shifts. In Figure 3, three different types of disparity encoding cell models are shown. The leftmost drawing is for position shift model where the internal structure of the receptive fields is the same but cells are positioned at non-corresponding points on the retina. The middle drawing is for phase shift model where cells are positioned at corresponding points on the retina but have phase difference. The right most drawing is for the hybrid model where both cells are positioned at non-corresponding points and have phase difference.

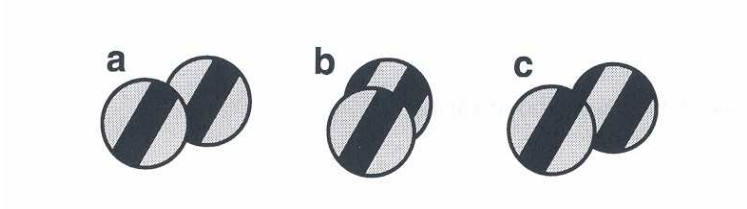

Figure 3 Different models for disparity encoding cells: a. Position shift model, b. Phase shift model, c. Hybrid model. (Picture is taken from [19])

Using phase difference in complex Gabor filters to decode disparity is not limited to models of complex cells using phase differences only. But complex Gabor filters have also been used for finding disparity from the region-based phase differences between the left and right images [84]. Sanger filters the stereo image pair with different oriented and sized complex Gabor filters and by checking the regional similarities of phase of complex Gabor filtered images finds the corresponding regions.

Potential problems with the use of phase as disparity encoder have been identified by Jenkin and Jepson [37] and Jepson and Fleet [38, 39]. If the stereo images are subjected to affine image deformations such as scaling or shifting with respect to one-another, at certain locations phase may not be stable through scale. These locations are referred to as singular points and can be identified in one of the two ways [37]: either they posses a central frequency which was very different from the central frequency of the Gabor used to filter the image, or they lacked a relatively constant amplitude term. It is suggested that those singular points should be discarded in correspondence analysis and methods of doing so is given in [37].

Using Multi Scale in Biological Disparity Encoding

Since extensive physiological and psychophysical evidence implicates spatial filtering by cortical receptive fields that are responsive to a limited range of spatial frequencies, with the peak frequency (i.e. the value yielding maximum response) varying among cells, many models incorporate spatial filters of multiple scale or size to model the shift in peak spatial frequency [7]. In these models, small receptive fields (high spatial frequency) process small disparities, while larger receptive fields (lower spatial frequency) process progressively larger disparities.

Marr et. al. [52] argue for a coarse to fine search procedure. Estimates are first computed at coarse scales. Once obtained, they are used as initial guesses for finer scale matching. Pollard et. al. [74] refines stereo correspondences by checking their behavior through scale. If they are all relevant at different scales, they keep the pairs

as correct matches, otherwise they discard these matches. Inspired from the knowledge that humans can not compare spatial phase between frequencies more than two octaves apart, Sanger [84] combines disparities at different scales separated by two octaves using a weighting method. In [76] a simple method which averages over different scales is used. In [22] the energy responses at different scales are simply summed. This pooling helps the large responses near the correct disparity sum to produce even larger peak. Anzai et. al. [1-2] model a binocular disparity representation in which disparity information is encoded by a group of cells in terms of phase disparity at each size or spatial frequency scale.

2.3.4 Probabilistic stereo algorithms

Experiences show that disparity estimations from local phase-differences as been done in [84] are reliable near edges but yield poor results between them. In [27] a probabilistic lattice structure is proposed to fill unreliable regions which result after phase-based disparity estimation by using a simple smoothness constraint in the spirit of Markov random fields. The probability of being a pair is modeled by an exponential function (Eq 4) where the parameter is the usual local phase difference divided by the filter wavelength, k_0 (Eq 5). But in this case while the phase difference method as used in [84] is limited to only small disparities, with the help of exponential, longer shifts can also be considered in this case.

$$p(x_L, x_R) = e^{-\pi\, d(x_L, x_R)^2} \qquad \text{Eq 4}$$

$$d(x_L, x_R) = \frac{\phi_R(x_R) - \phi_L(x_L)}{k_0} \qquad \text{Eq 5}$$

In many other probabilistic algorithms which estimate the disparity map between the stereo images, usually the starting point is to maximize the conditional probability of disparity given stereo images. The main problem is how to calculate the conditional probability given only stereo image set. In [46] Gibbs' distribution

is used to transform energy into probability. What is special in this study is that they consider point wise energy based on Markov Random Fields theory where it is proved that it is possible to estimate the disparity of a position, if all of the joint probability distributions between neighborhood disparities are known in advance. Assuming that the disparities in the neighborhood of a pixel are independent one another, the joint probability can be rewritten as the product of marginal probabilities of each disparity in the neighborhood. Myers, Wilson and Hancock applied their graph edit distance method to uncalibrated stereo correspondence problem where corrupted relational graphs are compared and matched [63]. In [59] a probability distribution function for disparity gradient is proposed for windowing operation. They formulated the relation between the maximum search space in the second image with respect to the relative displacement of the continuous edges in the successive scan lines of the first image. In [71] his previous work [70] on matching edge images for robot localization is generalized. Using a probabilistic framework, his method considers the distance from each pixel in the template to the closest matching pixel in the image. The joint probability density function is approximated as the product of each individual probability distribution function, assuming that the distance measurements are independent. This study is also a good example in order to show the close relation between stereo matching and robot localization.

2.4 Reconstruction from Multiple Images

3D point clouds obtained by image matching are intermediate results and should be integrated into a 3D surface model. Methods that manipulate or create surfaces in the object space can be listed as follows:

Surface fitting to organized data points: Besides the coordinates of the points, connectivity information is also available for each view. Usual surface fitting algorithms can directly be applied.

Surface fitting to unorganized data points: Surfaces are fitted to unorganized point cloud in the object space. A given initial mesh can be deformed by energy minimization, planar surface patches can be fit to 3D points defined by segmentation of color images, points can be clustered into regions of similar surface orientation for surface fitting to unorganized data. In [29] iterative re-weighted least-squares is used where the surface primitives are small disks in 3D called "oriented particles". Leloğlu and Halici fit growing planar surfaces to 3D points [47].

Minimizing re-projection error by optimization: The surfaces in 3D are obtained with no need to a prior image matching phase. For the purpose of maximization of multi-image correlation by changing parameters of a surface, in [28] an objective function defined over multiple images is minimized by moving the vertexes of a triangular mesh.

Volumetric methods: Surfaces are obtained without explicit matching. In the space carving method, part of the space that contains objects is divided into voxels and outermost voxels of the volume are removed if they are not justified by the images [62]. When the volume does not shrink any more, a surface covering the volume is generated. There is no explicit surface model until the volume is generated.

2.5 Biological Navigation and Robotic Applications

Navigation means directing a ship to its destination. This includes three steps: 1. The navigator determines the ship's position on a chart as accurately as possible. 2. On the chart, he relates his position to the destination, reference points and possible hazards. 3. Based on this info, he sets the new course of the vessel. As a similar approach, the steps of navigation in robotics can be listed as follows: 1. The robot finds where it is. 2. The robot discovers where the other places are with respect to it. 3. The robot plans how to get to other places from where it is.

Since no system which has the flexibility and navigation performance of animals such as bees, ants, has been reached yet, this motivated robotics researchers to look for biological navigation mechanisms that can be implemented on an autonomous mobile robot. Researches on animals show that “where am I?” is not the first question to ask [24]. The most important question is “how do I reach the goal?” Thus a new definition for navigation can be done as follows: Navigation is the process of determining and maintaining a course or trajectory to a goal location.

Navigation can be completed with two successive stages: Local navigation and way finding. Local navigation can be achieved with minimal internal state and the agent chooses its actions on the basis of current sensory or internal information without the need of representing any objects or places outside the current sensory horizon. Whereas way finding involves the recognition of several places and the representation of relations between places which may be outside the current range of perception. Way finding requires internal structures that encode at least some aspects of the agent’s past experience of its environment. In animal world, invertebrates do not appear to memorize the spatial layout of their environment, and as a consequence, their way finding behavior may be restricted to homing and retracing familiar routes [75]. In contrast, there is evidence that higher vertebrates do learn the spatial layout of their environments enabling them to generate and follow more efficient paths to distant targets [75].

2.5.1 Local Navigation

There are four different types of local navigation in terms of Franz’s classification [24]. In terms of increasing complexity they are listed as follows:

Search: Locomotion and goal detection is enough for this kind of navigation. The goal can be found by chance if the agent hits it while moving around. It is not efficient in terms of time.

Direction following: The agent must be able to align its course with a locally available direction to find the goal. The goal does not need to be perceivable during approach. If the agent displaced from the trail, it will miss the goal. E.g. ship setting its course along a fixed compass direction. Inspired from flying insects which are able to centre their flight path in a corridor by balancing image motion in their two eyes [11], a robot equipped with a wide angle camera follows the walls in a corridor by balancing the maximal flow on both sides and centering its course between the nearest objects.

Aiming: An agent has to orient its body axis such that the goal is in front of it. The goal must be perceivable during approach. E.g. ship navigating to a widely visible light house. In [36] a robot with motion detecting camera is used in the same manner as flies do. When an isolated object passes from front to back during flight, the fly compensates for the optic flow created by the object by counter rotating until the object is brought in front of the insect where it creates no image motion.

Guidance: the agent can be guided by spatial configuration of the surrounding objects. Spatial information is the relation between the current location, goal and current perceivable environment: E.g. A ship that tries to reach a fixed position between several islands. In [10] bees and ants are inspired where they store a relatively unprocessed snapshot of the surrounding panorama as seen from the goal. A robot with omni directional camera is used where the landmarks in the view are black regions on white background. From the difference between the image positions in the snapshot and the current view, a movement direction was computed to reduce the perceived difference.

2.5.2 Way Finding

Way finding can also be classified into three [24]:

Recognition triggered response: Starting location triggers the activation of local navigation method leading to the goal. This can be taken as the elementary

step for building routes. There is no planning involved, as knowledge is limited to the next action to perform. If one route is blocked, the agent has to resort to a search strategy until it reaches a known place again. In [81] hippocampus is viewed as an auto associative memory which stores a scene representation consisting of bearings and distances of the surrounding landmarks and of a goal location inspired from the idea that place cells in rat hippocampus discriminate between different parts of an environment. Place recognition is achieved by feeding the current scene into the associator which activates the stored scene memory if it matches the current scene. The stored direction and distance of the goal are activated together with the scene memory and could be used to directly drive towards the goal.

Topological navigation: If the two routes pass through the same place, they have to be merged in topological navigation and this process is called route integration. A collection of integrated routes thus becomes a topological representation of the environment and this representation is usually a graph. Any vertex can become the start or the goal of a route such that in case of obstacles, alternative intersecting routes may be found which is a planning. Topological navigation is the combination of planning and route integration but it can not generate novel routes over unvisited terrain. In [54] inspired form experiments on rat navigation, a robot with a ring of ultrasonic sensor and a compass is used. As long as sensory conditions remain the same (ultrasonic sensors sense a corridor leading into south) robot executes a single behavior. A new behavior is triggered by arriving at a distinctive place showing a qualitative change of the immediate environment such as a corner or a dead end.

Survey navigation: It requires the embedding of all known places and of their spatial relations into a common frame of reference. Spatial representation must be manipulated and accessible as a whole. E.g. finding shortcuts in unknown terrain between unconnected routes. Survey navigation is limited to vertebrates. The complicated navigation behavior of vertebrates is still less understood so that most corresponding biomimetic approaches have to remain on a very abstract level. Some

exceptions are the models of the rat hippocampus that can draw on a large number of neurophysiological investigations where a cognitive map is thought to be stored in the hippocampus [24]. However still there are different views for the exact role of hippocampus in navigation. But the concept of cognitive map is highly appreciated. Since cognitive map construction is one of the main purpose of this thesis this subject will be investigated more in the following sub-section.

2.5.3 Cognitive Maps

Goal independent memories of spaces which are very important for topological and survey navigation can be used for many different routes and these goal independent memories of space are called cognitive maps. In cognitive map route description is in this manner: “if you want to go to B, you should turn left”. Thus cognitive maps can be used as a route planning stage or short cut finding which are the abilities of higher vertebrates only. Hippocampus is known to be the place for cognitive maps and many physiological experiments have been done on rat hippocampus in order to get more information about cognitive map structure.

In [31], starting from insect homing mechanism, higher vertebrate map construction and shortest path discovery is modeled by neural networks. In [49] physiological modeling of hippocampus is used for cognitive map modeling. A cell growing ability network is constructed where different type of cells and layers of these cells such as landmark cell layer, place cell layer are modeled. The creation of place cell requires that at least three landmarks are nearby and visible to the agent. Each place cell is laterally connected to some place cells neighboring to it. The place fields of all place cells cover and partition an explored environment. As the agent moves, it keeps track of the place where it is currently situated and the place it previously was. Route finding is based on the traveling experience that is coded in the weights of lateral connections between place cells. For finding the shortest path an activation spreading process is used. In [79] a learning procedure is added on the links of the cognitive map which enables to reinforce particular paths, and to forget

others, allowing for an adaptation to a changing perception of the environment, as it is gradually discovered by the animate. The map is also associated with a motivational system so that the most interesting places can be linked with the appropriate motivation. The learning rule includes the activity of the cells and the external reinforcement that appears when the animate enters or leaves a difficult or dangerous area. When a particular need has to be fulfilled, the associated motivation triggers the activation of the appropriate neuron in the cognitive map. The activity then diffuses along the route to be followed for reaching the goal.

2.6 Robotic Mapping

In this section, different models of cognitive maps used in robotic research and problems faced in robotic mapping algorithms are summarized. In the last sub-section, simultaneous localization and mapping is explained.

2.6.1 Taxonomy of robotic mapping

Metric versus Topological Mapping

Robotic mapping research has a long history. In the 1980s and early 1990s, the field of mapping was widely divided into metric and topological approaches. Metric maps capture the geometric properties of the environment, whereas topological maps describe the connectivity of different places. An early representative of the former approach was occupancy grid mapping algorithm which represents maps by fine-grained grids that model the occupied and free space of the environment. Topological maps represent environments as a list of significant places that are connected via arcs. Arcs are usually annotated with information on how to navigate from one place to another. Topological models may suit constrained environments of corridors and tunnels that are easy to segment into the vertices and edges of a graph representation but be less suited to open terrain.

In animate artificial intelligence research on way finding, metric and topological maps are referred to as quantitative and qualitative spatial models respectively.

Qualitative models of spatial layout have an important advantage over route knowledge, in that they allow the agent to generate novel routes (using known path segments). However, such models do not allow the determination of ‘straight-line’ routes or of short cuts that cross unexplored terrain –such skills require knowledge of the quantitative spatial relations, direction and distance, between locations. In view of the importance of effective way finding to autonomous agents this is a very significant point in favor of the use of quantitative spatial knowledge.

One of the basic studies of topological mapping is Franz et. al.’s learning view graphs [23]. In their study, view graph approach from the mazes of Schölkopf and Mallot [88] is extended to open environments. Humans are able to navigate in unknown environments after presentation of sequences of connected views. This has led to the concept of a view graph. A view graph is defined as a topological representation consisting of local views and their spatial relations. Depending on the task, these relations can be, e.g., movement decisions connecting the views, or mere adjacencies. Since open environments do not impose a structure on the view graph, a set of views have to be selected and the connections between them have to be found. In their study the vertices of the acquired view graph are panoramic views of the environment and its edges are connections between views that can be traversed using a visual homing procedure. Since only visual information is used here, it must be guaranteed that the recorded views are sufficiently distinct. During exploration, the system constantly checks whether the current view becomes similar to the already recorded snapshots. This again is a view classifier as used for the selection of the snapshots. In a second step, the system checks whether the detected snapshot is not yet connected to the vertex from which the current exploration step started. Whenever these conditions hold, the system tries to home to the snapshot. If successful, an edge connecting the two vertices is included, and the exploration continues from the detected snapshot. In cases where the robot gets lost or bumps into obstacles, a non-edge is recorded between both vertices thus preventing the failed action from being repeated. During exploration, the infrared sensors of the

robot are continuously checked for the presence of nearby objects. If obstacles are detected at distances larger than 1cm, the robot tries to turn away without slowing down. Smaller distances are interpreted as collisions causing the robot to back up and turn away from the obstacle.

In grid-based (metric) paradigm, environments are represented by evenly spaced grids [60]. Each grid cell may include the presence of an obstacle in the corresponding region of the environment. If the position of a mobile robot can be tracked accurately (however usually accumulated error exists), different positions for which sensor measurements look alike are naturally disambiguated. Nearby geometric places are recognized as such, even if the sensor measurements differ. Grid based approaches suffer from complexity especially when the resolution of a grid must be fine enough to capture every important detail of the world.

In [91] grid-based map (discrete, 2D occupancy grids) is converted to a topological map. Each grid cell <x,y> in a map has attached a value of belief that this cell is occupied. Belief is defined as whether or not the center of the robot can be moved to the center of that cell. Occupancy values are determined based on sensor readings where sonar interpretations must be integrated over time to yield a single, consistent map. Using Bayesian approach and conditional independence approximation, integration over time for sonar sensors are obtained. In the presence of odometric errors maps are usually less accurate. In their study, wheel encoders, map matching and wall orientation information are integrated in order to minimize position error. After obtaining the grid-based map the following algorithm is applied to convert it to a topological map: First each occupancy value in the occupancy grid is thresholded. Then Voronoi diagram is constructed and critical points on the Voronoi diagram, which are the points that minimize clearance locally, are found. Critical lines are obtained by connecting each critical point with its basis points. These critical lines partition the free-space into disjoint regions. Finally, the partitioning is mapped into an isomorphic graph. Each region corresponds to a node in the topological graph, and each critical line to an arc.

The distinction between metric and topological has always been fuzzy, since virtually all working topological approaches rely on geometric information. In practice, metric maps are finer grained than topological ones. Higher resolution comes at a computational price, but it helps to solve various hard problems, such as the correspondence.

Many quantitative navigation systems seek to construct maximally accurate metric world models. Such an aim can justify the construction of a unified model, into which all available observations are integrated, as the most efficient way to minimize errors in estimates of spatial position. However, from the point of view of a navigator, accuracy may not be the key criterion for determining the adequacy of its spatial knowledge [75]. This is shown by recognizing that effective way finding rarely needs an accurate assessment of the position of a remote target – a navigator who begins with just a coarse estimate of the required heading can 'home in' on the distant goal by making successive corrections based on incoming perceptual data [75]. Rather than seeking to maximize accuracy, the animate artificial intelligence approach emphasizes strategies for coping with the inevitable error and uncertainty attached to acquired knowledge.

World-centric Versus Robot-centric Mapping

Historically, a second taxonomy of mapping algorithms is world-centric versus robot-centric. World-centric maps are represented in a global coordinate space. The entities in the map do not carry information about the sensor measurements that led to their discovery. Robot-centric maps, in contrast, are described in measurement space. They describe the sensor measurements a robot would receive at different locations. At first glance, robot-centric maps might appear easier to build, since no 'translation' of robot measurements into world coordinates is needed. However, robot-centric maps suffer two disadvantages. First, it is often difficult to extrapolate from individual measurements to measurements nearby, unexplored places –an extrapolation that is typically straightforward in world-centric approaches. Second,

if different places look alike, robot-centric approaches often face difficulties to disambiguate them, again due to the lack of an obvious geometry in measurement space. For these reasons, the dominant approaches to date generate world-centric maps. For example in [75], a quantitative model of environmental layout is achieved by integrating observations from different egocentric view-points into representations with respect to environment-centered co-ordinate frames.

2.6.2 Problems in Robotic Mapping

Sensor Problems

To acquire a map, robots must possess sensors that enable it to perceive the outside world. Sensors commonly brought to bear for this task include cameras, range finders using sonar, laser, and infrared technology, radar, tactile sensors, compasses, and GPS. However, all these sensors are subject to errors, often referred to as measurement noise. More importantly, most robot sensors are subject to strict range limitations. For example, light and sound cannot penetrate walls. These range limitations makes it necessary for a robot to navigate through its environment when building a map.

The motion commands (controls) issued during environment exploration carry important information for building maps, since they convey information about the locations at which different sensor measurements were taken. Robot motion is also subject to errors, and the controls alone are therefore insufficient to determine a robot's pose (location and orientation) relative to its environment. A key challenge in robotic mapping arises from the nature of the measurement noise.

Modeling problems are usually relatively easy to solve if the noise in different measurements is statistically independent. If this were the case, a robot could simply take more and more measurements to cancel out the effects of the noise. Unfortunately, in robotic mapping, the measurement errors are statistically dependent. This is because errors in control accumulate over time, and they affect

the way future sensor measurements are interpreted. Accommodating such systematic errors is the key to building maps successfully, and it is also a key complicating factor in robotic mapping. Many existing mapping algorithms are therefore surprisingly complex, both from a mathematical and from an implementation point of view.

Size Problem

The second complicating aspect of the robot mapping problem arises from the high number of the entities that are being mapped. A detailed two-dimensional floor plan, which is an equally common representation of robotic maps, often requires millions of numbers.

Correspondence Problem

A third and possibly the hardest problem in robotic mapping is the correspondence problem also known as the data association problem. The correspondence problem is the problem of determining if sensor measurements taken at different points in time correspond to the same physical object in the world. The correspondence problem is difficult, since the number of possible hypotheses can grow exponentially over time. Although the correspondence problem was basically ignored in the robot mapping community, in recent years it has emerged.

Dynamism Problem

Fourth, environments change over time. Some changes may be relatively slow, such as the change of appearance of a tree across different seasons, or the structural changes that most office buildings are subjected to over time. Others are faster, such as the change of doors status or the location of furniture items, such as chairs. Even faster may be the change of location of other agents in the environment, such as cars or people. The dynamism of robot environments creates a big challenge, since it adds yet another way in which seemingly inconsistent sensor measurements can be

explained. To see, imagine a robot facing a closed door that previously was modeled as open.

There are almost no mapping algorithms that can learn meaningful maps of dynamic environments. Instead, the predominant paradigm relies on a static world assumption, in which the robot is the only time-variant quantity (and everything else that moves is just noise). Consequently, most techniques are only applied in relatively short time windows, during which the respective environments are static.

Exploration Problem

A fifth and final challenge arises from the fact that robots must choose their way during mapping. The task of generating robot motion in the pursuit of building a map is commonly referred to as robotic exploration. While optimal robot motion is relatively well-understood in fully modeled environments, exploring robots have to cope with partial and incomplete models. Hence, any viable exploration strategy has to be able to accommodate contingencies and surprises that might arise during map acquisition. For this reason, exploration is a challenging planning problem, which is often solved sub-optimally via simple heuristics. When choosing where to move, various quantities have to be traded off: the expected gain in map information, the time and energy it takes to gain this information, the possible loss of pose information along the way, and so on.

2.6.3 Simultaneous Localization and Mapping

Since the 1990s, the field of robot mapping has been dominated by probabilistic techniques. A series of seminal studies introduced a powerful statistical framework for simultaneously solving the mapping problem and the induced problem of localizing the robot relative to its growing map. Since then, robotic mapping has commonly been referred to as SLAM or CML, which is shortest form for simultaneous localization and mapping, and concurrent mapping and localization respectively.

Some probabilistic approaches employ Kalman filters, expectation maximization (EM) algorithm etc. [91]. These approaches specifically address the correspondence problem in mapping, which is the problem of determining whether sensor measurement recorded at different points in time correspond to the same physical entity in the real world. A third family of probabilistic techniques seek to identify objects in the environment, which may correspond to ceilings, walls, doors that might be open or closed, of furniture and other objects that move. Usually such probabilistic algorithms are off-line and can not be run in real time. A real time incremental EM in order to obtain map for cyclic environment is suggested in [92]. The mapping is formulated as a maximum likelihood estimation problem in the high sized space of all grid maps. The estimation is carried out using the expectation maximization algorithm. In their study the key feature is the forward modeling of the physical sensors. Forward models describe the physics of the environment, from causes (occupancy) to effects (measurement). In their study, the forward model is a mixture model specific to range finders, such as sonar sensors. The optimization begins with an entirely unoccupied map. EM then iterates two steps, an expectation step (E step) and a maximization step (M step), thereby gradually increasing the likelihood of the data until a local maximum is reached. The E step calculates the expected correspondences for a given map. These expectations are simply the probabilities for each of the possible “causes” of the sensor measurements. The M step generates a new map for a fixed set of expectations by minimizing an energy function. In [89], first scale invariant features are detected from the images obtained by triclops camera system and their coordinates in 3D are found after matching corresponding pairs. Then successive frames are matched and displacements of these landmarks through time are found. Finally, ego-motion is calculated using least squares minimization. Also in [14] SLAM is implemented with stereo vision where repeatable long term localization is achieved using only naturally occurring, automatically detected features.

2.7 Virtual Environment Applications

Real robotic applications are very complicated because besides the problems of finding how the robot should behave to complete the task at hand, the problems faced while controlling the robot's internal parameters brings high computational load. The problem to be solved is not only the navigation procedure but also to move the robot to the desired location by making the wheels turn or feet step in a balanced way. Thus, first working in a simulated environment in order to find the strategy to be followed by the robot and then applying this on real robot for real applications is preferable. Thus, many studies prefer to work on simulations while producing their algorithm. After reaching a high level of performance, the algorithms could then be applied on real robots, of course, with necessary modifications.

In Terzopoulos and Rabie [80,90] biologically inspired active vision system is implemented on artificial fishes in a virtual environment. Each eye of a fish is implemented as four coaxial virtual cameras to approximate the spatially nonuniform, foveal/peripheral imaging capabilities typical of biological eyes. The system consists of two modules: a foveation module and a stabilization module. These enable the artificial fish to stabilize the visual target in its field of view, foveate the target, and visually navigate towards the target. In Jerbic et. al. [41] the planning of intelligent robot behavior in simulated environment is investigated. Action plan and work space structure, are stored in a list and in a shadowed neural network respectively. In [87] simulation of the environment and a virtual camera taking snapshots from this environment are used to improve a real robot's self-localization where real camera snapshots are taken by an on-board camera. In [55] simulation of a corridor world is constructed. A real robot is run by an operator to obtain images. Real images are inserted into virtual corridors as texture. Then virtual and real robots are let to move. Robots compare what they see and what they memorized and then move accordingly. In [97], computer simulations are used to compare exploration efficiency in a 3D field with cognitive map, without cognitive

map and with random exploration. In Quoy et. al. [79] a learning procedure is added on the links of the cognitive map which enables to reinforce particular paths, and to forget others, allowing for an adaptation to a changing perception of the environment, as it is gradually discovered by the animate. In [69] a humanoid robot which has stereo vision system and a 3D environment are simulated as a computer program. The algorithm for the problem of vision based behavior consisting of local map generation, planning and navigation is developed in simulation and then it is applied on real robots. Image processing to obtain RGB color, depth and optical flow are present where the robot's duty is to find and track a red ball.

CHAPTER 3

BIOLOGICAL STEREO VISION WITH MULTI SCALE PHASE BASED FEATURES

3.1 Introduction and Motivation

In this part of the thesis we propose a sparse disparity algorithm. Instead of corners which are very sparse, we prefer edges of high information as features to be matched. We inspired from the work of Ludke and Hancock [51] in finding our features. In their study, population coding of a bank of 8 complex Gabor filters of different orientation is used to extract features. The orientation selective complex cells found in a cortical hyper column are modeled by the response moduli of a bank of complex Gabor filters. The local maximum search in order to obtain distinctive points is performed and only points of high contrast and high certainty "survive". These points are usually located at object boundaries.

In our algorithm we used multi-scale phase information in order to match our sparse features. In doing this, we inspired from the biological disparity encoding cell models where phase is used to encode disparity. In the experimental studies of Anzai et. al. [1, 2, 3] phase shift model of binocular cell was proposed. In their model receptive fields of a binocular cell are at the same position in the two eyes but have phase differences. Their study also shows that besides phase shift model, position shift model is also available with the general receptive field structure of simple cells. In the position shift model, the receptive field profiles are assumed to

have identical shape in the two eyes, but are centered at non-corresponding points on the retina.

Using phase difference in complex Gabor filters to decode disparity is not limited to models of complex cells using phase differences only. Jenkin and Jepson [37-39] and Sanger [84] describe promising methods based on the output phase behavior of band-pass Gabor filters. Fleet, Jepson and Jenkin [39] discuss further justification for such techniques based on the stability of band-pass phase behavior as a function of typical distortions that exist between left and right views. Recently, Carneiro and Jenkin provide multi-scale phase-based stable features [8, 9].

Our approach is as follows: We commence from feature points detected using steerable filtering method [26] as being done in [18]. With this method, we have feature points with orientation information. Next, phase at different scales are calculated and a phase vector is formed for each feature point. Then, correspondences are estimated using the similarity of phase at multiple scales where magnitude is used as weighting. In this way we avoid the singular points encountered in the method of Jenkin and Jepson [38-39]. After calculating disparity from the positional difference between corresponding points, fine-tuning in disparity is performed using the phase difference information. We also propose a probabilistic model for corresponding point matching. In the following sections, extraction of features using population coding by the method of Ludke [51], our feature extraction method using steerable filters, disparity estimation, fine tuning in disparity, depth calculation and our probabilistic model are explained in the given order. Also the flow chart of our stereo vision algorithm is given in Figure 2.

3.2 Feature Extraction by Population Coding Method

Gabor filters (Eqs 6,7) are well known models of orientation selective cells in striate cortex [13]:

$$g(x, y, \omega_0, \theta) = \exp - \left[\frac{x^2}{2\sigma_x{}^2} + \frac{y^2}{2\sigma_y{}^2} \right] * \cos[2\pi\omega_0 (x\cos\theta + y\sin\theta)] \quad \text{Eq 6}$$

$$g(x, y, \omega_0, \theta) = \exp - \left[\frac{x^2}{2\sigma_x{}^2} + \frac{y^2}{2\sigma_y{}^2} \right] * \sin[2\pi\omega_0 (x\cos\theta + y\sin\theta)] \quad \text{Eq 7}$$

Here σ_x, σ_y express width of 2D Gaussian envelope along x and y direction which can be considered the radius of the receptive field, ω_0 is the spatial frequency and θ gives the orientation in space.

Experiments show that adjacent simple cells have the same orientation and spatial frequency, but are in quadrature pairs (i.e. they differ in spatial phase by 90^o) [15]. Thus a simple cell pair can be expressed by a complex Gabor filter which can encode phase:

$$g(x, y, \omega_0, \theta) = \exp\left\{ - \left[\frac{x^2}{2\sigma_x{}^2} + \frac{y^2}{2\sigma_y{}^2} \right] + i2\pi\omega_0 [x\cos\theta + y\sin\theta] \right\} \quad \text{Eq 8}$$

Although it is clear that cortical neurons are capable of responding to a diversity of feature contrast patterns, orientations and scales, combinational models of how to combine these responses have also proved quite elusive. Gabor filter banks provide rather coarse estimates of feature orientation unless the full range of orientations is sampled with a large number of filters, which is obviously highly inefficient. Recently, however, there has been a suggestion that neuronal ensembles of the sort encountered in cortical hyper columns can be conveniently encoded using a population vector [32]. When population coding is used to represent the convolution responses of the filter bank, the outputs of only a small number of filters need to be combined in order to achieve a considerable improvement of the precision of orientation estimation. In fact, population coding has become an essential paradigm

in cognitive neuroscience over the past decade and is increasingly studied within the neural network community. In the vision domain, in [96] a model of population vector coding of visual stimulus orientation by striate cortical cells is examined. Based on the ensemble of broadly orientation-tuned units, the model explains the high accuracy of orientation discrimination in the mammalian visual system.

Inspired from all these findings, the orientation selective complex cells found in a cortical hyper column are modeled by the response moduli of a bank of eight complex Gabor filters by Ludke and Hancock [51]. From the output of the filter-bank, a population vector is computed as:

$$\mathbf{p}(x,y) = \begin{bmatrix} p_x(x,y) \\ p_y(x,y) \end{bmatrix} = \sum_{i=1}^{n} \mathbf{G}(x,y,\omega_0,\theta_i)\mathbf{e}_i \qquad \text{Eq 9}$$

where *(x,y)* is the position of the pixel in the image, *n* is the number of different orientation states, $\mathbf{G}(x,y,\omega_0,\theta_i)$ is the complex response (energy) of a quadrature pair of Gabor filters with orientation θ_i and $\mathbf{e}_i$ is the unit vector in the direction θ_i. Here, the population vector is the vector sum of the *n*=8 filter response vectors and the resultant orientation is given by:

$$\theta_{pop}(x,y) = \arctan\left[p_y(x,y) / p_x(x,y)\right] \qquad \text{Eq 10}$$

It is very interesting that simple vectorial addition of the individual filter responses produces a population vector which accurately encodes the orientation response of the hyper columnar ensemble. Although each individual filter has very broad orientation tuning, the vectorial combination of the set of responses can yield a much better estimate of local stimulus orientation. Also a certainty measure, *C(x,y),* is calculated which characterizes the reliability of the orientation measurement independent of contour contrast [51]. Certainty is defined as the angular variance of the response energy distribution. This allows distinguish contour points from noisy regions. The local maximum search in order to obtain

distinctive points, is performed on the product of certainty and response energy, $\|\mathbf{p}(x,y)\|C(x,y)$. As a result only points of high contrast and high certainty "survive". These points are usually located on object boundaries.

In Figure 4 we show a stereo image pair and feature points obtained from these images using the method explained above. The estimated orientation for each feature is given in colors.

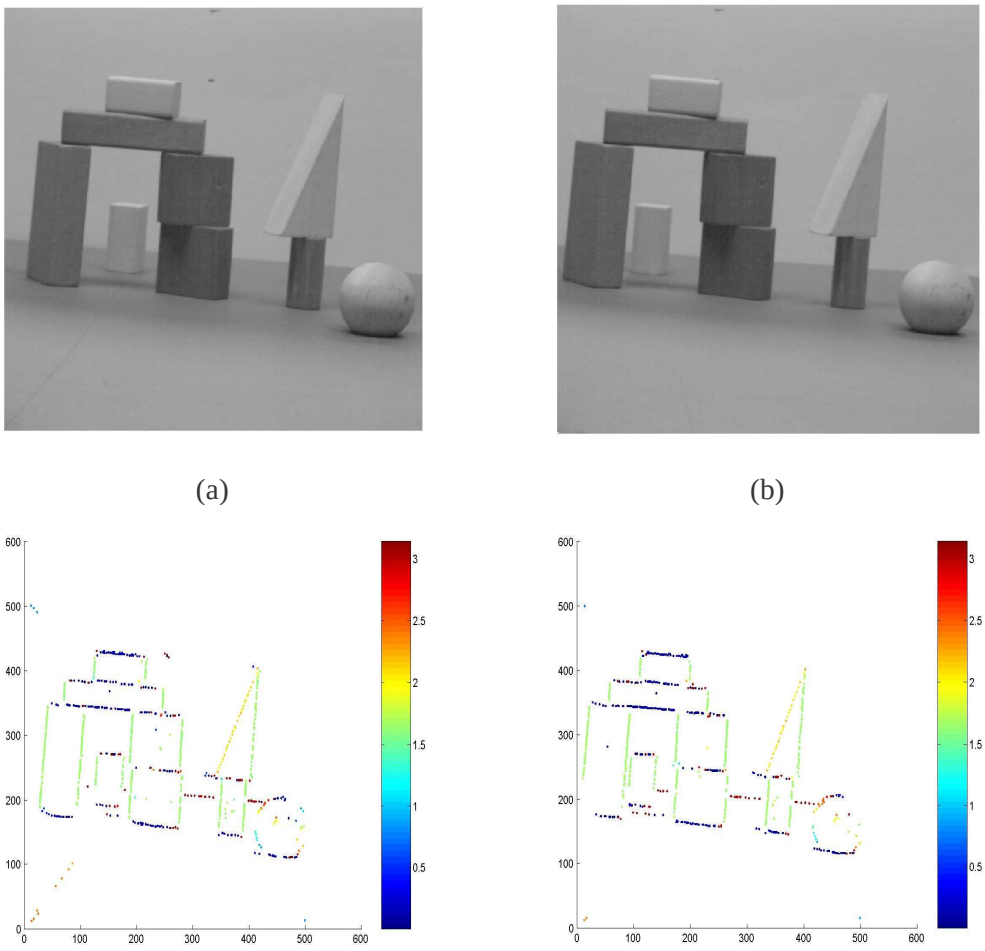

Figure 4 a,b. Stereo image pair (Blocks 1) taken from CMU database, c,d. Corresponding feature points with orientation given in color scale. In this case population coding method has been used.

3.3 Feature Extraction Using Steerable Filters

Keeping the same idea of orientation selective cells and hyper column structure in the visual cortex which was modeled in the population vector method given in the previous subsection, feature points used in our study are found by using steerable filters as been done in [18].

Steerable filters are template filters whose arbitrarily rotated versions can be synthesized by taking linear combinations of finite number of basis filters. Steerable filters are attractive as it allows one to work in continuum of orientations. All Gaussian derivatives are steerable and the orientation selectivity of the filter increases with the increasing derivative order *m* [26]. The analytic filter $h(\mathbf{x})$ (Figure 5) to be used as the template filter is constructed from the filters provided in the appendix [26] as follows where $\mathbf{x} = (x,y)$ is the pixel location in the image ***I***:

$$\begin{aligned} h(\mathbf{x}) &= g(\mathbf{x}) + jq(\mathbf{x}) \\ g(x,y) &= \left(0.934 - 3.738x^2 + 1.246x^4\right)e^{-\left(x^2+y^2\right)} \\ q(x,y) &= \left(2.858x - 2.982x^3 + 0.3975x^5\right)e^{-\left(x^2+y^2\right)} \end{aligned} \qquad \text{Eq 11}$$

For the multi-scale framework used in this study, $g(\mathbf{x})$ is chosen to be 4th derivative of a Gaussian, which is a steerable filter and $q(\mathbf{x})$ is chosen to be a steerable approximation to the Hilbert Transform of $g(\mathbf{x})$. For an arbitrary θ, $g_\theta(\mathbf{x})$ can be synthesized using 5 basis filters of 0˚, 36˚, 72˚, 108˚, 144˚ as in Eq 12, and $q_\theta(\mathbf{x})$ can be synthesized using 6 basis filters of 0˚, 30˚, 60˚, 90˚, 120˚, 150˚ as in Eq 13 where $\mathbf{R}_{\theta_i}$ is the rotation matrix. Scaling is done at three levels where the interval between the minimum scale and the maximum scale is divided linearly in 3 intervals. In this study filter widths vary between six pixels and 18th pixels.

$$g(\mathbf{R}_\theta \mathbf{x}) = \sum_{i=1}^{5} \frac{1}{5}\left(1 + 2\cos(2(\theta - \theta_i)) + 2\cos(4(\theta - \theta_i))\right) g\left(\mathbf{R}_{\theta_i}\mathbf{x}\right) \qquad \text{Eq 12}$$

$$q(\mathbf{R}_\theta \mathbf{x}) = \sum_{i=1}^{6} \frac{1}{6}\left(2\cos(\theta - \theta_i) + 2\cos(3(\theta - \theta_i)) + 2\cos(5(\theta - \theta_i))\right) q\left(\mathbf{R}_{\theta_i}\mathbf{x}\right) \qquad \text{Eq 13}$$

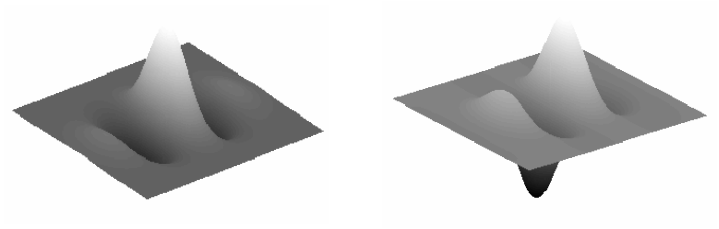

(a) (b)

Figure 5 The template filter used in analysis. a. The real part which is the 4th derivative of Gaussian, b. The Imaginary part which is a steerable approximation to the Hilbert transform of the real part.

After defining the filters, as the first step, the image is filtered with basis filters at three different scales and at each scale these are used to interpolate the filtered images of orientation between 0º to 180º with 10º degrees of interval by using equations 12 and 13. Then, the orientation estimation, $\tilde{\theta}(\mathbf{x})$, is done as follows:

$$\tilde{\theta}(\mathbf{x}) = \arg\max_{\theta} \sum_{n=1}^{S} r_{n,\theta}(\mathbf{x}) \qquad \text{Eq 14}$$

where $r_{n,\theta}(\mathbf{x})$ is the response of steerable filtering for scale n and orientation θ and S is the number of scales. At the final step, $\left|\sum_{n=1}^{S} r_{n,\tilde{\theta}}(\mathbf{x})\right|$ is thresholded and feature points are extracted. For the stereo pair given in Figure 4 the feature points are obtained and shown in Figure 6 with their orientation in color.

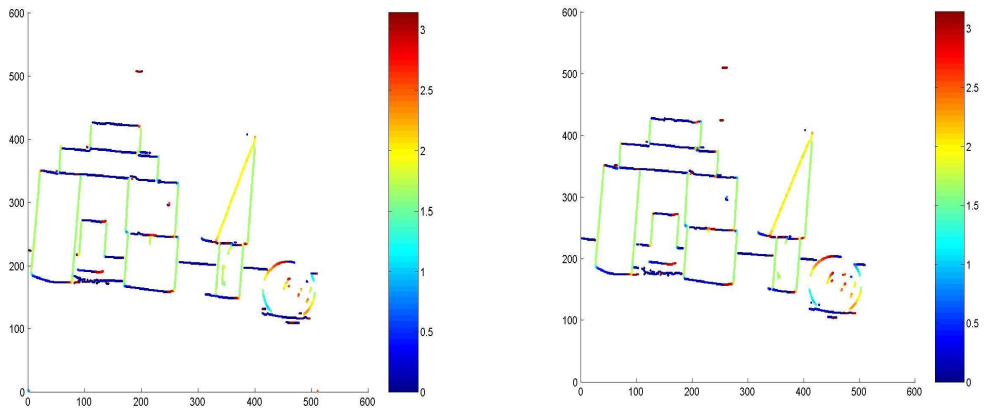

(a) (b)

Figure 6 Feature points obtained by steerable filtering for the Blocks 1 stereo image pair given in Figure 4. The orientation is given in color scale.

In population coding method [51] explained in the previous section, the images are filtered with 8 different oriented complex Gabor filters at a predefined wavelength. Since only one scale is considered this makes 16 times filtering. Population vector for each pixel location is calculated by summing the 8 different oriented complex filter responses. Also a certainty measure is calculated for each pixel. Feature points are selected to be the local maximum of the product of population vector magnitude and certainty.

In steerable filtering method used in our study, 5 and 6 orientations are considered for the real and the imaginary part of the complex filter respectively. In this case any number of scaling is allowed and this makes (5+6)*n filtering where n is the number of scales allowed. In order to find the best representative orientation for each pixel, filter responses are calculated for each scale for the interval between 0˚ and 180˚ with 10˚ steps using the already obtained filter responses. The orientation of a pixel location is selected to be the orientation which gives the

maximum sum of responses over scales. Feature points are selected using global thresholding over the sum of responses at the estimated orientations.

Both of these methods use very similar filters however the population vector method [51] is single scale but the steerable filter method used in our study is multi-scale. In order to show the importance of using multi-scale in extracting features, we show feature points extracted using steerable filters with different number of scales in Figure 7.

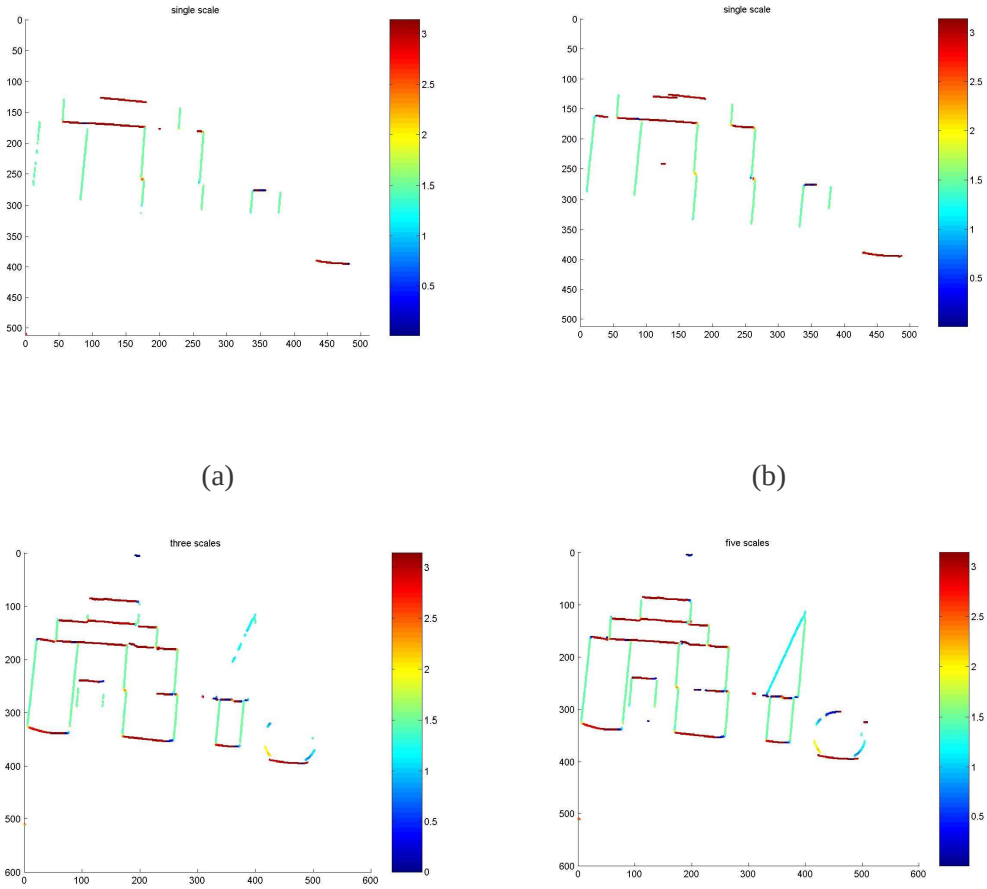

(a) (b)

(c) (d)

Figure 7 Feature points extracted using filters at different number of scales. a. Single scale where width of the filter is 6 pixels, b. Single scale where width of the filter is 18 pixels, c. Three scales where filter widths are 6, 12 and 18 pixels, d. Five scales where filter widths are 6,10,14,18,22 pixels.

3.4 Finding Corresponding Pairs Using Multi-scale Phase

The main attributes used in this thesis for the corresponding pair matching of feature points are multi-scale phase and amplitude. While extracting the feature points as explained above we also obtain orientation information for each feature point. Using this orientation information we calculate phase at each feature point as follows:

$$\phi_i = \arctan\left[\frac{real(r_{n,\theta}(\mathbf{x}_i))}{imag(r_{n,\theta}(\mathbf{x}_i))}\right] \qquad \text{Eq 15}$$

Here, the quantity ϕ_i is the phase at feature point *i*, $real(r_{n,\theta}(\mathbf{x}_i))$ and $imag(r_{n,\theta}(\mathbf{x}_i))$ are real and imaginary parts of the filtered image respectively where $\mathbf{x}_i$ is the coordinate of feature point *i*, *n* and θ are the scale and orientation of the filter applied at feature point *i*. We use the phase measurements for filters of different width, i.e. different scales, to locate correspondences. We use three filters where the width of the narrowest filter is six pixels and the largest filter is 18 pixels. Let $\mathbf{\Phi}_i = [\phi_1 \ \phi_2 \ \phi_3]^T$ be a vector of phase estimates obtained using these filters. For each feature point at the left image, we search over a window for feature points of similar phase vector in the right image.

We measure the similarity of phase vectors by taking the dot product of the phase vectors (Eq 16). The candidate $\hat{j}$ which has the largest weighted phase vector dot product with feature point *i* is the one that satisfies the condition. In Eq 16, $\bullet$ is used for vector dot product and * is used for element by element vector product. Weighting vector $\boldsymbol{C}_{ij}$ (Eq 17) is constructed by using the method described in [84]. Each element c_{ij}^n shows how similar the magnitudes of feature points *i* and *j* at scale *n* (Eq 18). Hence, it is the confidence value of the pair *i-j*.

$$\hat{j} = \arg_{j}\left\{\max\left\{\mathbf{\Phi}_i \bullet (\mathbf{\Phi}_j * \mathbf{C}_{ij})\right\}\right\} \quad \text{Eq 16}$$

$$\mathbf{C}_{ij} = \begin{bmatrix} c_{ij}^1 \\ c_{ij}^2 \\ c_{ij}^3 \end{bmatrix} \quad \text{Eq 17}$$

$$c_{ij}^n = \min\left(\frac{|r_{n,\theta}(\mathbf{x}_i)|}{|r_{n,\theta}(\mathbf{x}_j)|}, \frac{|r_{n,\theta}(\mathbf{x}_j)|}{|r_{n,\theta}(\mathbf{x}_i)|}\right) \quad \text{Eq 18}$$

The matching algorithm explained above is cross checked for left to right correspondences and right to left correspondences. In this way, we may discard occluded feature points and unsafe matches. For the stereo pair shown in Figure 4 we find correspondences for 537 out of 980 feature points in the right-hand image.

3.5 Finding Disparity and Depth

Once the cameras are calibrated, that is, the internal parameters of cameras like focal length and principle point, and the camera pose (the position and orientation of the camera in a given common coordinate system) are known, the 3D coordinate of a point can be found, if its projections on at least two images are available.

Assuming that corresponding points are available, 3D location of the point P can be found by finding the intersection point of the lines passing through the camera center and the projection of P in the images. In Figure 8 the projection of point P on left and right images are denoted by P_1 and P_2. The lines starting from the projection points and passing through the camera lenses converge at point P. In this case, cameras are assumed to be parallel thus epipolar lines are aligned and in the horizontal direction. Epipolar lines are the intersection of the image planes with the plane formed by the focal centers and the object point.

In rectified pairs, i.e. epipolarly aligned images, the difference between the projections of the point P on the image planes is known as the disparity, δ, and is inversely proportional to the depth which is the distance of the object point to the reference camera. In our case depth can be calculated as follows:

$$d=b*f/\delta \qquad \text{Eq 19}$$

where d is the depth of the point P in the space, i.e. the distance of point P from the plane of the lenses, b is the baseline, i.e. distance between the two lenses, f is the focal length of the lenses, i.e. the distance of the imaging plane (retina in the human eye) to the lenses, δ is the disparity of point P, i.e. the distance between the projection of point P on two image planes.

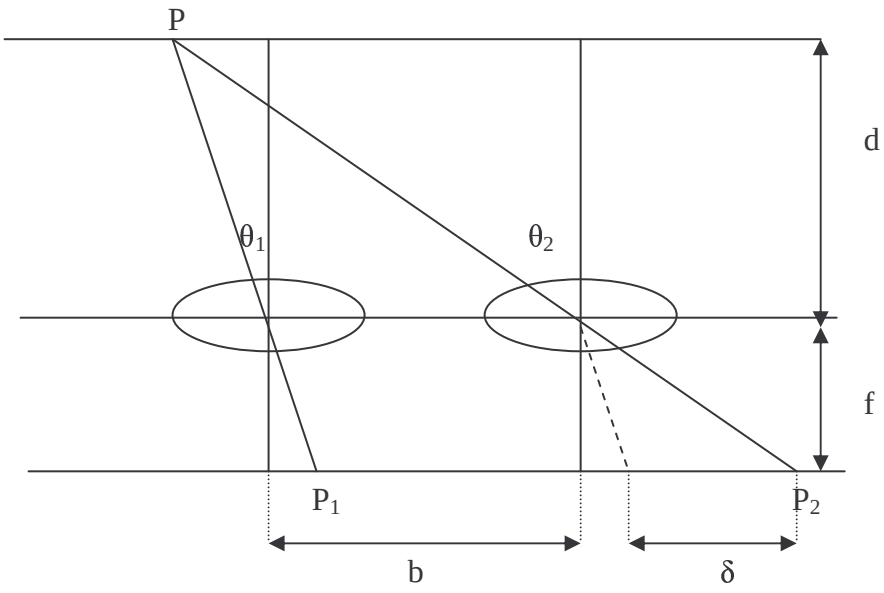

Figure 8 Stereo camera projection system.

In this study, we also work on stereo image pairs where parallel cameras are used. This means that the epipolar line is in the horizontal direction and the disparity is the horizontal pixel distance between corresponding feature point

locations, i.e. $\delta = x_i - x_{\hat{j}}$. This disparity calculation is also in parallel to the models of binocular disparity selective cells where there exists position shift between the receptive fields of binocular cells [15].

The disparity values calculated for the stereo pair given in Figure 4 are displayed in Figure 9. Out of the 537 matched feature points only 62 are in error, hence the success rate is 90%. Most of the errors are for feature points having a population vector orientation in the disparity direction.

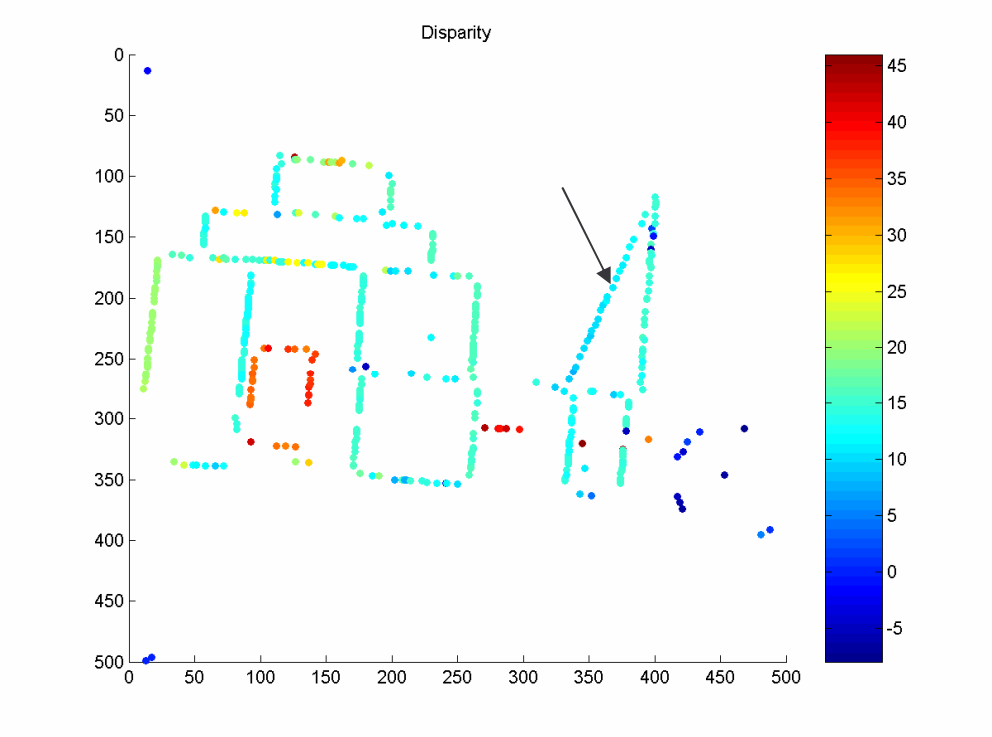

Figure 9 Disparity estimated for the Blocks 1 image pair.

In order to obtain sub pixel accuracy, we apply a fine tuning on the rough disparity values. In fine tuning, the phase shift model of binocular cell receptive fields is mimicked [15]. The amount of fine tuning ($\Delta\delta$) is calculated from the intraocular phase differences between corresponding points as follows:

$$\Delta\delta = \phi_{ij}^{n} * \lambda^{n} / 2\pi \qquad \text{Eq 20}$$

Here $\phi_{ij}^{n} = \phi_{i}^{n} - \phi_{j}^{n}$ is the measured phase difference at scale *n* between corresponding feature points where *i* and *j* are the corresponding feature point indenties and λ^{n} is the wavelength used at scale *n*. In this way, the rough disparity estimate expressed by integer number of pixels is tuned by the phase shift model and sub pixel disparity, D, is calculated as follows:

$$D = \Delta\delta + \delta \qquad \text{Eq 21}$$

In order to express the effect of fine tuning, the rough disparity and fine tuned sub pixel disparity calculated on the edge-segment shown by an arrow in Figure 9 are shown in Figure 10. Here, x-axis of the plot is for the feature points on the edge where neighboring feature points are given successive numbers starting from one and y- axis is the disparity. The ground truth disparity changes from 13 pixels to 9 pixels on this edge. The rough disparity for each feature point is given by '*' and the fine tuned disparity is given by line. As can be seen on the figure, rough disparities are in integer numbers and have a stair shaped structure whereas fine tuned sub-pixel disparity varies smoothly.

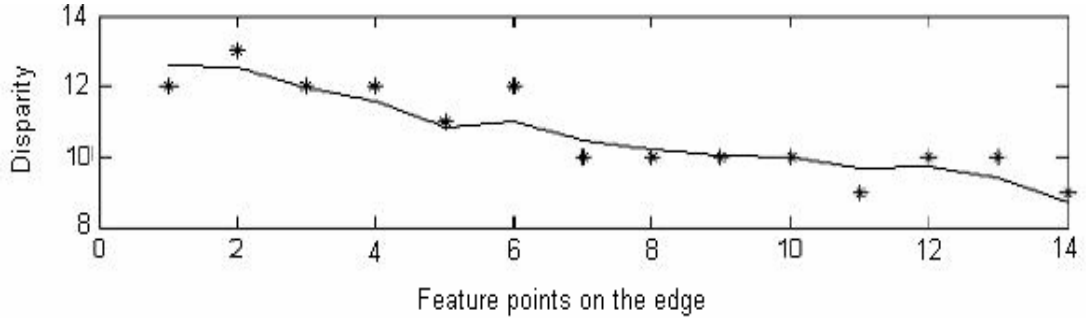

Figure 10 Fine tuning. Feature points are numbered starting from the left-most one through the right-most one and given in the x-axis of the plot. y-axis shows the disparity where rough disparity is given with (*) and fine tuned disparity given with line.

Disparity results for other image pairs are shown in Figures 11-14. Also, the results are summarized in Table 1. Total number of feature points extracted from the right image of the stereo pair, the number of pairs matched, the number of wrong matches among matched pairs and the success rate over number of matched pairs, i.e. the percentage of correct matches over total number of matched pairs, are given in the successive columns of the table from left to right for each stereo pair. Although the image pairs have very different characteristics, the results are still satisfactory. Especially for textured locations in the images, features extracted and multi-scale phase are very informative so that success rate is high.

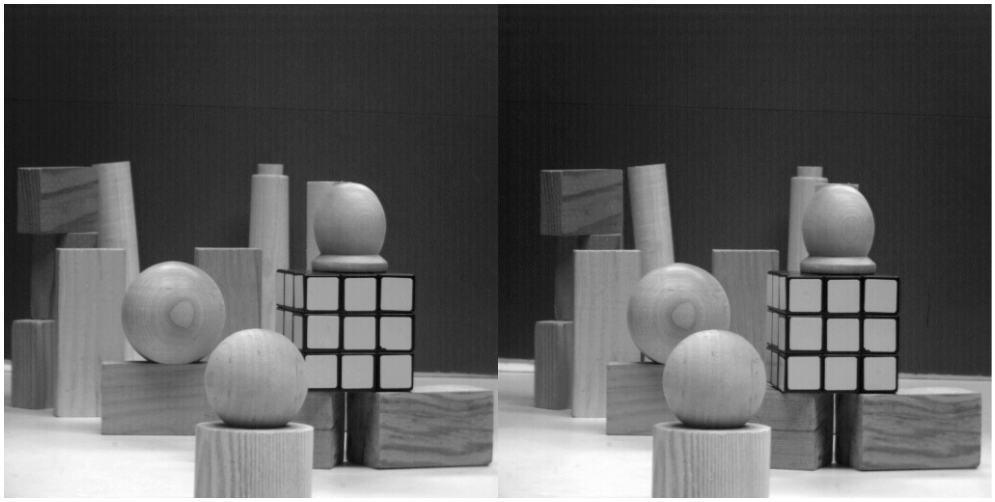

(a) (b)

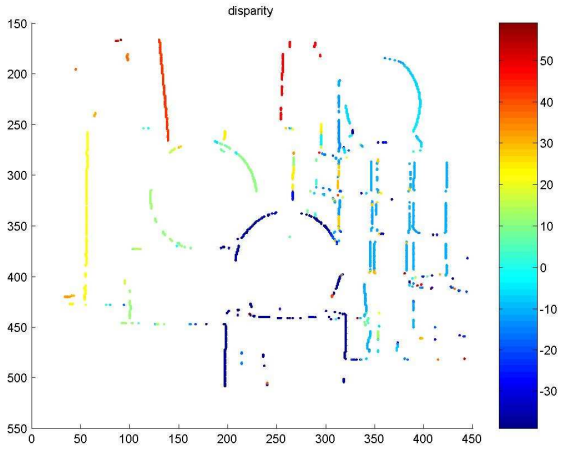

(c)

Figure 11 a. Left image, b. Right image, c. Disparity. Stereo images (Blocks 2) are taken from CMU stereo database.

(a)

(b)

(c)

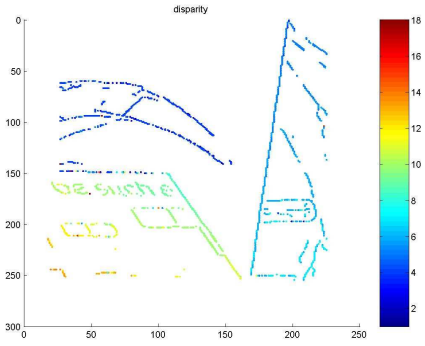

(d)

Figure 12 a Left image, b. Right image, c. Disparity. Stereo images (Venus stereo pair) are taken from Middlebury Stereo webpage.

(a)

(b)

(c)

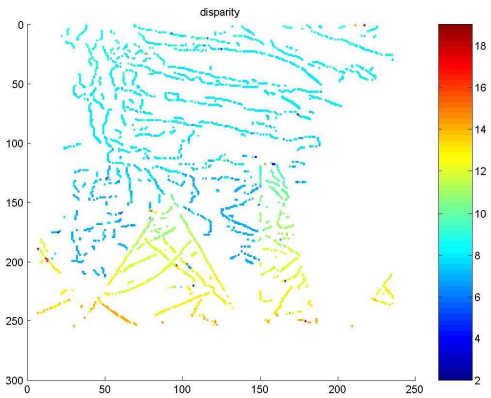

(d)

Figure 13 a. Left image, b. Right image, c. Disparity. Stereo images (Sawtooth stereo pair) are taken from Middlebury Stereo webpage.

(a)

(b)

(c)

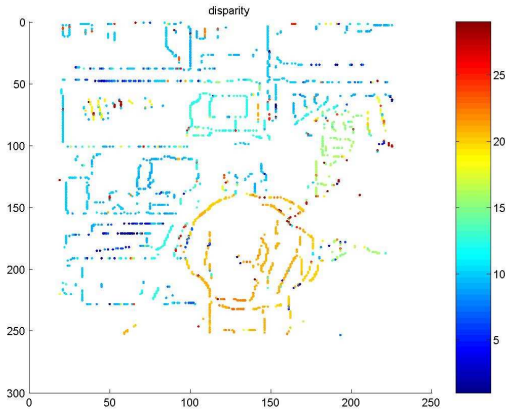

(d)

Figure 14 a. Left image, b. Right image, c. Disparity. Stereo images (Tsukuba stereo pair) are taken from Middlebury Stereo webpage.

Table 1 Success rate of the algorithm for different stereo pairs.

Image pair	Number of feature points extracted	Number of pairs matched	Number of mismatches	Success rate (%) over number of matched pairs
Blocks 2	3847	1265	340	73
Venus	1884	1163	65	94
Sawtooth	4288	2938	140	95
Tsukuba	4088	2089	352	83

In [95] some feature point matching strategies are compared. In their study they use corners detected by Plessey operator [34] as features and apply variance normalized correlation method for matching where the constraints of uniqueness and symmetry are considered also. They select correct matches manually and provide success rates for different stereo image pairs. The only stereo pair in their study which has horizontal as epipolar line is the Tsukuba image pair and they reach a success rate of 71.7% for it whereas we reach 83% success rate with our matching algorithm for the same stereo pair.

Also in [93] corners are detected by Harris corner detector and features are matched based on proximity and similarity of their neighborhood. Matches for nearly 50% of the total features are estimated and RANSAC algorithm [20] is used in order to find the outliers where the success rate for the matching comes out to be 50% for most of the images used in their study.

Also, fine tuning result for some part on the edge shown by an arrow in Figure 12.d is given in Figure 15. Here, x-axis of the plot is for the feature points on the edge where neighboring feature points are given successive numbers starting from one and y- axis is the disparity. The ground truth disparity changes from six pixels to seven pixels on this part of the edge. The rough disparity for each feature point is

given by ‘*’ and the fine tuned disparity is given by line. As can be seen on the figure, rough disparities of feature points are in integer numbers and same for all feature points although they are slanted and should have slightly different disparity values. Fine tuned sub-pixel disparity varies smoothly starting from just above six pixels and extends to seven pixels.

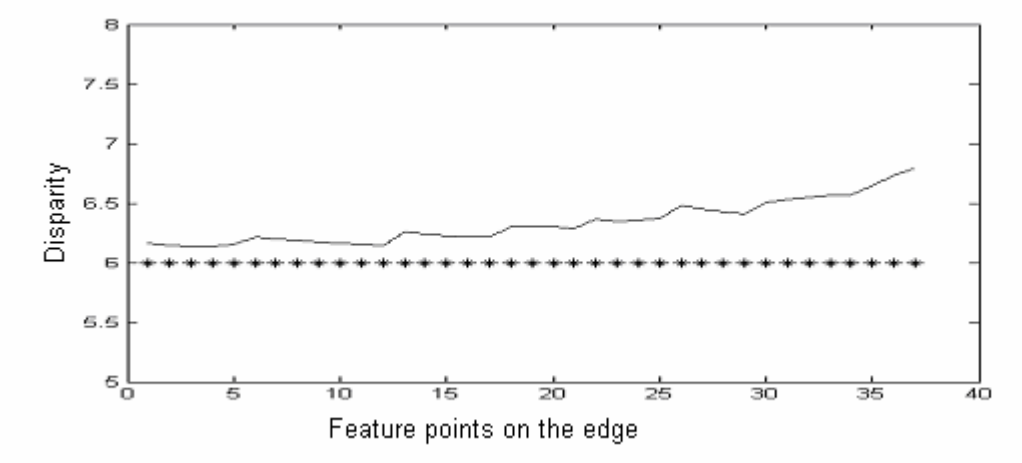

Figure 15 Fine tuning. Feature points are numbered starting from the left-most one through the right-most one and given in the x-axis of the plot. y-axis shows the disparity where rough disparity is given with (*) and fine tuned disparity given with line.

In order to show the importance of using multi scale instead of single scale in matching, we present disparity maps obtained using a single scale and three scales in Figure 16. In both cases left to right and right to left double checking is performed in order to get only relevant results. In the top image of Figure 16 result given is in the case when only a single scale phase is used in matching. In the bottom image results when multi-scale is used. Using multi-scale phase brings more reliable results with more number of points.

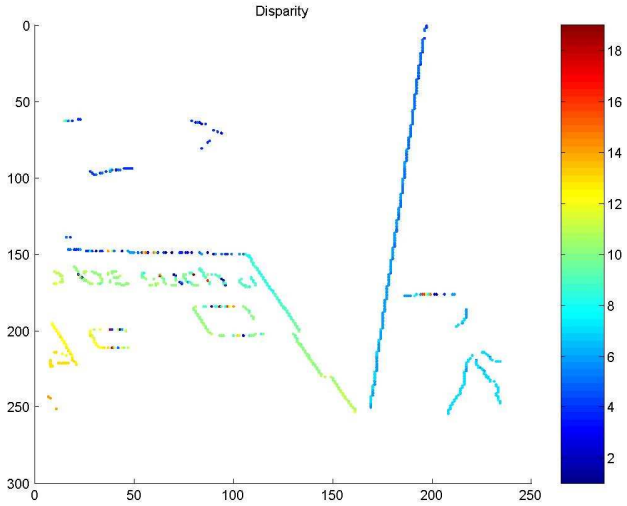

(a)

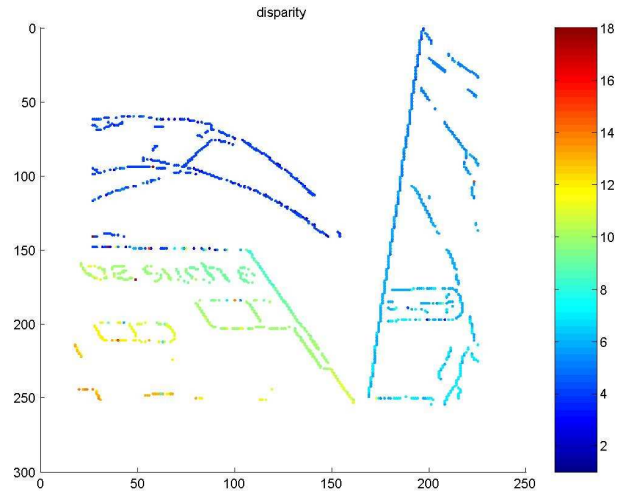

(b)

Figure 16 Disparity calculated for Sawtooth stereo pair using: a. Single scale where filter width is six pixels, b. Three scales where filter widths are 6, 12 and 18 pixels.

3.6 Complexity of the Algorithm

There are four main steps in the algorithm. These steps are filtering of the image with steerable filters at three scales, thresholding in order to select feature points, checking similarity in multi-scale phase in order to find corresponding pair and fine tuning. Each of these steps is summarized below.

Filtering:

```
for i=1:N,
        for j=1:N,
                for s=1:S,
                        for ir=real,imaginary,
                                for r=1:R,
                                        filter I(i,j) by n_s x n_s window at orientation r)
                                end
                        end
                        for rd=1:RD,
                                calculate complex filter response for orientation od
                                from real and imaginary filter responses obtained
                                above
                        end

                        comparison for maximum response magnitude over RD for
                        each (i,j) at each scale s
                end
        end
end
```

Thresholding:

```
for i=1:N,
        for j=1:N,
                if sum of responses over scales is greater than a threshold, pixel (i,j)
                is selected as a feature point
        end
end
```

Similarity Check:

```
for i=1:N,
        for j=1:N,
                for d=1:D,
```

```
                    find dot product of phase vector at pixel location (i,j) in one
                    image and phase vector at (i,j+d) in the other image where
                    vectors have dimension of 1xS
                end
                find disparity d for which the dot product is maximum
        end
end
```

Fine Tuning:

```
for i=1:N,
        for j=1:N,
                calculate phase difference between pairs and estimate subpixel
                disparity
        end
end
```

The parameters which are important for complexity computation, their definition and default values used in our program are given in the following table.

Table 2 Parameters of the algorithm effective for complexity.

Parameter	Definition	Default Value
I	Image	
N	Image size	256
S	Total number of scale	3
R	Total number of main orietations	5
RD	Total number of orientations	18
n_s	Filter window size	12, 24, 48 for scales 1 to 3
D	Disparity search range	20

After filtering and thresholding we obtain feature point locations and phase and magnitude values for each feature point location. This takes nearly 2 seconds in time which is normal since each pixel is filtered with S*2*O number of filters where S is for total number of scales, O is for total number of basic orientations and

2 is for real and imaginary parts of the complex filters. The matching step is completed in 63 milliseconds.

The complexity of the system is calculated as follows:

$$O(N^2 R\sum_{s=1}^{S} n_s^2) + O(N^2) + O(N^2 DS) + O(N^2) \quad \text{Eq 22}$$

where first term is for filtering step, second term is for thresholding step, third term is for checking similarity step and last term is for the fine tuning step. For single scale, the complexity is simplified to $O(N^2 Rn^2)$ and for multiple scales it comes out to be $O(N^2 RSn^2)$ where n is assumed to be the width of the widest filter.

3.7 Probabilistic Model of the Disparity Algorithm

After finding correspondences and computing the associated disparities, we model the distribution of phase differences between corresponding pairs. In order to model a phase distribution, a circular distribution would be appropriate because of the periodicity property of the phase. One of the circular distributions which is appropriate for this purpose is the von Mises distribution.

The probabilistic modeling of the disparity algorithm is done as follows: First, von Mises distribution is fit to phase differences between corresponding feature points of Venus stereo pair. This is done once for each scale. Then, an equation for probability of being a pair is proposed. Finally, the model is tested for its performance on different images. Results show that although the model is based on Venus stereo pair only, it works fine for other images such as Blocks 2, Sawtooth and Tsukuba as well.

3.7.1 Probability Density Estimation of Phase Differences by von Mises Model

The general form of the von Mises distribution is given by the formula:

$$p(\phi_k \mid \kappa, \mu) = \frac{1}{2\pi I_0(\kappa)} \exp[\kappa \cos(\phi_k - \mu)] \qquad -\pi < \phi < \pi \qquad \text{Eq 23}$$

where ϕ_k , k=1.....K, are the data points of finite number (here phase differences between pairs), μ is the mean and κ is the width of the distribution. Here I_0 is the zeroth order Bessel function.

Mixture model for the von Mises density is the linear combination of component density in the form given in Eq 23. Here W gives the total number of von Mises distributions used. $P(w)$, κ_w, μ_w are the adjustable parameters where κ_w, μ_w are the density function parameters and $P(w)$ is called the mixing parameter. It can also be called the prior probability of the data point having been generated from component w of the mixture. These priors are chosen to satisfy the constraints $\sum_{w=1}^{W} P(w) = 1$ and $0 \le P(w) \le 1$. Similarly, the component density functions are normalized so that $\int p(\phi_k \mid \kappa_w, \mu_w) d\phi_k = 1$.

$$p(\phi_k) = \sum_{w=1}^{W} p(\phi_k \mid \kappa_w, \mu_w) P(w) \qquad \text{Eq 24}$$

Having decided on a parametric form for density function, $p(\phi_k)$, mixture of von Mises in this case, the next stage is to use the data set to find values for the parameters. One of the principle approaches for the solution to this problem is maximum likelihood. Maximum likelihood seeks to find the optimum values for the parameters by maximizing a likelihood function (Eq 24) derived from the training set. In practice it is often convenient to consider the negative logarithm of the likelihood (Eq 25) which is minimized instead of maximization.

$$\ell(\phi_k) = \prod_{k=1}^{K} p(\phi_k) \qquad \text{Eq 25}$$

$$E = -\ln \ell(\phi_k) = -\sum_{k=1}^{K} \ln p(\phi_k) \qquad \text{Eq 26}$$

Using the mixture density of von Mises distribution, the log likelihood for the data set can be given by:

$$E = -\ln \ell(\phi_k) = -\sum_{k=1}^{K} \ln\, p(\phi_k) = -\sum_{k=1}^{K} \ln\left\{ \sum_{w=1}^{W} p(\phi_k \mid \kappa_w, \mu_w) P(w) \right\} \qquad \text{Eq 27}$$

One of the methods to find the parameters $P(w)$, κ_w, μ_w is to take the derivative of E with respect to the parameter and solve by equalizing the result to zero. This way a direct method to calculate the parameters can not be provided. In fact highly non-linear coupled equations are represented. Thus, an iterative scheme would be better for finding the minimum of E. An iterative scheme could be as follows: First initial guesses for the parameters are made which are called 'old' values. Then the right hand sides of the derivatives explained above are solved and this gives a revised estimate for the parameters and these revised parameters are called as 'new'. These parameter values are then become the 'old' values and the process is repeated. This way at each iteration the error function decreases until a local minimum is found. This is also a special case of a more general procedure known as the expectation-maximization (EM) algorithm.

The change in error when we replace the old parameter values by the new values can be written as in Eq 27 where $p^{new}(\phi_k)$ denotes the probability density evaluated using the new values for the parameters while $p^{old}(\phi_k)$ represents the density evaluated using the old parameter values.

$$E^{new} - E^{old} = -\sum_{k} \ln\left\{ \frac{p^{new}(\phi_k)}{p^{old}(\phi_k)} \right\} \qquad \text{Eq 28}$$

Using the definition of mixture distribution given by Eq 23 it can be re-written as follows [6]:

$$E^{new} - E^{old} = -\sum_{k} \ln\left\{ \frac{\sum_{w} P^{new}(w)\, p^{new}(\phi_k|w)}{p^{old}(\phi_k)} \frac{P^{old}(w|\phi_k)}{P^{old}(w|\phi_k)} \right\} \qquad \text{Eq 29}$$

where $p(\phi_k \mid w)$ is used instead of $p(\phi_k \mid \kappa_w, \mu_w)$ and $P(w \mid \phi_k)$ is used instead of $P(\kappa_w, \mu_w \mid \phi_k)$ for simplicity and the last term is simply the identity. Making use of the Jensen's equality [6] the equation becomes:

$$E^{new} - E^{old} \leq -\sum_{k} \sum_{w} P^{old}(w|\phi_k) \ln\left\{ \frac{P^{new}(w)\, p^{new}(\phi_k \mid w)}{p^{old}(\phi_k) P^{old}(w \mid \phi_k)} \right\} \qquad \text{Eq 30}$$

We wish to minimize E^{new} with respect to the 'new' parameters. If we let Q be the right hand side in Eq 29 then we have $E^{new} \leq E^{old} + Q$ and so $E^{old} + Q$ represents an upper bound on the value of E^{new}. Thus minimizing Q will necessarily lead to a decrease in the value of the E^{new} unless E^{new} is already at a local minimum. If we drop the terms which depend on the 'old' parameters, Q is rephrased as follows where 'n' is used instead of 'old' and 'n+1' is used instead of 'new' in order to emphasize the iterative process:

$$\tilde{Q}^{(n+1)} = -\sum_{k=1}^{K} \sum_{w=1}^{W} P^{(n)}(w \mid \phi_k) \ln\left\{ p(\phi_k \mid \kappa_w{}^{(n+1)}, \mu_w{}^{(n+1)}) P^{(n+1)}(w) \right\} \qquad \text{Eq 31}$$

This function can be minimized with respect to the 'new' parameters at iteration 'n+1'. For $\kappa_w{}^{(n+1)}, \mu_w{}^{(n+1)}$ this minimization is straight forward. The derivative of the function with respect to the parameter will be equalized to zero and the result will be solved for the parameter.

The update equation for $\mu_w^{(n+1)}$ is given in Eq 31. The solution is straight forward if the posterior probabilities and the Bayes' theorem (Eq 32, 33) are inserted in Eq 31 then Eq 31 becomes as in Eq 34. The posterior probabilities also satisfy $\sum_{w=1}^{W} P(w|\phi_k) = 1$.

$$\mu_w^{(n+1)} = 1/2 \arctan\left[\frac{\sum_{k}^{K} P^{(n)}(w|\phi_k)\sin(2\phi_k)}{\sum_{k}^{K} P^{(n)}(w|\phi_k)\cos(2\phi_k)}\right] \quad \text{Eq 32}$$

$$p(\phi_k) = \sum_{w=1}^{W} p(\phi_k | \kappa_w, \mu_w) P(w) \quad \text{Eq 33}$$

$$P(w|\phi_k) = \frac{p(\phi_k | \kappa_w, \mu_w) P(w)}{p(\phi_k)} \quad \text{Eq 34}$$

$$\mu_w^{(n+1)} = 1/2 \arctan\left[\frac{\sum_{k}^{K} \frac{p(\phi_k | \kappa_w^n, \mu_w^n) P^n(w)}{\sum_{w=1}^{W} p(\phi_k | \kappa_w^n, \mu_w^n) P^n(w)} \sin(2\phi_k)}{\sum_{k}^{K} \frac{p(\phi_k | \kappa_w^n, \mu_w^n) P^n(w)}{\sum_{w=1}^{W} p(\phi_k | \kappa_w^n, \mu_w^n) P^n(w)} \cos(2\phi_k)}\right] \quad \text{Eq 35}$$

For $\kappa_w^{(n+1)}$ the solution is not obtained directly but the *R* value is obtained as in Eq 35. For the solution of *R*, which is a value in the range [0-1], the posterior probabilities which are expressed using Bayes' theorem as explained just above are also used.

$$R = \frac{I_1(\kappa_w^{(n+1)})}{I_0(\kappa_w^{(n+1)})} = \frac{\sum_k^K P^{(n)}(w|\phi_k)\cos(2(\phi_k - \mu_w^{(n)}))}{\sum_k^K P^{(n)}(w|\phi_k)} \qquad \text{Eq 36}$$

In this case the inverse solution for $\kappa_w^{(n+1)}$ is required and $\kappa_w^{(n+1)}$ can be calculated as follows:

$$\kappa_w^{(n+1)} \cong \begin{cases} \frac{1}{6}R(12 + 6R^2 + 5R^4) & R \le 0.5 \\ 1/\left[2(1-R) - (1-R)^2 - (1-R)^3\right] & R > 0.5 \\ 1/2(1-R) & R \approx 1 \end{cases} \qquad \text{Eq 37}$$

However, for the mixing parameter *P(w)* this minimization is not straight forward. For the solution we must take account of the constraint $\sum_{w=1}^{W} P(w) = 1$ [6]. This is done by introducing a LaGrange multiplier λ and minimizing the function in Eq 37. Setting the derivative of Eq 37 with respect to $P^{(n+1)}(w)$ to zero, Eq 38 is obtained. The value of λ can be found by multiplying both sides of Eq 38 by $P^{(n+1)}(w)$ and summing over *w*. Finally, the value of λ is computed as in Eq 38. Using the properties $\sum_{w=1}^{W} P^{(n+1)}(w) = 1$ and $\sum_{w=1}^{W} P^{(n)}(w|\phi_k) = 1$, we obtain that λ=*K*. Then the update equation for the mixing parameter *P(w)* comes out to be as in Eq40. Inserting Eq 32 and Eq 33 into Eq 40, the solution is straight forward.

$$\tilde{Q} + \lambda(\sum_w P^{(n+1)}(w) - 1) \qquad \text{Eq 38}$$

$$-\sum_{k=1}^{K}\frac{P^{(n)}(w\mid\phi_k)}{P^{(n+1)}(w)}+\lambda=0 \qquad \text{Eq 39}$$

$$\lambda=\sum_{k=1}^{K}\frac{P^{(n)}(w\mid\phi_k)}{P^{(n+1)}(w)} \qquad \text{Eq 40}$$

$$P^{(n+1)}(w)=\frac{1}{K}\sum_{k}P^{(n)}(w\mid\phi_k) \qquad \text{Eq 41}$$

The results of fitting the von Mises mixture model to phase differences between Venus corresponding pairs at different scales are shown in Figure 17. In this case, J is taken to be five, i.e. total number of mixed von Mises distribution components is five. The five different components for each scale are given at the leftmost column of the figure (Figure 17 a,c,e). As can be seen on the plots, most components are exactly the same, thus J=5 is more than enough. On the rightmost column, the final mixture models are shown on top of the phase difference histograms. Here, top row (Figure 17 a,b) is for scale one, i.e. when filter of width six pixels is used, middle row (Figure 17 c,d) is for scale two, i.e. when filter of width 12 pixels is used and the last row (Figure 17 e,f) is for scale three, i.e. when filter of width 18 pixels is used.

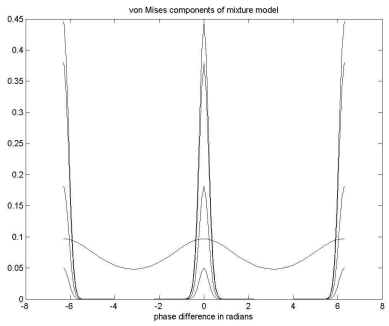

(a)

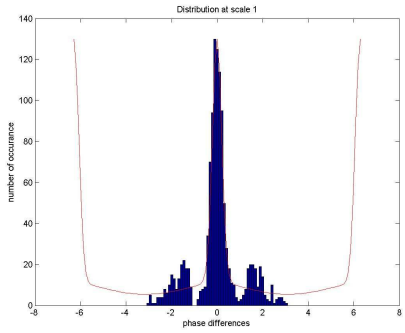

(b)

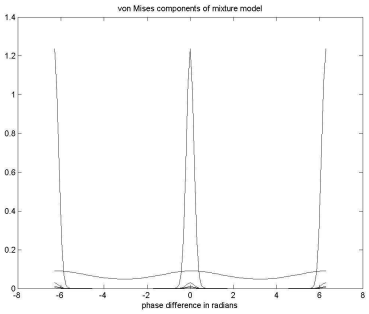

(c)

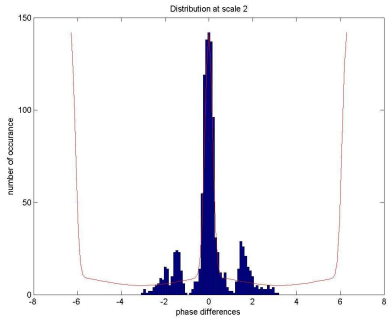

(d)

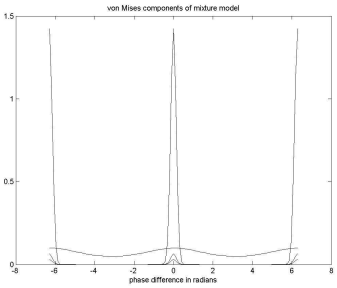

(e)

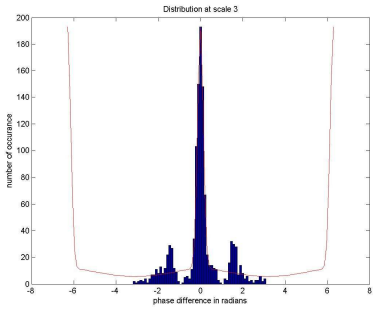

(f)

Figure 17 Mixture of von Mises models for the correct pair phase differences. a, c, e. Components of the mixture model for scale 1, 2 and 3 respectively, b, d, f. Mixture model and histogram of phase differences for scale 1, 2 and 3 respectively.

3.7.2 Probability of Being a Pair

With the parameters of the mixture model to hand, we can estimate correspondence probabilities from the phase differences. The correspondence probabilities are taken to be a posteriori probability of the mixture with the smallest mean at convergence of the EM algorithm. Suppose that Eq 41 is the a posteriori correspondence probability for scale *n* where *j* is the index for candidate corresponding feature points for feature point *i*. The overall correspondence probability is the product of correspondence probabilities computed at the different scales as in Eq 42 assuming that they are independent. The correspondences are taken so as to maximize *P(i=j)* as in Eq 43. Applying the correspondences located in this way the computed disparities for Venus stereo pair are very similar to those found using the method described in Section 3.5. Both results are shown in Figure 18.

$$P^n(\phi_{ij}) = p^n(\phi_{ij}) / \sum_j p^n(\phi_{ij}) \qquad \text{Eq 42}$$

$$P(i = j) = \prod_n P^n(\phi_{ij}) \qquad \text{Eq 43}$$

$$\hat{j} = \arg\max_j P(i = j) \qquad \text{Eq 44}$$

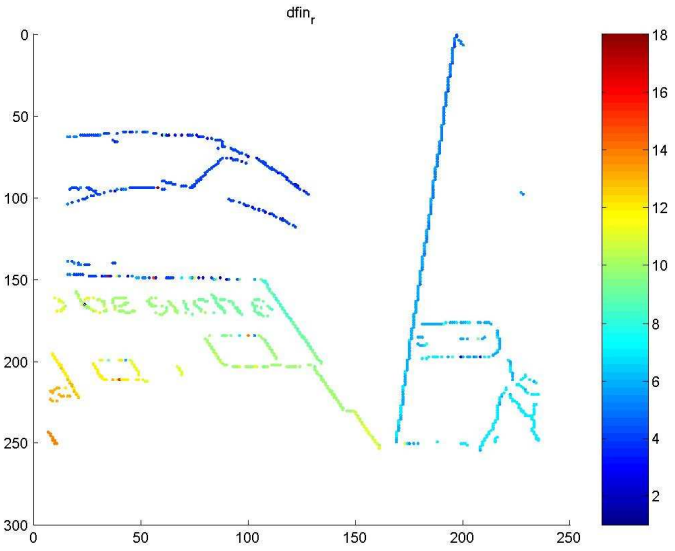

(a)

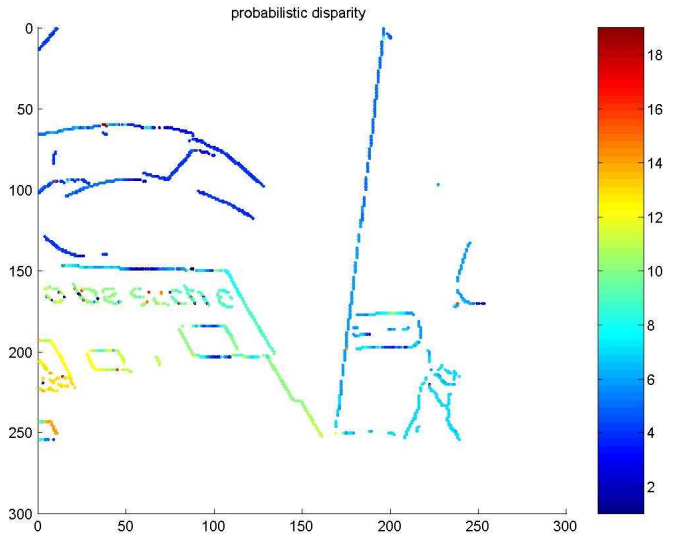

(b)

Figure 18 Results for Venus stereo pair. a. Disparity found by the method in Section 3.5, b. Disparity found by the probabilistic model described in Section 3.6.

3.7.3 Validation of the Probabilistic Model

The same model is applied to Blocks, Sawtooth and Tsukuba stereo pairs and the results are given in Figures 19-21 respectively. The top image in each figure shows the disparity obtained by the method in Section 3.5. The bottom image in each figure shows the disparity estimated by the probabilistic method.

The important thing here is that the probabilistic model obtained from Venus stereo pair is used in order to obtain disparity for Blocks, Sawtooth and Tsukuba image pairs as well and the results are still satisfactory.

Also in Table 3 success rate of the probabilistic model is listed for different stereo pairs. Number of features extracted, number of pairs matched, number of wrong matches and success rate are given in successive columns from left to right for each stereo pair. In this case success rate is also calculated as the percentage of number of wrong matches over total number of matched pairs and found to be better than the numbers in the last column of Table 1 although the number of matched pairs is more in this case. Thus, by this model we obtain disparity values for more number of pairs with higher accuracy.

Table 3 Success rate of the probabilistic model for different image pairs.

Image pair	Number of feature points extracted	Number of pairs matched	Number of mismatches	Success rate (%) over number of matched pairs
Blocks 2	3847	1505	206	86
Venus	1884	1310	85	94
Sawtooth	4288	3079	111	96
Tsukuba	4088	2350	398	83

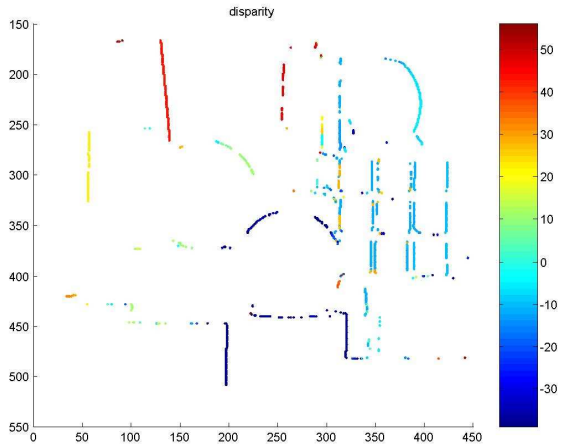

(a)

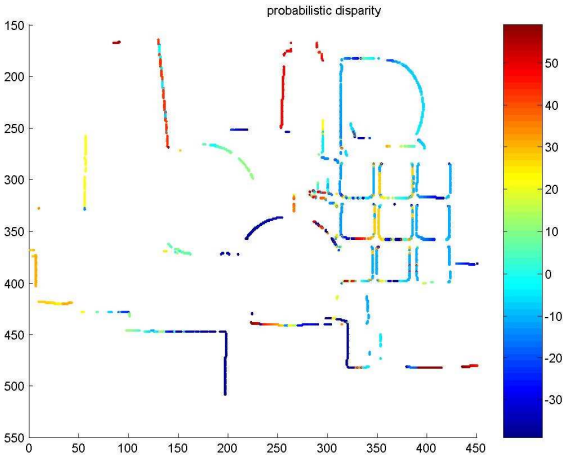

(b)

Figure 19 Results for Block stereo pair. a. Disparity found by the method in Section 3.5, b. Disparity found by the probabilistic model described in Section 3.6.

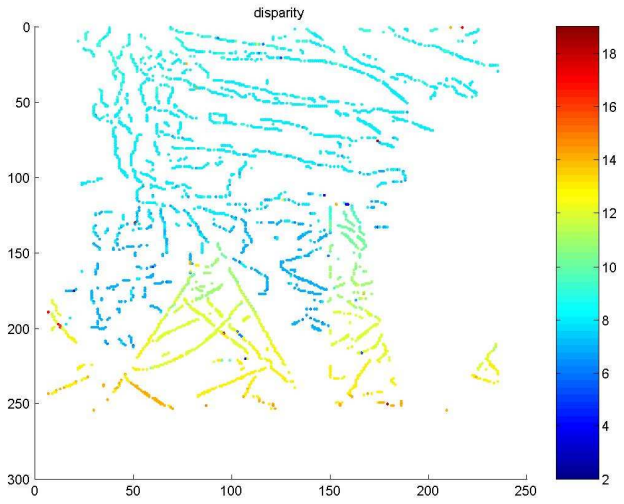

(a)

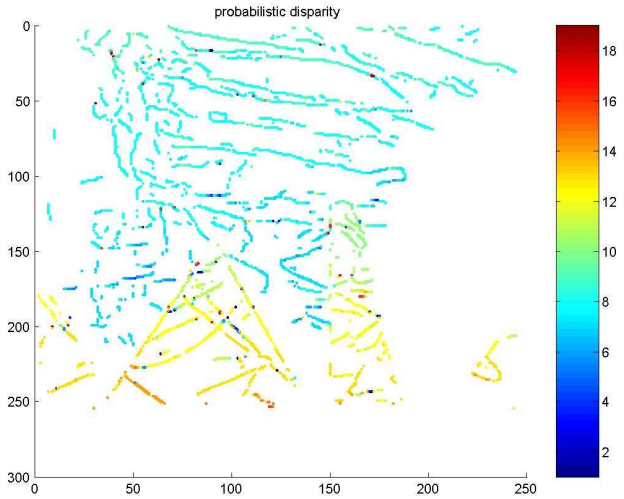

(b)

Figure 20 Results for Sawtooth stereo pair. a. Disparity found by the method in Section 3.5, b. Disparity found by the probabilistic model described in Section 3.6.

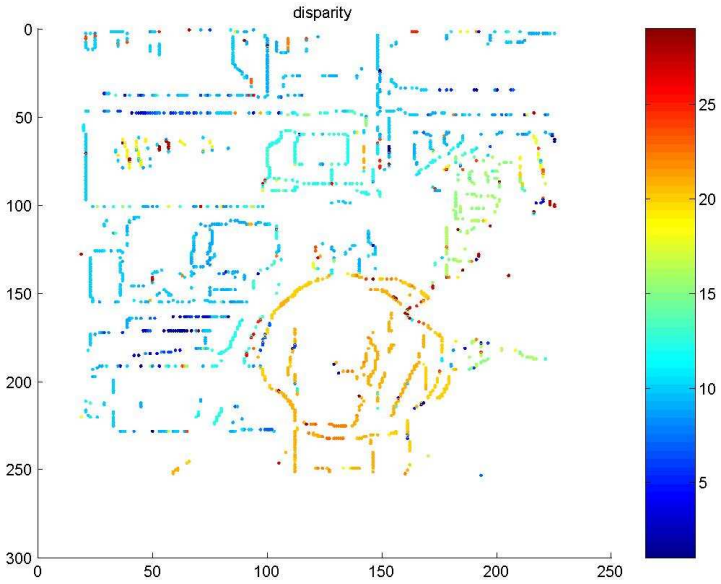

(a)

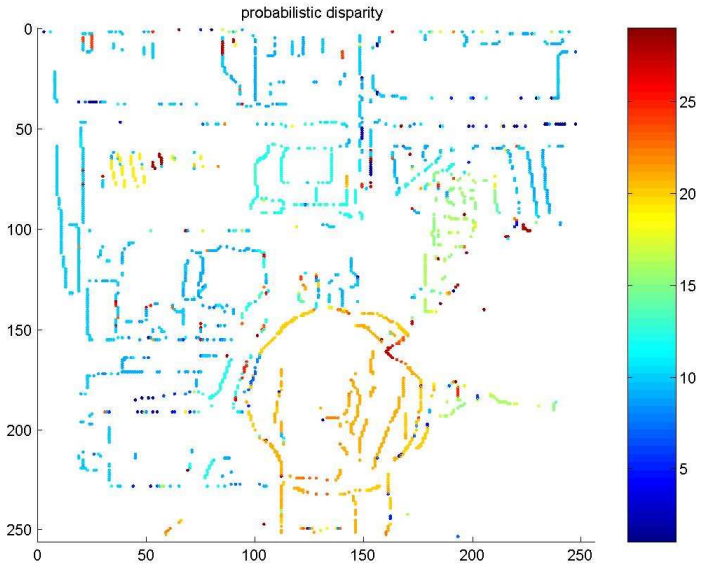

(b)

Figure 21 Results for Tsukuba stereo pair. a. Disparity found by the method in Section 3.5, b. Disparity found by the probabilistic model described in Section 3.6.

3.8 Summary and Conclusion

We have presented a stereo correspondence method which is motivated by biological information. We have modeled hyper column structure of the human visual cortex using steerable filters. Thus, instead of calculating disparities using oriented filters and pooling the results over different orientations, a single orientation for each feature is obtained prior to disparity computation. The steerable filter estimate of stimulus orientation found using this method is very accurate given the small number of filters used.

By using multi-scale filtering highly informative feature points are extracted even they are at different scales. The use of multiple scales is also biologically plausible. The reason for this is that disparity encoding binocular cells are sensitive to different spatial wavelengths. Although feature points extracted from image pairs are sparse, since they are the points of high contrast edges that define the bounding contours of objects, they still prove to be informative.

Correspondences between feature points are located using multi-scale phase information. This idea is also biologically grounded. The reason for this is that simple binocular cells occur in pairs that are in quadrature phase. Also, phase is sensitive to spatial differences, and hence it provides fine image detail which is helpful in discriminating neighboring image regions. Phase is also robust to small scale differences. Unfortunately, there are image locations where phase is singular and can not be reliably used. Such points are the locations where local frequencies at these points are very different from the filter tuning. In this study, by performing phase comparisons at multiple scales and by using magnitude confidence information we overcome these difficulties. The confidence weighting is used to augment phase information with information concerning the magnitude of the steerable filtered image to improve the correspondence method.

Two routes to locating feature-point correspondences are explored. Using the position shift model, rough disparity values are obtained and a large range of

disparities can be calculated, but to a limited accuracy. Using the phase shift model, fine tuning is performed without encountering the quarter cycle limit. This tuning scheme also allows a continuum of disparity estimates to be obtained. Success rate for correct matches over total number of matches is quite high when compared to other studies in which similar type of stereo image pairs are considered. The smallest success rate is obtained for Blocks 2 stereo pair because nearly half of the total number of edges has orientation parallel to the epipolar line and due to the lack of texture, phase contents are very similar for neighboring edges. The next better success rate is for Tsukuba stereo pair. Tsukuba images are known to be a hard image pair for stereo algorithms because they have very complicated depth discontinuities and repeated patterns. The best success rate is obtained for Venus and Sawtooth stereo pairs. In these pairs both textured and textureless regions exist. Also slanted surfaces are present. Thus, they are good examples for matching algorithms.

The complexity of our algorithm is calculated as $O(N^2SRn^2)$ where n is assumed to be the width of the widest filter, S is the total number of scales used and N is the image size where image is though to be square in size. The feature extraction step of our algorithm takes time where as matching and extraction of depth filed is real time. Although highly informative edges are selected as features by using multi-scale strategy, it is time consuming to filter the image pair with filters of various widths. However, with the recent development in hardware and software and with some parallel processing we are hoping to obtain our features in real time in the very near future.

There are of course some problems occur because of using phase in matching since this algorithm gives results for textured regions and edges only. For texture-less regions since there are no edges and features, no disparity value can be found. Thus some post processing such as surface fitting is needed in order to obtain dense disparity values.

There are some taxonomy papers for feature based matching however they are dated very late. One of the recent matching algorithms is given by [93] where feature matching is done for the purpose of camera calibration. Their feature points are corners and proximity and similarity of feature point intensity neighborhood are used for matching. Then RANSAC is used for computing homography. Finally matching is guided by the estimated homography. In their study, the average success rate over different image pairs is %50. The most recent taxonomy study for feature matching is performed by Vincent and Laganiere [95]. They followed the same steps as [93]. But they used variance normalized correlation between feature points for matching. In their study Tsukuba image pair is also used in order to show the results and they reach %67.8 success rate. Than they do left to right and right to left symmetry check and increase their success rate to %71.7 with the number of good matches being 195. When we apply our matching algorithm to the same Tsukuba image pair, although the number of feature points are high in our case, we reach a success rate of %83.

In this part of the thesis, a probabilistic algorithm for correspondence matching is also proposed. Mixture of von Mises distributions are used to model probabilistic matching algorithm using phase differences obtained for a stereo image pair and the model is verified on other stereo pairs. The model provides not only better results especially for Block 2 stereo pair but also flexibility in search region in matching. The important thing here is that although modeling is done by Venus stereo pair data only, it works fine for many other images. Another important thing is that von Mises being a circular distribution has been used in EM algorithm for the first time.

CHAPTER 4

APPLICATION OF OUR ACTIVE STEREO VISION ALGORITHM ON A VIRTUAL ROBOT FOR COGNITIVE MAP FORMATION AND OBJECT RECOGNITION IN A VIRTUAL ENVIRONMENT

4.1 Introduction

In the previous chapter, we explained our disparity algorithm which is based on human vision. In this chapter we will apply it on a virtual robot for the purpose of environmental map construction. Our disparity algorithm is a sparse algorithm and is appropriate for such an application.

The reason why we select such an application is that we want to use our method in a navigation activity which is achieved by humans. Humans can manage a high level of navigation which is called survey navigation by constructing an environmental map in the hippocampus region of the brain. The task of generating robot motion in the pursuit of building a map is commonly referred to as robotic exploration. While optimal robot motion is relatively well-understood in fully modeled environments, exploring robots have to cope with partial and incomplete models. Hence, any viable exploration strategy has to be able to accommodate contingencies and surprises that might arise during map acquisition. For this reason, exploration is a challenging planning problem, which is often solved sub-optimally via simple heuristics. In this study, we also suggest a heuristic for environmental map construction strategy using our disparity algorithm only.

Humans can perform many different activities simultaneously. While they are walking, they can recognize objects that they observe around their pathways. Thus a vision model should be such that it could be used for as many purposes as possible such as obstacle avoidance, map construction and object recognition . The best way of doing this is to construct a vision model which is as close to the human visual system as possible. Our model is also good for other visual activities such as obstacle avoidance and object recognition as well as environmental map construction. In this chapter we also give a recognition algorithm for simple shaped objects.

We apply our algorithm in a 3D virtual environment. There is a virtual agent in this environment and this agent has stereo cameras which are modeled based on human eye properties. The cameras are positioned at a height above the ground level with six cm distance between each other just as the eyes of humans. The cameras are controlled in the way human eyes can be. Given a target location, both eyes look at the same target point with similar parameters such as focal length. There are also 3D objects from the set {apple tree, pine tree, cottage} with different shapes, sizes, textures and colors in this virtual world. These 3D objects are made up of two basic shapes from the set {sphere, ellipsoid, cylinder, cone}. For example, a big radius cone on top of a big radius cylinder is a cottage, whereas a small radius cone on top of a small radius cylinder is a pine tree. Also, a sphere on top of a cylinder is for an apple tree. The objects can be placed anywhere on the ground in the virtual world and the agent can move anywhere around them.

We explained our physiological model of disparity extraction in the previous chapter. For each stereo image pair that the agent obtains from the virtual environment, disparity is extracted and depth for the current view is calculated. In doing this we assume that the camera parameters are known by the agent just like the eye parameters such as focal length are known by the humans. When looking at a distant location the eye muscles activate such that the view is as clear as possible and this is coordinated between the visual cortex and eye muscles which is

obviously showing that human brain is aware of the eye parameters for depth calculation.

The map is constructed using the location information extracted from the current view in a way that each grid value is increased by one if something is observed at the location covered by that grid. This means that the belief of that grid being occupied is as large as the value of that grid. Also, color information is kept for each grid. In this study we used world centered, grid based cognitive map structure due to its applicability, differentiability, simplicity and fine grained structure. World-centric maps are represented in a global coordinate space. Since disambiguation of similar but different places is hard and extrapolation from individual measurements to measurements nearby is very difficult for robot-centric approaches, dominant approaches to date generate world-centric maps. Occupancy grid map is a metric map that represents the environment by fine grained grids and models the occupied and free space of the environment whereas topological maps only give the relative position of the things in the environment. Since metric maps are finer grained than topological ones, places that look alike can be disambiguated more easily. Although this high resolution comes at a computational price, it helps to solve various hard problems. In this study, unlike the common 2D grid-based maps, we construct 3D map of the environment.

While the agent is exploring the environment, new objects seen around are investigated in detail. Using the location and color information, the shape of the object parts are estimated and the whole object is classified to be either one from the set: {apple tree, pine tree, cottage}.

Further details for virtual world construction software, map construction algorithm and object recognition are given in the following sections.

4.2 Design and Implementation Details of the Simulation Software

The simulation software is developed using C++ programming language and OpenGL graphics library on the Microsoft (MS) Windows operating system (OS) [94]. As the user interface of the software is depicted in Figure 22, it is composed of four panes showing the scene from different view points. The two panes above are views from the left camera (eye) and right camera, respectively. The bottom panes render the scene from the top viewpoint, and front viewpoint. Below of the bottom panes, there are tab based (so called) dialog boxes which allow entering/adjustment of the parameters used throughout algorithm implementations.

A multi-purpose user interface for displaying the calculated feature point information is shown in Figure 23. You can either see only the rendered stereo images or both stereo images and extracted feature points simultaneously by selecting “Show Feature Point” option button shown under each image. By selecting a channel from the pull-down menu called “Channel” various kinds of information can be seen for each feature point on the screen. For example, in this specific study, Channel 0 to Channel 2 are used to keep world coordinates of the feature points, i.e. x,y,z locations respectively. Channel 3 is used for disparity and Channel 4 is for agent centered depth. Any information can be arranged to be printed on the screen with minor changes in the software. Moreover, by clicking on a feature point by mouse, all the information about that feature point, i.e. information of all channels, is seen in the dialog box called “Point Info”. In Figure 23, the image shown on the left side is the left camera view and the black dots on the image show feature point locations for this current view. The image on the right side is the right camera view and Channel 3 is selected to be shown on the feature points thus the disparity values for the right feature points are shown in colors.

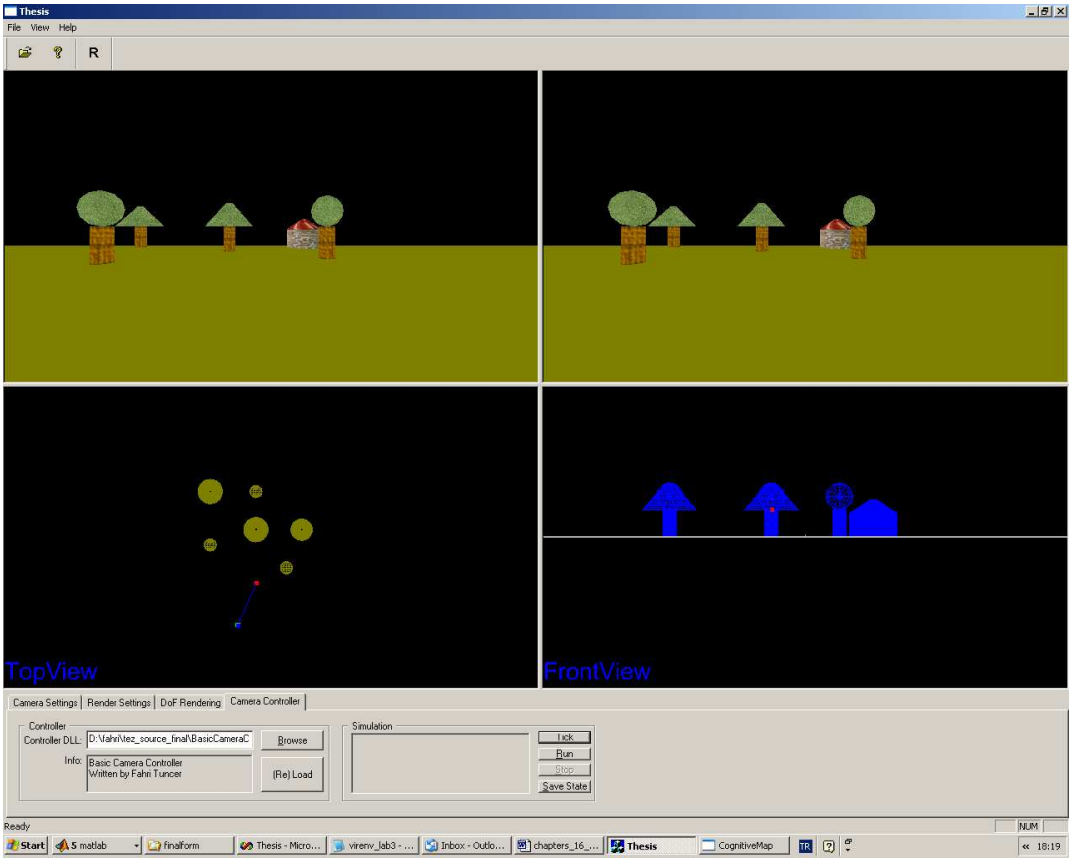

Figure 22 A screen shot from the virtual environment. A farm cottage and different type of trees are seen. In the upper left and right panes left and right eye views are shown respectively. In the lower left and right panes top and front views are shown respectively. Below of the bottom panes, there are tab based dialog boxes.

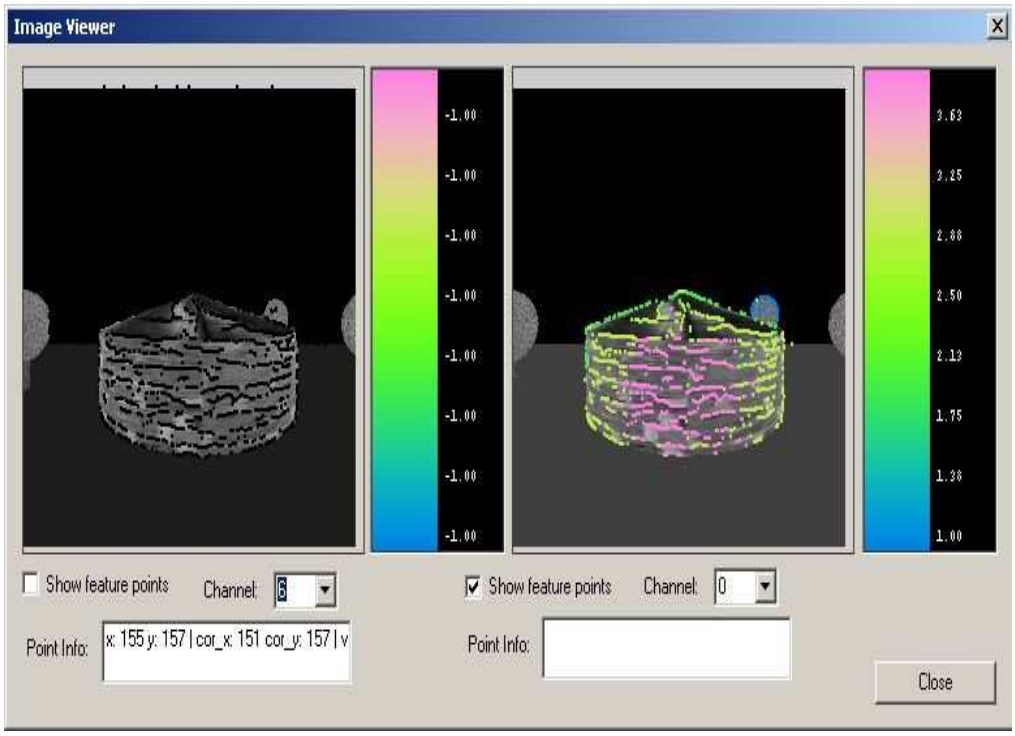

Figure 23 Interface for displaying feature point information. Locations of feature points for the cottage are shown on the left camera view as black dots and disparities found are shown on the right camera view in colors.

Basically, the software should fulfill the following requirements in order to be used in our study:

1. It should allow specifying and rendering arbitrary geometric shapes and these shapes should be placed somewhere in the virtual environment.

2. We should locate the agent at any point on the ground of our virtual world.

3. Images rendered for the current snapshots viewed by the camera(s) (left and right) should be exported to a specified image file for future processing.

4. We should modify the camera parameters whenever we would like. Those modifications should be observed at interactive frame.

5. The software should support some kind of plug-in mechanism to be loaded (and linked) dynamically into the application at run-time. This plug-in should access internal structure of the scene data and image(s) rendered, so that this plug-in would control the navigation in the scene by locating the camera. The method or methods used by this plug-in(s) to navigate through the scene is up to the internals and goals of the plug-in. In this study, the navigation algorithm for the purpose of environmental map formation and object recognition will be the camera controller plug-in.

Some assumptions made in this study are as follows:

1. Objects in the environment are made up of two parts and these parts have one of the following basic shapes: {sphere, ellipsoid, cylinder, cone}. The shapes can be of any size, color and texture. The final objects are either one from the set {apple tree, pine tree, cottage}.

2. The objects constructed from these basic shapes can be located anywhere in the world.

3. The objects are clearly separable.

4. The agent is aware of its initial position in the world and initial orientation with respect to global north.

5. The agent is aware of its internal camera parameters.

6. The agent is aware of its external camera parameters such as position and gaze direction.

7. The cameras can see up to a predefined distance.

8. There is no error in agent movement, i.e. agent goes to its target with success.

According to these requirements and assumptions the software is designed and implemented as follows:

1. Specifying the geometric shapes is done via loading the shape and texture data from a disk file. The format of the geometry file is given in Appendix B. The geometric shapes are easily handled using object oriented techniques. Some primitive shapes such as ellipsoid, cylinder and cone are used in order to form other complex shapes such as trees, cottages, etc. The shapes can have different sizes. For example, a pine tree is constructed from a cone on top of a cylinder, whereas a cottage is constructed from a cone on top of a large radius cylinder.

2. The requirement of locating the camera anywhere in 3D space is fulfilled in three ways. First, at the bottom panes (top view and front view), the user can change the position of the camera and its target by dragging the camera and target symbols within the views, as shown in Figure 24. Second, the user can enter the camera parameters numerically in dialog box named "Camera Settings" at the bottom tabbed control. Third, the camera parameters can be controlled automatically via the plug-in.

3. The rendered images on the left and right camera views can be exported by entering the menu (pop-up menu) by clicking the right-mouse button within the views, and selecting ‘Export Frame’. Also rendering could be done via the plug-in automatically.

4. The plug-in mechanism to load a camera controller is done by using dynamic-link libraries (DLL). A sample camera controller source is listed in Appendix C. The camera controller source used in this study will be explained in the following section. The camera controller DLL controls the stereo cameras (i.e. the agent) through the virtual world in an intelligent way in order to extract the environmental cognitive map and recognize the objects.

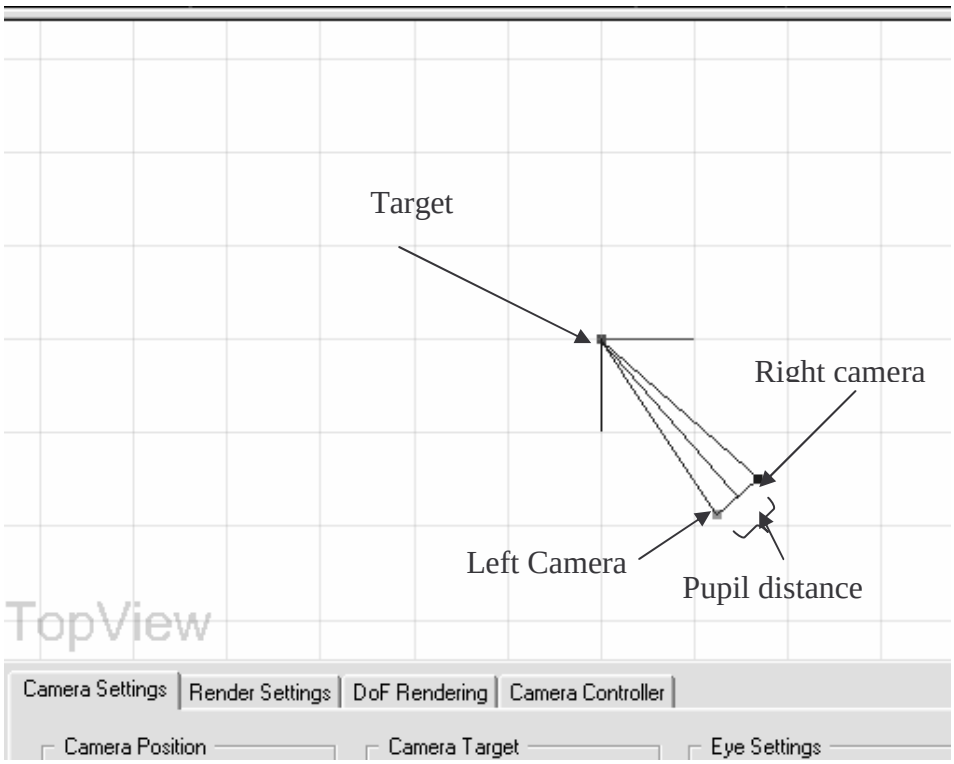

Figure 24 Top-view with camera and target controls

4.3 Camera Controller

The camera controller used in this study controls the camera internal parameters, positions and orientations, renders the stereo images, processes these images and extracts depth information in order to construct a world-centered, grid based cognitive map and recognize the objects in the view.

The following basic activities are performed by our camera controller dll:

1. Gaze direction, focal length, field of view, base (pupil) distance between the cameras are the main camera parameters which could be modified whenever desired. This is done either by entering the camera parameters numerically in dialog box named "Camera Settings" at the bottom tabbed control or by automatically setting in the plug-in.

2. Stereo images are rendered.

3. Depth information is extracted from the stereo image pair.

4. Cognitive map is updated for the current view using depth and color information.

5. Next position of the agent is decided according to the purposes. If the agent needs to explore the environment more, first of all it turns around itself to see if there is something new close to it. If the agent sees a new object and wants to be sure if it is a real thing or noise, the next target is selected so that the agent gets close to the object leaving some clearance between the object and itself. If the agent is sure that it is a new object, going around it in order to recognize it is the next movement and this is done in a controlled manner keeping a clearance between the object and the agent. If the agent doesn't see anything new around then it goes to the most unexplored region.

6. Object recognition is achieved after the agent fulfills a complete turn around a new object.

4.4 Active Vision and Cognitive Map Construction

In this study, world centered, grid based 3D map of the environment is extracted and each grid codes a 1x1x1 unit cube of world unit. The cognitive map is constructed from the depth information obtained via the disparity algorithm.

Feature extraction for the current view, estimation of the disparity and calculation of the agent centered depth information are obtained as explained in Chapter 3. The maximum allowed disparity is set to a value at the beginning and is kept the same all through the processes. The depth information also provides a sort of obstacle location information in the field of view. This agent centered location information is converted to world centered location information by Eq 44 where R is the rotation and translation matrix which converts the camera coordinates $z_C = (x_c, y_c, z_c)$ to world coordinates $z_W = (x_w, y_w, z_w)$.

$$z_W = \mathbf{R} z_C \qquad \text{Eq 45}$$

The state space structure of the system is as given in Figure 25. Also in Figure 26 the flow chart is given. Based on this structure, the following recursive active vision and exploration strategy is followed for the purpose of cognitive map construction:

1. Initially, cognitive map grid values are set to zero, agent is located and oriented in the world and the cameras take the first stereo view, i.e. images are rendered.

2. The disparity and depth are calculated as in Chapter 3 and the world coordinates of the feature points are calculated as in Eq 44. The resulting values for feature points could be observed by the interface as in Figure 23 if desired.

3. For the current view, map is updated. World centric location information for each feature point is used to fill the cognitive map such that if a feature point belongs to a grid on the map, that grid's value is increased by 1. So each grid will keep a number which shows something like the belief of that grid being full. The belief of being full is as high as the number.

4. If something new is observed in the view, the agent is moved in front of the nearest object to take a sharper view and steps 2 and 3 are repeated. If it is really an object not a noise, then the agent starts to turn around that object by looking at the object all the time and keeping a distance between the object in the view and itself. For each move while turning around the object, steps 2 and 3 are repeated. If turning around the object is fulfilled with success then process continues from step 6.

5. If nothing new is observed, the agent makes a 90˚ counter-clock wise turn around itself and repeats 2 and 3. If a new object is observed then and steps starting from 2 are repeated. The agent continues to make 90˚ counter-clock wise turns around itself until it makes a full turn or a new object is seen. If nothing is observed until the agent makes a full turn around itself then the agent moves to a different location. In this move, the already constructed cognitive map is checked and the closest unexplored direction is selected and the agent starts to move in that direction

until a new object is seen or until the borders of the world are reached. If a new object is seen during this time, steps starting from 2 are repeated. If nothing is observed then the agent starts to turn around itself and step 5 is repeated.

6. If turning around an object is fulfilled with success then object recognition is performed. The object recognition algorithm will be explained in the next subsection. While turning around the object, if some other objects are seen somewhere then the nearest one is selected to be the next target after object recognition step is completed. The agent is moved to that target and stereo images are rendered and steps starting from 2 are repeated

7. During all these movements the 3D cognitive map is updated gradually. In the end the 3D cognitive map of the environment is obtained. The grid points which have high numbers, i.e. high belief of being full, are selected to be full.

The 3D cognitive map for the environment given in Figure 22 is shown in Figure 27.

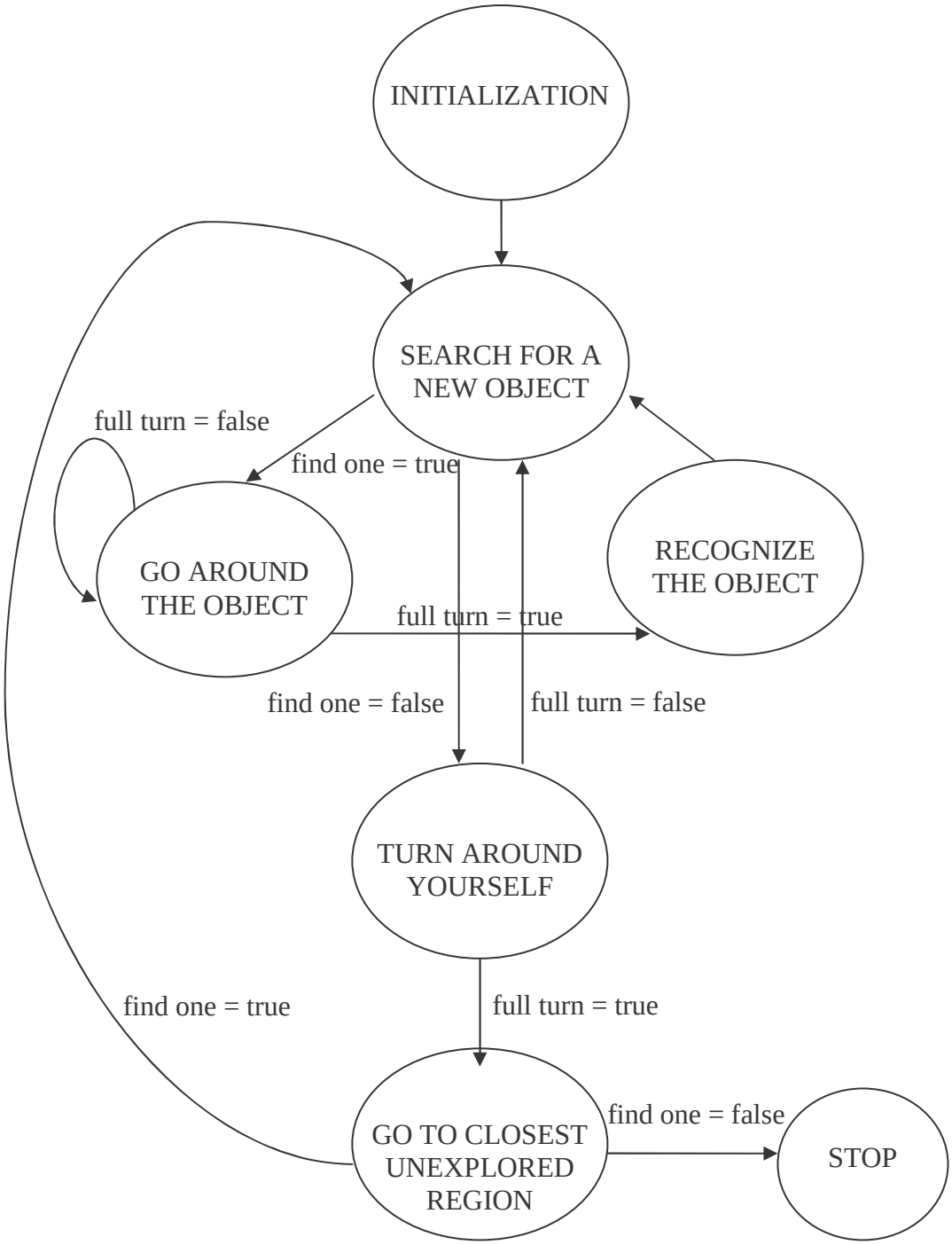

Figure 25 States of camera controller DLL.

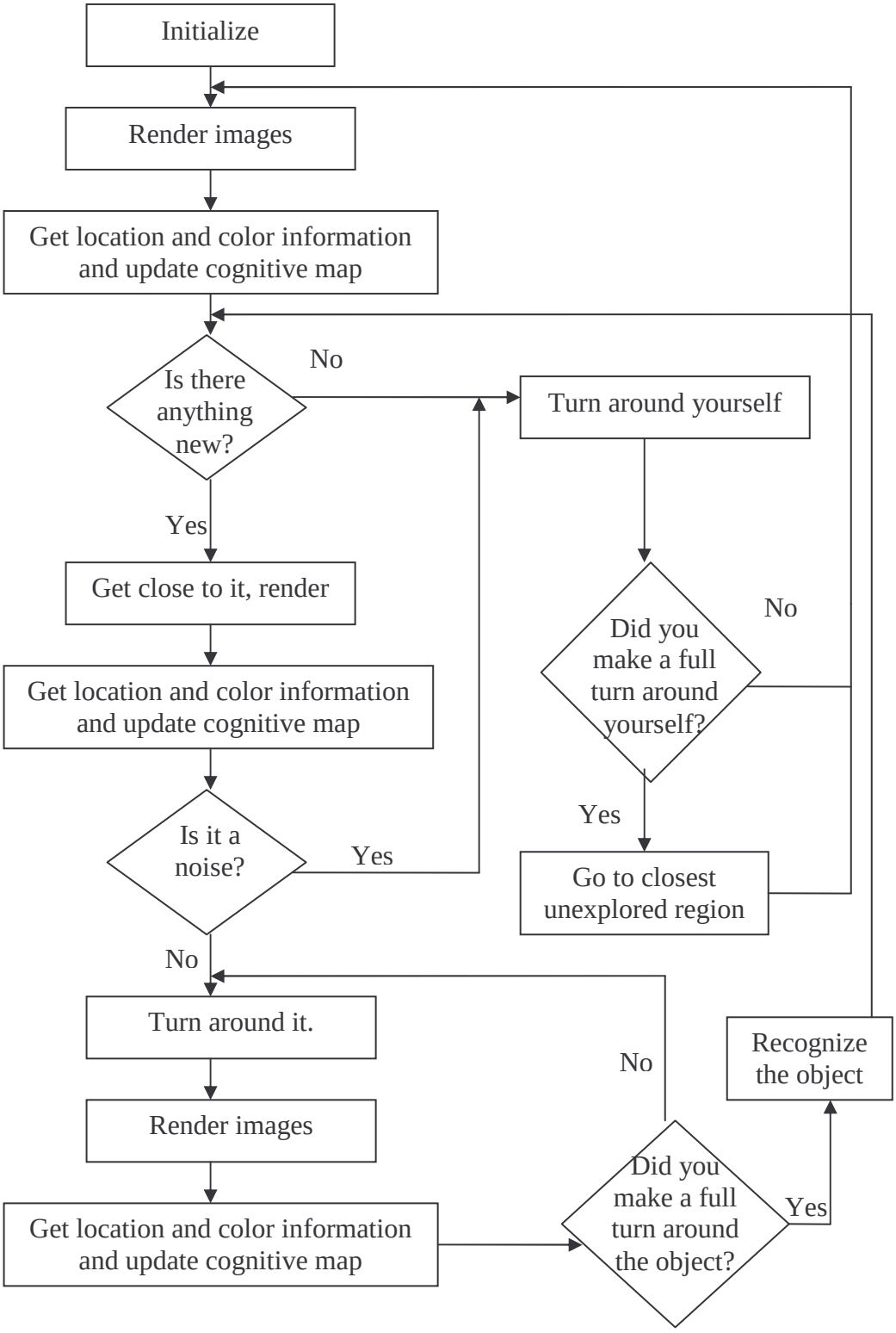

Figure 26 Flowchart of the map construction system.

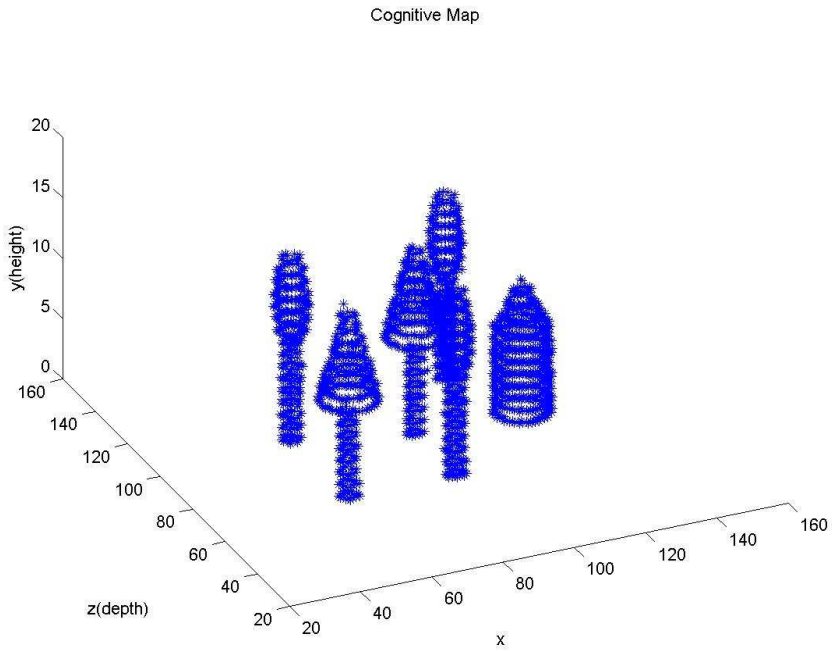

Figure 27 3D cognitive map. x- and z- axis are the width and depth of the environment respectively and y-axis is for height above the ground. Only the grids for which the belief of being occupied are high are shown here. Others are given zero values i.e. not occupied.

4.5 Object Recognition

While exploring the environment for the purpose of map construction, whenever a new object is seen, the agent gets close to that object and turns around it keeping a clearance between the object and itself and gets the 3D feature point locations of that object. These locations are (x,y,z) triples..

While filling the cognitive map, the RGB color information is also saved for each grid. This is done by following a few steps: First the averages of the RGB values for each feature point are calculated. This is done by averaging the RGB values of the pixels falling into a window centered at a feature point selected on the right image of the stereo pair. Then the averages of the RGB values of the feature points falling on the same grid are calculated. Finally the RGB averages for each

grid are calculated through time. This means that at each update of the cognitive map, the color averages stored at each grid are also updated.

After completing a full turn around the object, the 3D location information in terms of grid locations and RGB color information for each grid are obtained. In order to classify the object being observed, only the grids which have high belief of being occupied are used and the following steps are followed: First, the RGB color information is converted to HSV using the C++ script given in Appendix D. Second, assuming that the top and body parts of the objects have different color content, the 3D object is segmented into two parts. In doing this, the following basic ideas are used: 1. The color content of all the grids belonging to a segment of the object should be similar. 2. The grids containing similar color information should be connected. In this study, only the hue channel is found to be enough for segmentation. The neighboring grid points which have similar Hue values are clustered together. In the top images of Figure 28 and Figure 29, the Hue values for the apple tree and pine tree are given respectively. In the bottom images of the same figures the segmented object parts are seen. For the apple tree segmented parts are a spherical and a cylindrical shape. For the pine tree the segmented parts are a conical and a cylindrical shape. In the third step, the shapes of the segmented parts are estimated by fitting the quadratic surface equation of three parameters. As the last step, the object is recognized from the shapes of its parts.

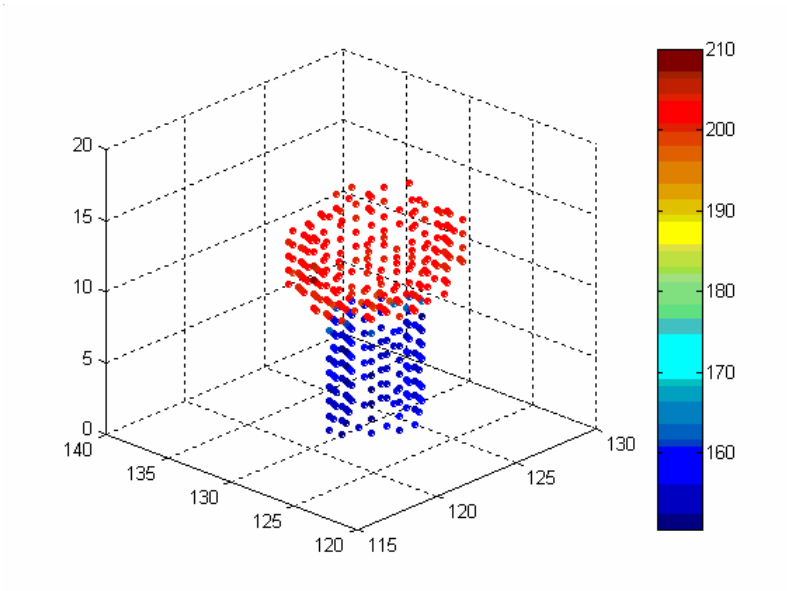

(a)

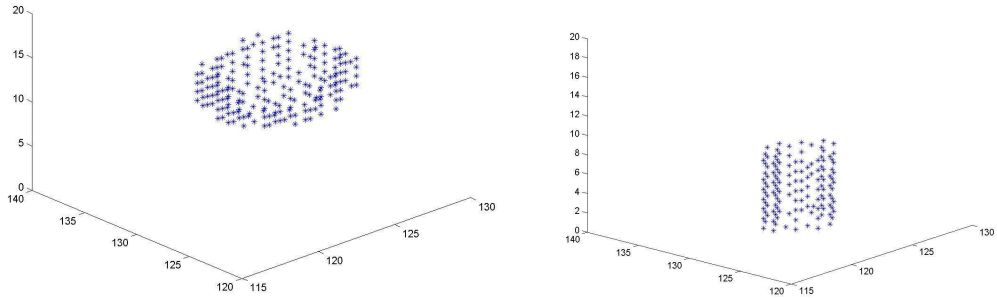

(b) (c)

Figure 28 a. Location and color information stored in each grid for an apple tree in the cognitive map, b. Cognitive map grids for the top of the apple tree, c. Cognitive map grids for the body of the apple tree.

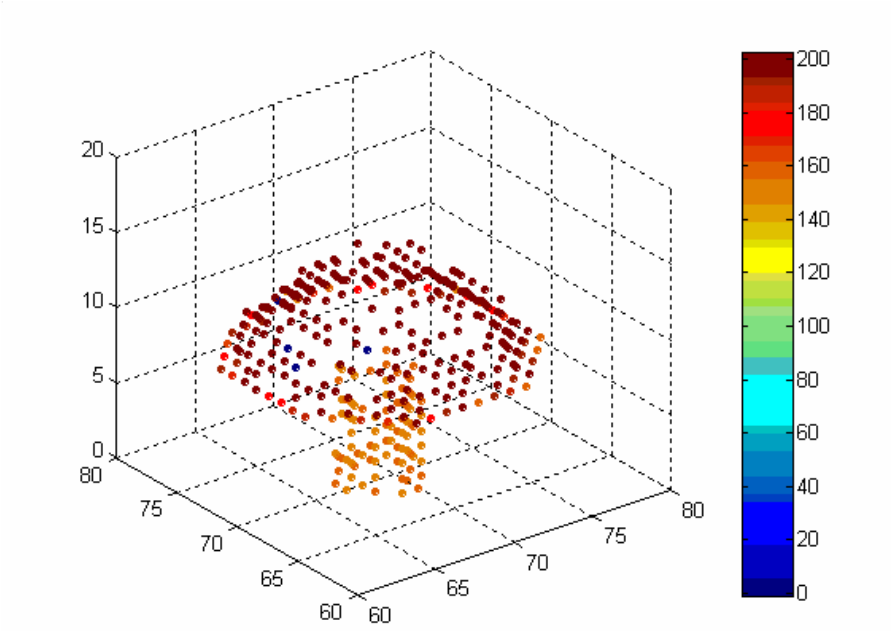

(a)

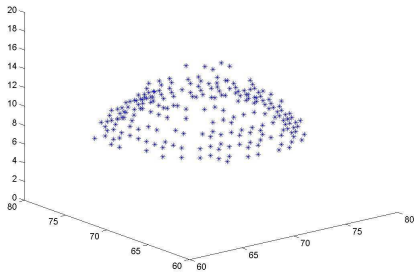

(b)

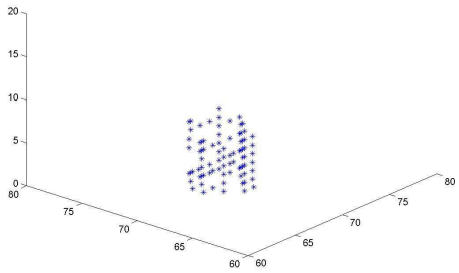

(c)

Figure 29 a. Location and color information stored in each grid for a pine tree in the cognitive map, b. Cognitive map grids for the top of the pine tree, c. Cognitive map grids for the body of the pine tree.

In order to extract the shape information for a part of the object, these steps are followed: First, triples (x,y,z) belonging to the part are used in Eq 45. This equation is called the general quadratic equation in three variables [43, 83]. Then, the parameters {A,B,C,D,E,F,G,H,K,L} are found. In this study, we assume that the

parameter A in Eq 45 is non-zero, since the shapes in our environment is either sphere, cylinder or cone. Reorganizing Eq 45 we obtained Eq 46 and the unknown equation parameters P={B',C',D',E',F',G',H',K',L'} can be solved as in Eq 47 where $\breve{V}$ is the pseudo inverse of V (Eq 48) and X is the vector of x-coordinates (Eq 49). Here N is the total number of (x,y,z) triples. Finally, form these parameters we can comment on the shape [43, 83].

$$Ax^2 + By^2 + Cz^2 + 2Dxy + 2Exz + 2Fyz + 2Gx + 2Hy + 2Kz + L = 0 \qquad \text{Eq 46}$$

$$B'y^2 + C'z^2 + 2D'xy + 2E'xz + 2F'yz + 2G'x + 2H'y + 2K'z + L' = -x^2 \qquad \text{Eq 47}$$

$$P = \begin{bmatrix} B' \\ C' \\ D' \\ E' \\ F' \\ G' \\ H' \\ K' \\ L' \end{bmatrix} = \breve{V} * X \qquad \text{Eq 48}$$

$$V = \begin{bmatrix} y_1^2 & z_1^2 & 2x_1y_1 & 2x_1z_1 & 2y_1z_1 & 2x_1 & 2y_1 & 2z_1 & 1 \\ . & . & . & . & . & . & . & . & . \\ . & . & . & . & . & . & . & . & . \\ . & . & . & . & . & . & . & . & . \\ . & . & . & . & . & . & . & . & . \\ . & . & . & . & . & . & . & . & . \\ . & . & . & . & . & . & . & . & . \\ . & . & . & . & . & . & . & . & . \\ y_N^2 & z_N^2 & 2x_Ny_N & 2x_Nz_N & 2y_Nz_N & 2x_N & 2y_N & 2z_N & 1 \end{bmatrix} \qquad \text{Eq 49}$$

$$X=\begin{bmatrix} x_1^2 \\ . \\ . \\ . \\ . \\ . \\ . \\ . \\ x_N^2 \end{bmatrix} \qquad \text{Eq 50}$$

In order to comment on the shape, first of all an S matrix (Eq 50) and Q vector (Eq 51) are formed from the parameters. This S matrix is a non-zero real symmetric matrix [43, 83] and has real characteristic values, i.e. real eigenvalues $\lambda_1, \lambda_2, \lambda_3$, where at least one of them is different than zero. Since we deal with 3 basic shapes of sphere, cone and cylinder, we can say that all three are different than zero. Thus, there exists an orthogonal matrix R such that Eq 52 holds. Considering the change of coordinates $\bar{\mathbf{x}} = R^T\mathbf{x}$ where $\mathbf{x} = (x, y, z)$, Eq 45 can be rewritten as Eq 53 where $\overline{G}'$, $\overline{H}'$, $\overline{K}'$ are calculated as in Eq 54. Here, u_1, u_2, u_3 are the eigenvectors of S. Knowing that all three of the eigenvalues are non-zero, we can translate $\bar{x}$ system to $\tilde{x}$ system by $\tilde{x} = \bar{x} + \frac{\overline{G}'}{\lambda_1}$, $\tilde{y} = \bar{y} + \frac{\overline{H}'}{\lambda_2}$, $\tilde{z} = \bar{z} + \frac{\overline{K}'}{\lambda_3}$. Then Eq 53 can be rewritten as in Eq 55 where k is calculated as in Eq 56.

$$S = \begin{bmatrix} 1 & D' & E' \\ D' & B' & F' \\ E' & F' & C' \end{bmatrix} \qquad \text{Eq 51}$$

$$Q = \begin{bmatrix} G' \\ H' \\ K' \end{bmatrix} \qquad \text{Eq 52}$$

$$R^T SR = \begin{bmatrix} \lambda_1 & 0 & 0 \\ 0 & \lambda_2 & 0 \\ 0 & 0 & \lambda_3 \end{bmatrix} \quad \text{Eq 53}$$

$$\lambda_1 \bar{x}^2 + \lambda_2 \bar{y}^2 + \lambda_3 \bar{z}^2 + 2\overline{G}'\bar{x} + 2\overline{H}'\bar{y} + 2\overline{K}'\bar{z} + L = 0 \quad \text{Eq 54}$$

$$\overline{G'} = Q^T u_1, \ \overline{H'} = Q^T u_2, \ \ \overline{K'} = Q^T u_3 \quad \text{Eq 55}$$

$$\lambda_1 \tilde{x}^2 + \lambda_2 \tilde{y}^2 + \lambda_3 \tilde{z}^2 = k \quad \text{Eq 56}$$

$$k = \frac{\overline{G'}^2}{\lambda_1} + \frac{\overline{H'}^2}{\lambda_2} + \frac{\overline{K'}^2}{\lambda_3} - L' \quad \text{Eq 57}$$

In order to comment about the shape of the object part, Eq 55 can be transformed into Eq 57 using the relations $a = \sqrt{\frac{k}{\lambda_1}}$, $b = \sqrt{\frac{k}{\lambda_2}}$, $c = \sqrt{\frac{k}{\lambda_3}}$ where all a,b,c are nonzero.

$$\frac{x^2}{a^2} + \frac{y^2}{b^2} + \frac{z^2}{c^2} = 1 \quad \text{Eq 58}$$

If the shape is a sphere (for example the top of the apple tree) then these numbers are equal or very close to each other, i.e. a=b=c, and the average could give us the radius of the sphere. If the shape is a cylinder (for example the body of the trees) then two of these numbers are equal or similar and the other one is very different and bigger than the other two. The similar ones give the radius of the cylinder. If the shape is a cone (for example the roof of the cottage) then one of these numbers is imaginary (i.e. square of the number is less than zero) and the other two are greater than zero.

After finding the shape for both of the object parts, the object is recognized using the following logic:

* If there is a sphere on a small radius cylinder, this is an apple tree.
* If there is a cone on a small radius cylinder, this is a pine tree.
* If there a cone is on a big cylinder, this is a cottage.

After going around the environment and recognizing all the objects seen, we finally have the location information for all the objects and label for each of them. In Figure 30 the 2D occupancy map and estimated labels for the objects are shown. 2D map is calculated by summing the grid values of 3D map in y-axis which gives us the usual 2D environmental map.

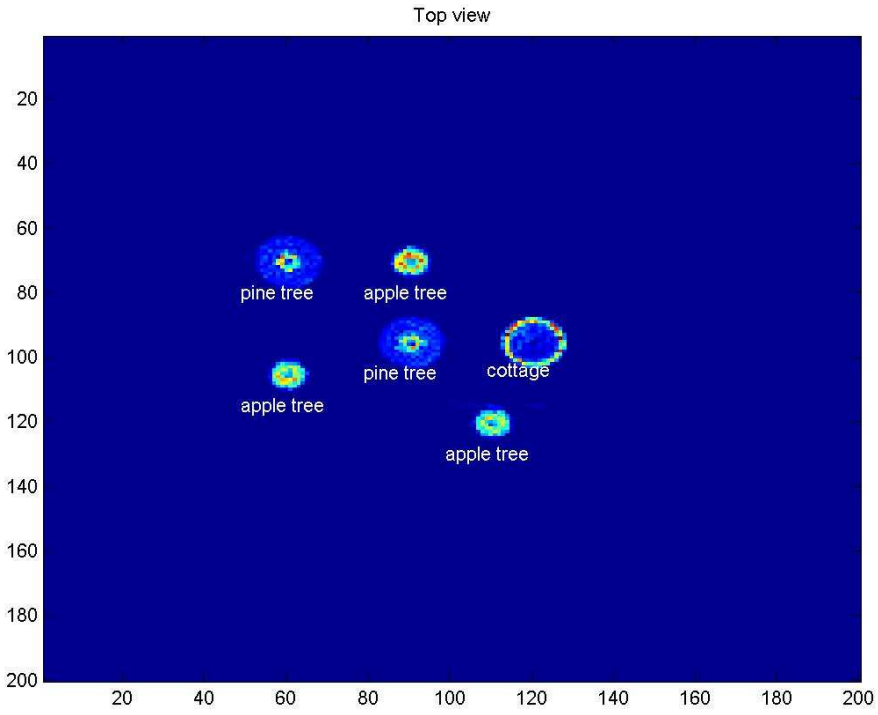

Figure 30 Labeled occupancy.

4.6 Results and Conclusion

Some other virtual environments and the resultant 3D map and 2D occupancy information are given in the following figures. In Figure 31 the environment is constructed such that there is one from each object class and each of them is placed very far away from the others. In Figure 32 the environment consists of three apple trees which have different sizes. In all cases, map construction and object recognition are successfully completed.

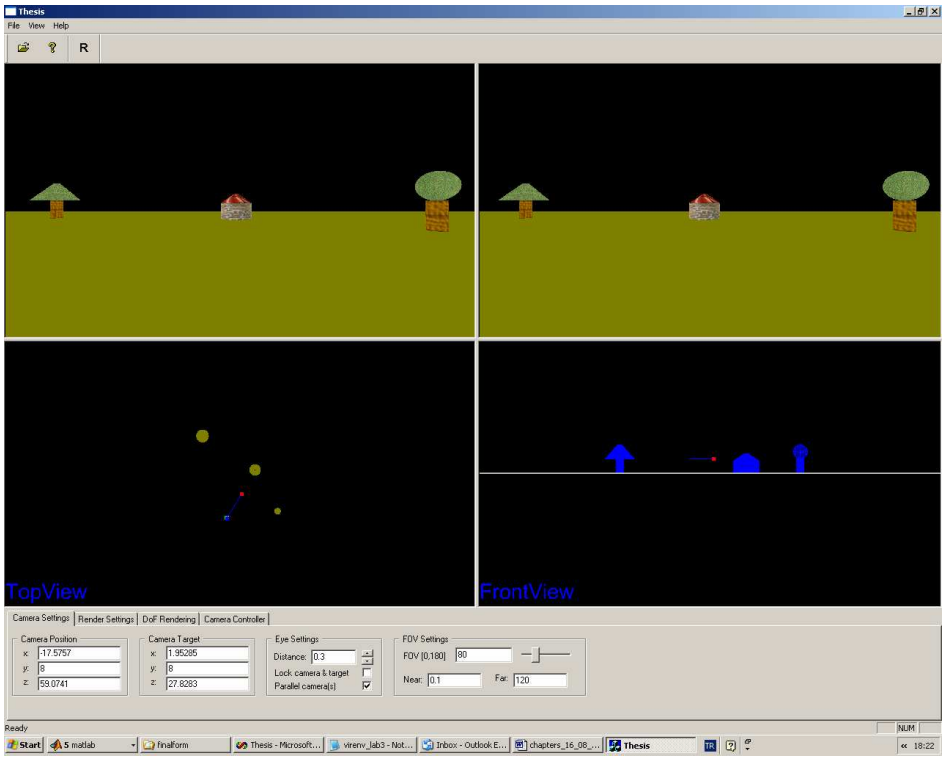

(a)

Figure 31 a. Virtual environment with three different object very far away from each other, b. Computed 3D map, c. Occupancy (top view of 3D map) with labeled objects.

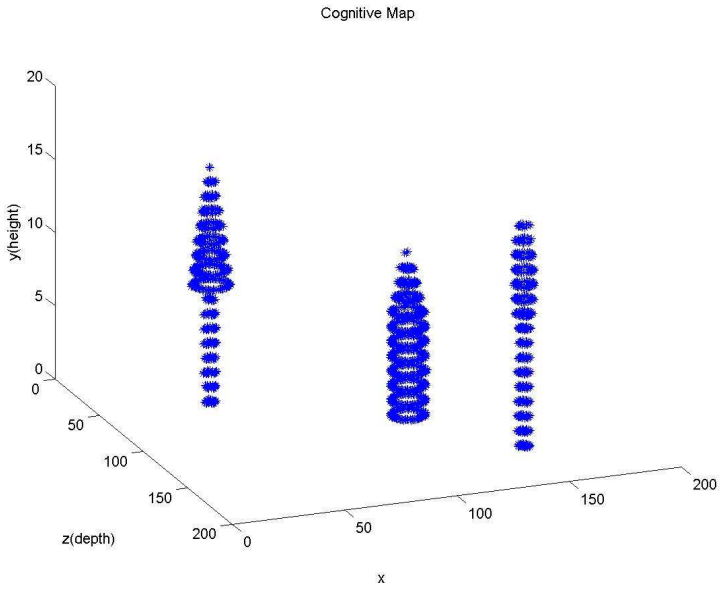

(b)

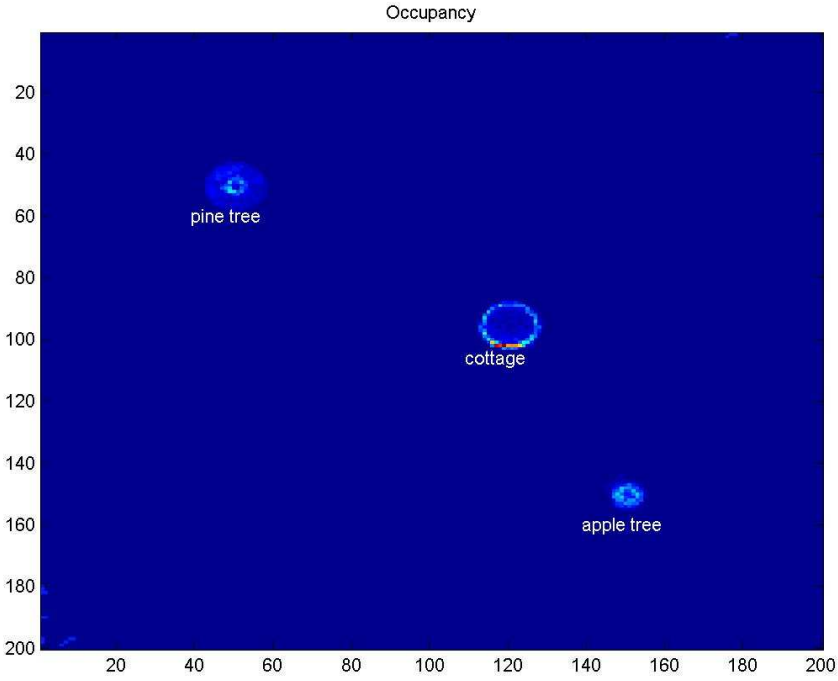

(c)

Figure 31 continued.

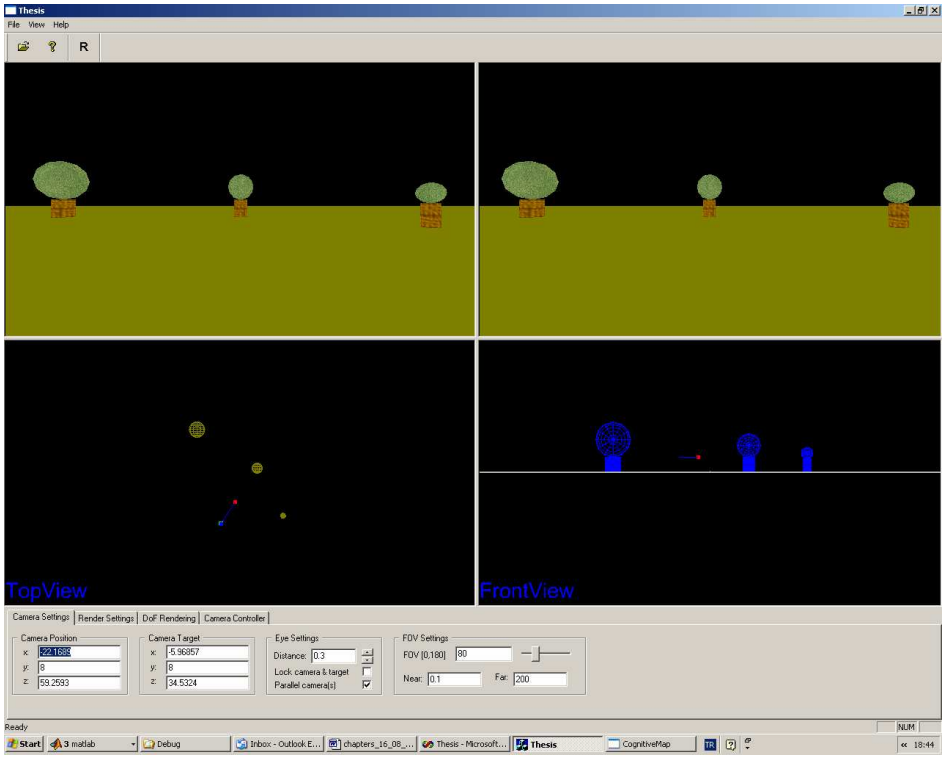

(a)

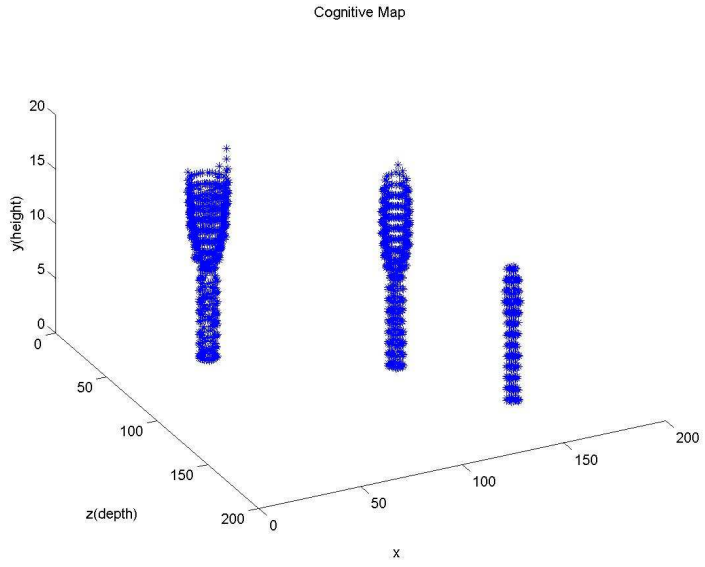

(b)

Figure 32 a. Virtual environment with three objects of the same type, b. Computed 3D map, c. Occupancy (top view of 3D map) with labeled objects.

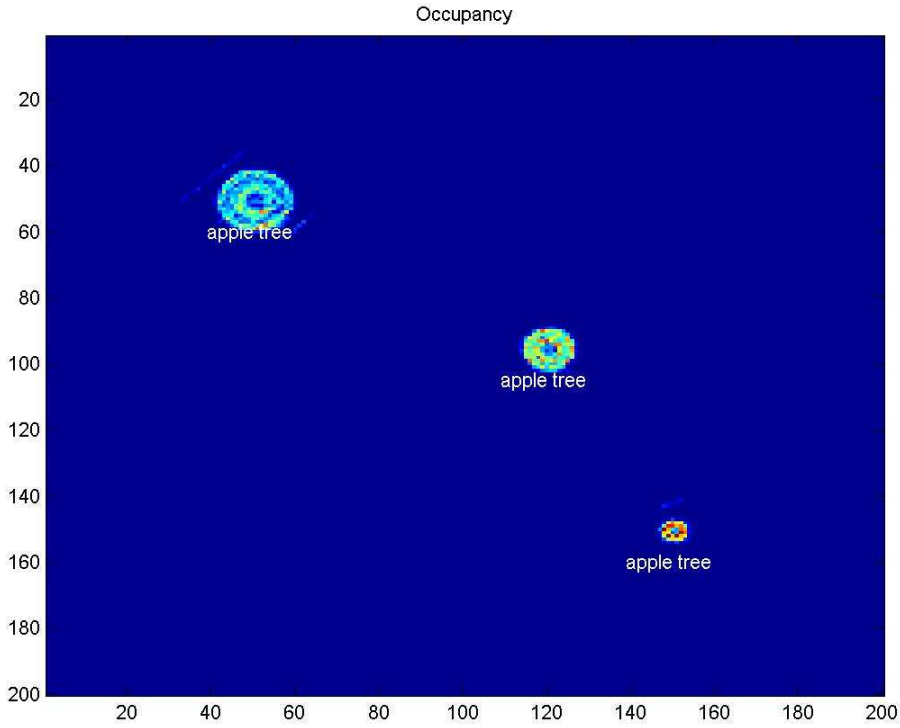

(c)

Figure 32 continued

The parameters used in our program are listed in the following table. Parameter names, purposes and default values are listed in the successive columns from left to right. These parameters are kept the same in all cases of map construction. A global world coordinate system is assumed and the virtual world is centered at the center of the world coordinate system. Virtual world is divided into grids of size GridSize in world units in each dimension. The size of the stereo images rendered from the virtual world is ImWidth by ImHeight pixels and kept the same through out the process of map construction. Distance between stereo camera pairs (BaseLine in world units), focal length of the cameras (FocalLength in world units), field of view (FOV degrees), the nearest distance cameras can see (Near in world units) and the

farthest distance (Far in world units) are the camera parameters initialized at the beginning of each map construction. MaxDisparity, MinDisparity and RowPermission all in pixels are the limits of search space for disparity.

While the agent explores the environment, it keeps a distance of ObjectClearance in world unit between the closest object in the view and itself. Also the same distance is kept while turning around an object. The agent turns around the object with ObjectTurnAngle degrees at each step of turn, and turns around itself with RobotTurnAngle degrees at each step of turn.

After completing a full turn around an object, the point cloud belonging to the object is thresholded by CountThreshold and the grids which have higher values are selected and considered for the recognition step. Object is segmented into two partsin terms of proximity and color similarity, where hue channel similarity is enough in most cases and the ColorThreshold_Hue is the similarity threshold used.

Table 4 Parameters used in the program.

Name of the parameter	**Purpose**	**Default value**
ImWidth	Image width	256
ImHeight	Image height	256
WorldX	Size of the virtual world in x direction	200
WorldY	Size of the virtual world in y direction	200
WorldZ	Size of the virtual world in z direction	30
GridSize	Size of a single world grid in terms of world meters	1
BaseLine	Distance between stereo cameras	0.3
FocalLength	Focal length of the cameras	0.1
FOV	Field of View	80º
Far	The farthest distance seen by the cameras	100
Near	The nearest distance seen by the cameras	0.1
MaxDisparity	Maximum disparity search limit in epipolar direction	20
MinDisparity	Minimum disparity search limit in epipolar direction	-10
RowPermission	Search limit in the direction vertical to epipolar direction	1
CountThreshold	The grid value threshold in order to be considered as occupied	5
ColorThreshold_Hue	Hue similarity threshold	7.0
ColorThreshold_saturation	Saturation similarity threshold	0.15
ColorThreshold_value	Value similarity threshold	0.15
ObjectTurnAngle	Amount of turn around the object at each step	40º
RobotTurnAngle	Amount of turn around the robot itself at each step	45º
ObjectClearance	Distance kept between the robot and the object	10

CHAPTER 5

CONCLUSION

In this study a human-like disparity estimation algorithm for the purpose of depth extraction is developed. Then this stereo vision system is applied to construct a world centric, grid based cognitive map which is very important for higher vertebrate survey navigation. This is done in a 3D virtual environment by moving a virtual robot around the 3D objects of this virtual world. The future study is to apply the algorithm on a real robot in a natural environment.

Navigation could not be achieved unless distance information is obtained. The most informative, natural and cheapest sensors for depth extraction are stereo or multiple cameras. With some processing on the images obtained by cameras, not only distance but other information such as color, texture, shape, motion, etc. can be obtained as well. And this brings the effort to include cameras as sensors to recent robotic applications although extraction of information from multiple images is very hard. By this way, a robot can simultaneously navigate, avoid obstacles, recognize objects around, perform some very special tasks just like humans do when at least a stereo camera pair is used as sensors. The final goal of many studies is to come up with a system which functions as humans do. Thus a vision model which is similar to human vision system would be very appropriate in order to perform many tasks simultaneously in a parallel manner.

In this study, a disparity algorithm which is based on multi-scale phase similarity of edges between corresponding feature points is developed. Sparse algorithms are

very important because before a dense analysis, at least in order to calibrate cameras, sparse feature matching is needed. Also, for 3D reconstruction and many robotic applications feature based methods work very well. In this study, features and their orientation information are extracted from stereo image pairs by steerable filters inspired from biological model of human cortical hyper-column structure where responses to filters at various orientations are stored. Thus, instead of calculating disparities using oriented filters and pooling the results over different orientations, a single orientation for each feature is obtained prior to disparity computation. The steerable filter estimate of stimulus orientation found using this method is very accurate given the small number of filters used.

Although the feature points are sparse, since features are extracted using a multi-scale strategy and they are the points of high contrast edges that define the bounding contours of objects, they prove to be highly informative. Correspondences between feature points are located using multi-scale phase information. This idea is biologically grounded. The reason for this is that simple binocular cells occur in pairs that are in quadrature phase. Besides, phase is very sensitive to position differences hence it provides fine image detail which is helpful in discriminating neighboring image regions and also is stable to geometric, lighting and very small scale deformations. However phase may not be stable for large scale deformations. There are image locations where phase is singular and can not be reliably used. Such points are the locations where local frequencies are very different from the filter tuning. Using multi-scale and including magnitude in matching algorithms bring good results in matching images with scale deformations. In this study, phase comparison is done at multiple scales and confidence weighting is used to augment phase information with information concerning the magnitude of the steerable filtered image to improve the correspondence method. Since phase-based stereo methods are not good in textureless regions but only good at boundaries, using multi-scale phase information at sparse feature points and using magnitude as confidence provide a highly trustable disparity information at feature points only.

Two routes to locating feature-point correspondences are explored. Using the position shift model, rough disparity values are obtained and a large range of disparities can be calculated, but to a limited accuracy. Using the phase shift model, fine tuning is performed without encountering the quarter cycle limit. This tuning scheme also allows a continuum of disparity estimates to be obtained.

In the future studies, post processing will be performed on the disparity values in order to get rid of spikes and discontinuities. Also, surface fitting will be applied to sparse disparity results in order to obtain dense disparity. This will provide a tool for image segmentation when color and disparity are used together.

Also, a probabilistic algorithm for correspondence matching is proposed. Mixture of von Mises distributions are used to model probabilistic matching algorithm using phase differences obtained for a stereo image pair and the model is verified on other stereo pairs. Thus, it can be concluded that multi-scale phase similarity is a good measure for sparse feature matching problems. In the future studies, more number of stereo pairs will be used as training set in modeling our algorithm probabilistically which will increase the success rate.

Finally, our stereo vision algorithm is applied in a simulated world. In this world there is a virtual robot (agent) which has a stereo imaging system modeled with the properties of human eye. There are also 3D objects which are made of simple shapes such as sphere, cone, cylinder, etc. In our study, the agent explores its environment based on some heuristics and simultaneously builds a 3D map and recognizes the objects it observes during exploration. The task of generating robot motion in the pursuit of building a map is commonly referred to as robotic exploration. While optimal robot motion is relatively well-understood in fully modeled environments, exploring robots have to cope with partial and incomplete models. Hence, any viable exploration strategy has to be able to accommodate contingencies and surprises that might arise during map acquisition. For this reason, exploration is a challenging planning problem, which is often solved sub-optimally via simple heuristics. In future studies, more complex objects will be used in our

virtual world and our virtual world will include natural effects such as lighting, background, shadow ect.

In the future studies, our exploration strategy will be expanded and our complete system will be applied on real robots. In that case simultaneous localization and mapping, ego-motion extraction problems will also be studied. All these problems are very closely related to stereo matching and with some slight changes on our algorithm we would be able to provide results for these problems also. Our final goal is to have a system where obstacle avoidance, map construction, localization, ego-motion extraction, object recognition and 3D reconstruction are done simultaneously. Also auto focusing which is very important for calibration and deciding on search space will be investigated.

In our study we only used world-centric coordinate system. However, human can prefer ego-centric or world-centric coordinate system with respect to the task performed. Thus, using ego-centric and world-centric together according to task is an other future study.

REFERENCES

[1] Anzai, A., Ohzawa, I., Freeman, R. D., Neural mechanisms for encoding binocular disparity: Receptive field position vs. phase. Journal of Neurophysiology, vol. 82, no. 2, pp. 874-890, 1999.

[2] Anzai, A., Ohzawa, I., Freeman, R. D., Neural mechanisms for processing binocular information: I. Simple cells. Journal of Neurophysiology, vol. 82, no. 2, pp. 891-908, 1999.

[3] Anzai, A., Ohzawa, I., Freeman, R. D., Neural mechanisms for processing binocular information: II. Complex cells. Journal of Neurophysiology, vol. 82, no. 2, pp. 909-924, 1999.

[4] Baker, S., Szeliski, R., Anandan, P., A layered approach to stereo reconstruction, Proc. of CVPR98, pp. 434-441, 1998.

[5] Baluja, S., Pomerleau, D. A., Expectation based selective attention for visual monitoring and control of a robot vehicle. Robotics and Autonomous Systems 22, pp. 329-344, 1997.

[6] Bishop, C. M., Neural Networks for Pattern Recognition. Oxford University Press, 1995.

[7] Blake, R., Wilson, H.R., Neural models of stereoscopic vision. Trends in Neuroscience, vol. 14, no. 10, pp.445-452, 1991.

[8] Carneiro, G., Jepson, A.D., Phase-based local features. In ECCV2002, pp. 282-296, Copenhagen, Denmark, May 2002.

[9] Carneiro, G., Jepson, A.D., Multi-scale phase-based local features. In CVPR, pp. 736-743, Madison, WI, USA, June 2003.

[10] Cartwright, B. A., Collett, T. S., Landmark learning in bees. Journal of Computational Physiology A 151, pp.521-543, 1983.

[11] Coombs, D., Roberts, K., Centering behavior using peripheral vision. Proceedings of IEEE Conference on Computer Vision and Pattern Recognition, IEEE Computer Society Press, Los Alamitos, CA, pp. 440-451, 1993.

[12] Cox, I., Hingorani, S., Rao, S., A maximum likelihood stereo algorithm. Computer Vision and Image Understanding, vol. 63, no. 3, May 1996.

[13] Daugman, J., Uncertainity relation for resolution in space, spatial frequency and orientation optimized by two dimensional visual cortical filters. Journal of the Optical Society of America 2, pp. 1160-1169, 1985.

[14] Davison, A. J., Murray, D. W., Simultaneous localization and map building using active vision, IEEE transactions on Pattern Analysis and Machine Intelligence, vol. 24, no. 7, pp. 865-880, July 2002.

[15] DeAngelis, G., Seeing in three dimensions: the neurophysiology of stereopsis. Trends in Cognitive Science, vol. 4, no. 3, s. 80-89, 2000.

[16] DeSouza, G. N., Kak, A.C., Vision for mobile robot navigation: A Survey. IEEE Transactions on Pattern Analysis and Machine Intelligence, vol. 24, no. 2, pp. 237-267, 2002.

[17] Elder, J. H., Zucker, S. W., Locale scale control for edge detection and blur estimation. IEEE PAMI, 20 (7), pp. 699-716, 1998.

[18] Erol, A., Automatic Fingerprint Recognition. Ph.D. Thesis, Middle East Technical University, Electrical and Electronics Department, Ankara, Turkey, 2001.

[19] Erwin, E., Miller, K. D. The subregion correspondence model of binocular simple cells. Journal of Neuroscience 19, pp. 7212-7229, 1999.

[20] Fischler, M. A., Bolles, R. C., Random sample consensus: a paradigm for model fitting with application to image analysis and automated cartography. Communication Association and Computing Machine, 24 (6), pp. 381-395, 1981.

[21] Fleet, D., Measurement of Image Velocity. Kluwe Academic Publishers, 1992.

[22] Fleet, D. J., Wagner, H.,Heeger, D. J., Neural encoding of binocular disparity: Energy models, position shifts and phase shifts. Vision Research, vol. 36, no. 12, pp. 1839-1857, 1996.

[23] Franz, M.O., Schölkopf, B., Mallot, H. A., Bülthoff, H. H., Leaning view graphs for robot navigation. Autonomous Robots, 5, pp. 111-125, 1998.

[24] Franz, M. O., Mallot, H. A., Biomimetic robot navigation. Robotic and Autonomous Systems, 30, pp. 133-153, 2000.

[25] Freeman, R. D., Ohzawa, I., On the neurophysiological organization of binocular vision. Vision Research, vol. 30, no. 11, pp. 1661-1676, 1990.

[26] Freeman, W. T., The design and use of Steerable Filters. IEEE Trans. Pattern Analysis and Machine Intelligence, 13(9), 1991.

[27] Fröhlinghaus, T., Buhmann, J. M., Regularizing phase-based stereo. International Conference on Pattern Recognition, ICPR96, pp. 451-455, Vienna, 1996.

[28] Fua, P., Leclerc, Y. G., Using 3D meshes to combine image-based and geometry-based constraints. In ECCV94, pp. B:281-291, 1994.

[29] Fua, P., From multiple stereo views to multiple 3-D surfaces. International Journal of Computer Vision, 24 (1):19-35, 1997.

[30] Gaussier, P., Joulain, C., Zrehen, S., Revel, A., Visual navigation in an open environment without map. Proc. IEEE Int'l Conf. Intelligent Robots and Systems, pp. 545-550, Sept. 1997.

[31] Gaussier, P., Lepretre, S., Joulain, C., Revel, A., Quoy, M., Banquet, J. P., Animal and robot learning: experiments and models about visual navigation. In Seventh European Workshop on Learning Robots- EWLR'98, Edinburgh, UK, 1998.

[32] Georgopoulos, A. P., Schwarz, A. B., Kettner, R. E., Neural population coding of movement direction. Science 233, pp. 1416-1419, 1986.

[33] Grimson, W. A computer implementation of a theory of human stereo vision. Royal, B-292:217-253, 1981.

[34] Harris, C., Determination of ego-motion from matched points. Proc. Alvey Vision Conf., 1987.

[35] Harris, C., Stephens, M., A combined corner and edge detector. In Alvey Vision Conference, pp. 147-151, 1988.

[36] Hüber, S. A., Bülthoff, H. H., Simulation and robot implementation of visual orientation behaviors of flies. In: Pheifer, R., Blumberg, B., Meyer, J. A., Wilson, S. W. (Eds.), From Animals to Animats 5, Proceedings of SAB'98, MIT Press, Cambridge, MA, pp.77-85, 1998.

[37] Jenkin, M. R. M., Jepson, A. D., Recovering local surface structure through local phase difference measurements. CVGIP: Image Understanding, vol. 59, no. 1, pp. 72-93, 1994.

[38] Jepson, A. D., Fleet, D. J., Scale space singularities. Lecture Notes in Computer Science, vol. 427, pp. 50-55, 1990.

[39] Jepson, A. D., Fleet, D. J., Phase singularities in scale space. Image and Vision Computing, vol. 9, no. 5, s. 338-343, 1991.

[40] Jones, D. G., Malik, J., Computational framework for determining stereo correspondence from a set of linear spatial filters. Image and Vision Computing, vol. 10, no. 10, pp. 699-708, 1992.

[41] Jerbic, B., Grolinger, K., Vranjes, B., Autonomous agent based on reinforcement learning and adaptive shadowed network. Artificial Intelligence in Engineering 13, pp. 141-157, 1999.

[42] Kagami, S., Okada, K., Inaba, M., Inoue, H., Design and implementation of on body real-time depth map generation system. Proceedings of the 2000 IEEE International Conference on Robotics and Automation, San Francisco, CA, pp. 1441-1446, April 2000.

[43] Karakaş, H. I. Analytic Geometry.

[44] Kim, D., Nevatia, R., Symbolic navigation with a generic map. Proc. IEEE Workshop Vision for Robots, pp. 136-145, Aug. 1995.

[45] Kundur, S. R., Raviv, D., Active vision based control schemes for autonomous navigation tasks. Pattern Recognition 33, pp. 295-308, 2000.

[46] Lee, S. H., Park, J. I., Lee, C. W., A new stereo matching algorithm based on Bayesian model. Proc. IEEE ICASSP98, pp. 2769-2772, 1998.

[47] Leloğlu, U. M., Halıcı, U., Multi-image region growing for integrating disparity maps. In Franc Solina and Ales Leonardis, editors, Computer Analysis of Images and Patterns, CAIP99, pp. 403-410, Slovenia, 1999.

[48] Leven, P., Hutchinson, S., Burschka, D., Farber, G., Perception based motion planning for indoor exploration, Prooceedings of the 1999 IEEE International Conference on Robotics and Automation, Detroit, Michigan, pp. 695-701, May 1999.

[49] Li, G., Svensson, B., Navigation with a focus directed mapping network. Autonomous Robots 7, pp. 9-30, 1999.

[50] Lowe, D.G., Three-dimensional object recognition in it cortex. In First IEEE International Workshop on Biologically Motivated Computer Vision, pg. 20-31, Seoul, Korea, May 2000.

[51] Ludtke, N., Wilson, R. C., Hancock, E. R., Tangent fields from population coding. Lecture Notes in Computer Science, vol. 1811, pp. 584-593, 2000.

[52] Marr, D., Poggio, T., A computational theory of human stereo vision. Proceedings of the Royal Society of London, B207, pp. 187-217, 1979.

[53] Marshall, J. A., Burbeck, C. A., Ariely, D., Occlusion edge blur: a cue to relative visual depth. Journal of the Optical Society of America, 1996.

[54] Mataric, M. J., Navigation with a rat brain: A neurobiologically inspired model for robot spatial representation. In: Meyer, J. A., Wilson, S. W. (Eds.), Form Animals to Animats, MIT Press, Cambridge, MA, 1991.

[55] Matsumoto, Y., Inaba, M., Inoue, H., Visual navigation using view-sequenced route representation. Proc. IEEE Int'l Conf. Robotics and Automation, vol. 1, pp. 83-88, Apr. 1996.

[56] Mayhew, J. E. W., Frisby, J. P. , Psychophysical and computational studies towards a theory of human stereopsis. Artificial Intelligence, vol. 17, pp. 349-385, 1981.

[57] Medioni, G., Nevatia, R. Segment-based stereo matching. CVGIP, 31(1), pp.2-18, 1985.

[58] Meng, M., Kak, A. C., Mobile robot navigation using neural networks and nonmetrical environment models. IEEE Control Systems, pp. 30-39, Oct. 1993.

[59] Moallem, P., Faez, K., Haddadnia, J., Reduction of the search space region in the edge based stereo correspondence. VMV, pp. 149-152, 2001.

[60] Moravec, H. P., Elfes, A., High resolution maps from angle sonar. In IEEE International Conference on Robotics and Automation, pp. 116-121, 1985.

[61] Murray, D., Little, J., Using real-time stereo vision for mobile robot navigation. Prooceedings of the IEEE Workshop on Perception for Mobile Agents, Santa Barbara, CA, June 1998.

[62] Mülayim, A. Y., 3D Reconstruction of Rigid Objects from Multiple Calibrated Views. Ph.D. Thesis, METU, Ankara, Turkey, 2003.

[63] Myers, R., Wilson, R. C., Hancock, E.R., Bayesian graph edit distance. Image Analysis and Processing, Venice, Italy, pp. 1166-1171, 1999.

[64] Nelson, R.C., Memory based recognition for 3-d objects. In ARPA Image Understanding Workshop, pg. 1305-1310, Palm Springs, USA, February 1996.

[65] Nourbakhsh, I. R., Andre, D., Tomasi, C., Genesereth, M. R., Obstacle avoidance via depth from focus, ARPA Image Understanding Workshop 1996.

[66] Ohya, A., Kosaka, A., Kak, A., Vision based navigation by a mobile robot with obstacle avoidance using single camera vision and ultrasonic sensing. IEEE Transactions on Robotics and Automation, vol. 14, no. 6, December 1998.

[67] Ohzawa, I., DeAngelis, G. C., Freeman, R. D., Stereoscopic depth discrimination in the visual cortex: Neurons ideally suited as disparity detectors. Science, vol. 249, no. 4972, pp. 1037-1041, 1990.

[68] Ohzawa, I., Mechanisms of stereoscopic vision: the disparity energy model. Current Opinion in Neurobiology 8, pp. 509-515, 1998.

[69] Okada, K., Kino, Y., Kanehino, F., Kuniyoshi, Y., Inaba, M., Inoue, H., Rapid development system for humanoid vision-based behaviours with real-virtual common interface. Proceedings of the International Conference on Intelligent Robotics and Systems, Laussanne, Switzerland, Oct 2002.

[70] Olson, C. F., Subpixel localization and uncertainty estimation using occupancy grids. Proceedings of the 1999 IEEE International Conference on Robotics and Automation, Detroit, Michigan, pp. 1987-1992, May 1999.

[71] Olson, C. F., Maximum likelihood image matching. IEEE Transactions on Pattern Analysis and Machine Intelligence, vol. 24, no 6, pp. 853-857, 2002.

[72] Pentland, A. P., A new sense of depth of field. IEEE Trans. On Pattern Analysis and Machine Intelligence, vol. PAMI-9, no 3, pp. 523-531, 1987.

[73] Perez, J.A., Castellanos, J. A., Montiel, J. M. M., Neira, J., Tardos, J. D., Continuous mobile robot localization: Vision vs. Laser, Proceedings of the 1999 IEEE International Conference on Robotics and Automation, Detroit, Michigan, pp. 2917-2923, May 1999.

[74] Pollard, S. B., Mayhew, J. E. W., Frisby, J. P., PMF: A stereo correspondence algorithm using a disparity gradient limit. Perception, vol. 14, pp. 449-470, 1985.

[75] Prescott, T. J., Spatial representation for navigation in animats. Adaptive Behaviour, 4(2), pp. 85-123, 1996.

[76] Qian, N., Computing stereo disparity and motion with known binocular cell properties. Neural Computation, vol. 6, no. 3, pp. 390-404, 1994.

[77] Qian, N., Zhu, Y., Physiological computation of binocular disparity. Vision Research, vol. 37, no. 13, s. 1811-1827, 1997.

[78] Qian, N., Relationship between phase and energy methods for disparity computation. Neural Computation, 12, pp. 279-292, 2000.

[79] Quoy, M., Laroque, P., Gaussier, P., Learning and motivational couplings promote smarter behaviors of an animate in an unknown world. Robotics and Autonomous Systems 38, pp. 149-156, 2002.

[80] Rabie, T. F., Terzopoulos, D., Stereo and color analysis for dynamic obstacle avoidance. CVPR1998, pp. 245-252, 1998.

[80] Ramloll, R., Mowat, D., Way finding in virtual environments using an interactive spatial cognitive map. In IV2001 Proceedings, IEEE Press, pp. 574-583, 2001.

[81] Recce, M., Harris, K. D., Memory of places: A navigational support of Marr's theory of hippocampal function. Hippocampus 6, pp. 735-748, 1996.

[82] Robert, L., Faugeras, O. Curve-based stereo: Figural continuity and curvature. In IEEE Conference on Computer Vision and Pattern Recognition, pp. 57-62, 1991.

[83] Rogers, D. F., Adams, J. A., Mathematical Elements for Computer Graphics. Second Eddition, McGraw-Hill International Editions, 1990.

[84] Sanger, T. D., Stereo disparity computation using Gabor filters. Biol. Cybern., 59, pp. 405-418, 1988.

[85] Scharstein, D., Szeliski, R., A Taxonomy and evaluation of dense two-frame stereo correspondence algorithms. International Journal of Computer Vision, 47 (1/2/3), pp. 7-42, April-June 2002.

[86] Schmid, C., Mohr, R., Local gray value invariants for image retrieval. IEEE Transactions on Pattern Analysis and Machine Intelligence, 19(5):530-535, 1997.

[87] Schmitt, M., Rous, M., Matsikis, A., Kraiss, K. F., Vision-based self-localization of a mobile robot using a virtual environment. Proceedings of the International Conference on Robotics and Automation, Detroit, Michigan, pp. 2911-2916, May 1999.

[88] Schölkopf, B., Mallot, H., View-based cognitive mapping and path planning. Adaptive Bahavior, 3, pp. 311-348, 1995.

[89] Se, S., Lowe, D., Little, J., Vision-based mobile robot localization and mapping using scale-invariant features. Proceedings of the 2001 IEEE International Conference on Robotica and Automation, Seoul, Korea, pp.2051-2058, May 2001.

[90] Terzopoulos, D., Rabie, T. F., Animat vision: Active vision in artificial animals. Journal of Computer Vision Research, pp. 2-19, September, 1997.

[91] Thrun, S., Learning metric-topological maps for indoor mobile robot navigation. Artificial Intelligence, 99 (1), pp. 21-71, 1998.

[92] Thrun, S., Learning occupancy grids with forward models. Proceedings of the 2001 IEEE/RSJ International Conference on Intelligent Robots and Systems, Mani, Hawaii, USA, pp.1676-1681, Oct.29-Nov. 03, 2001.

[93] Torr, P.H.S., Zisserman, A., Feature-based methods for structure and motion estimation. In Vision Algorithms: Theory and Practice, pg. 278-294, Corfu, Greece, September 1999.

[94] Tunçer, F., Image Synthesis for Depth Estimation Using Stereo and Focus Analysis. M.Sc. Thesis, Department of Electrical and Electronics Engineering, Middle East Technical University, Ankara, Turkey, 2002.

[95] Vincent, E., Laganiere, R., Matching feature points in stereo pairs: A comparative study of some matching strategies. Int. Journal of Machine Graphics and Vision, vol. 10, no. 3, pp. 237-259, 2001.

[96] Vogels, R., Population coding of stimulus orientation by striate cortical cells. Biological Cybernetics, 64, pp. 25-31, 1990.

[97] Voicu, H., Schmayuk, N., Three dimensional cognitive mapping with a neural network. Robotic and Autonomous Systems 35, pp. 23-36, 2001 .

[98] Wolf, J., Burgard, W., Burkhardt, H., Robust vision-based localization for mobile robots using an image retrieval system based on invariant features. Proceedings of the 2002 IEEE International Conference on Robotics and Automation, Washington, DC, pp. 359-365, May 2002.

[99] Zucker, S., Early orientation selection: Tangent fields and the dimensionality of their support, Comp. Vis., Graph., and Image Process., 32, pp. 74-103, 1985.

APPENDIX A

DEPTH PERCEPTION IN HUMAN VISUAL SYSTEM

The visual system makes use of a variety of cues to help judge the distance of objects. These cues can be classified mainly into two groups:

- Monocular (pictorial) cues
- Binocular cues

A.1 Pictorial Depth Cues

Our perception of the relative depth, or distance from the viewpoint, of the various objects in a static, two-dimensional image of a three-dimensional scene may be influenced to various extents by several different factors, which are sometimes referred to as pictorial cues to depth because of their use by artists to convey a greater sense of depth in a flat medium.

A.1.1 Occlusion (Interposition)

Probably the most important of the pictorial depth cues is occlusion, the obscuration of a portion of a more distant object's surface by another surface that is closer to the viewpoint. There is evidence that our visual system makes fundamental use of occlusion information to encode the relative depths of superimposed surfaces at a relatively early stage in visual processing, and that the occlusion boundaries are the

key elements in conveying the depth relationships. See Figure 33 for a illustration of occlusion.

Figure 33 An illustration showing the effect of occlusion

A.1.2 Linear Perspective

When we look through our eyes at the world, the three-dimensional information in the scene gets projected onto the two-dimensional surface of our retina. Mathematically, this transformation can be described by a perspective projection, a 3D-to-2D mapping that has several important features. The first of these is what is often referred to in the literature as “linear perspective” or the observation that lines which are parallel in the three-dimensional model will appear in the projected image to converge toward a single vanishing point as they recede into the distance. This phenomenon is illustrated in Figure 34. In general, the effect will be most pronounced when the lines originate close to the viewpoint and extend a considerable distance away.

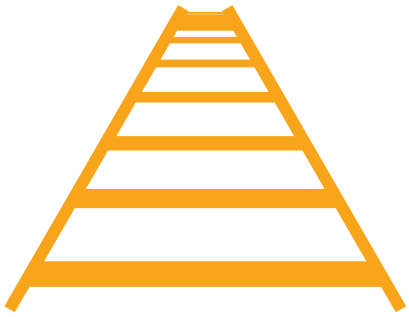

Figure 34 An illustration showing linear perspective

Parallel lines are obviously not the only lines whose relative orientations are “remapped” by a perspective projection, but the effects of perspective convergence may be most clearly represented by them. It becomes increasingly difficult to appreciate the “distortion” due to perspective projection when the represented objects are more distant from the viewpoint, have a more limited extent in depth, and are smoothly curving or of irregular or unfamiliar shape.

A perspective projection is clearly not the only possible 3D-to-2D mapping, and in some instances it has been argued that, for the purposes of representing certain types of information about a three-dimensional model, it is not necessarily the best type of mapping to use. A common alternative is to employ an orthographic projection, in which parallel lines remain parallel. Such projections can be somewhat easier to construct manually and interpret intellectually, and certain algorithms for generating images from three-dimensional models derive their computational efficiency from relying on the regularities inherent in this approach.

We are not constrained, when constructing a computer-generated image, to represent the data exactly as it would appear if it sat before us as a physical entity; however, it is important to consider both the advantages and disadvantages of stylizing the display.

A.1.3 Relative familiar size

A second consequence of perspective (but not orthographic) projection is that as an object moves farther away from the viewpoint it will subtend a smaller visual angle on the retina. This means that more distant objects will have relatively smaller projected sizes, and this is the basic premise behind the pictorial depth cue referred to as “relative familiar size”. Size is an ambiguous cue unless the physical size of the object is known.

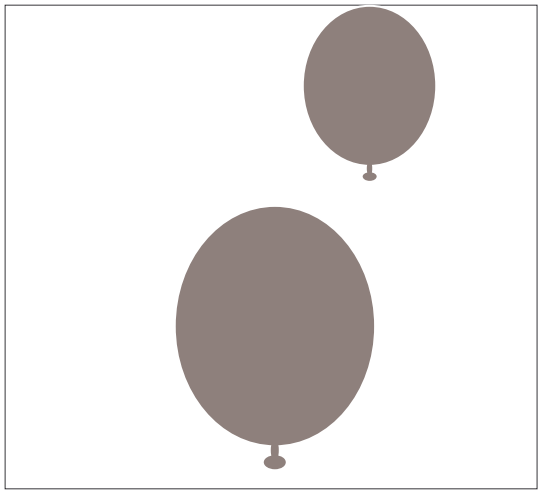

Figure 35 Relative size as a cue. Which one of the balloons looks closer?

A.1.4 Focus, Depth of Field and Accommodation

When we perceive objects in our everyday experience, we are rarely conscious of anything appearing to be “out of focus”. Under ordinary circumstances, when we direct our attention to an object we fixate it in our fovea and automatically adjust the lens of our eye to bring the object into focus. Because of the great disparity between the depth of field attainable by our visual system and the depth of field available with a camera, however, it is not at all uncommon to observe photographs in which some part of the image is blurred due to its distance in depth from the focal point.

Accommodation refers to the ability of the eye to change focus from distant to near objects.

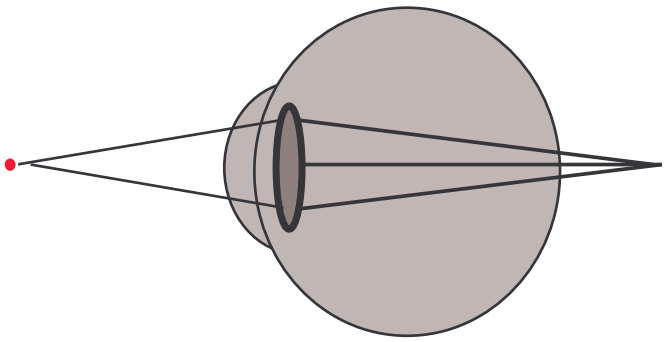

Figure 36 Accommodation. Blurred image.

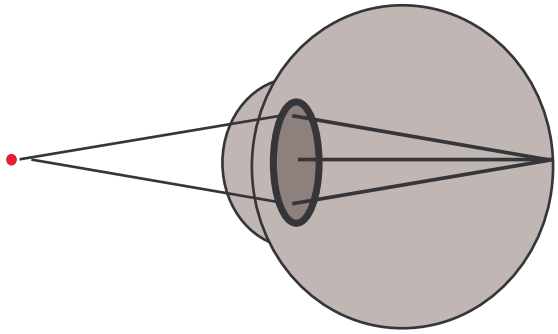

Figure 37 Accommodation. Focused image.

Experimental evidence substantiating the usefulness of focus as a depth cue was provided by [72], who performed experiments verifying that people perceived a greater separation in depth between overlapping objects in images in which there was a larger gradient of focus between them. Further support for the perceptual significance of focal differences can be drawn from experiments by other researchers, who found that when the separate parts of an ambiguously organized image were filled with sine wave gratings of two different spatial frequencies but equivalent contrasts, the region filled with the higher spatial frequency pattern was seen as figure (rather than ground) a significantly greater percentage of the time. Although there is generally not enough information available in a limited-depth-of-field image of two non-overlapping surfaces to determine the sign of the depth distance between them purely on the basis of focus information, [53] described how it should be theoretically possible for observers to disambiguate the depth order of overlapping textured surface on the basis of the amount of blur along the occluding edge, and conducted experiments verifying this hypothesis. (About half of the subjects in these experiments consistently judged the blurred half-plane to be closer when the occluding edge was blurred and the focused half-plane to be closer when the occluding edge was sharp; for the other half of the subjects this trend, while detectable, was fairly modest.)

A.2 Binocular disparity (Stereopsis)

When we look at a particular point in space with both of our eyes (which is the normal case in vision), the views perceived by each individual eye will be slightly different, because of their spatial separation in the head. The focal point will fall on corresponding locations in the retinal images of each eye, as will all other points that are equidistant from the viewpoint (defining a plane, called the horopter, of points in space that have zero retinal disparity in that view), but points that are closer or farther from the viewpoint than the fixation point will be mapped onto disparate locations in the two retinal images. Objects that are closer to the viewpoint (in front of the horopter) are seen in crossed disparity, while objects that are farther away are seen in uncrossed disparity. Our visual system is able to interpret the relative depths between two points in space from the amount of retinal disparity in their projections to each eye and to determine the depth order of these points from the sign (crossed or uncrossed) of this disparity, Figure 38 and Figure 39. Exactly how the two flat views are united in the brain to yield a unified perception of three-dimensional space has been a topic of considerable investigation.

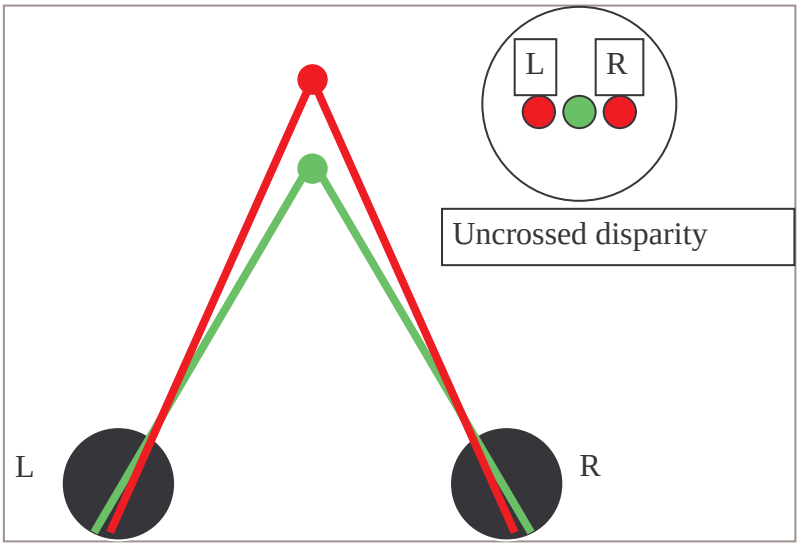

Figure 38 Uncrossed disparity

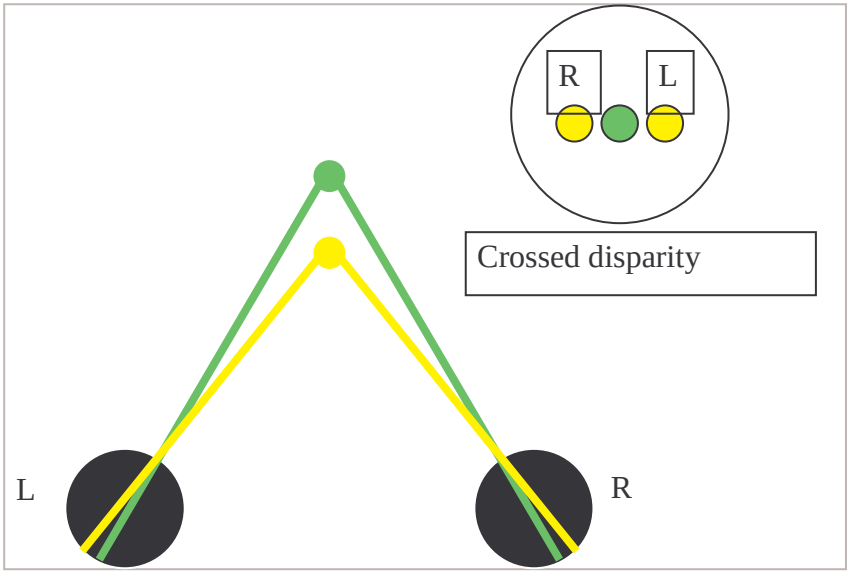

Figure 39 Crossed disparity

APPENDIX B

GEOMETRY FILE FORMAT

A sample geometry file listing with a few primitives is given below. The fields are self-explanatory as seen from the comment lines.

```
# Shader count
3

# Texture count
9

# Visual count
13

################################################################################
# SHADER 0
################################################################################

# Ambient color
1.0 1.0 1.0 1.0
# Diffuse color
1.0 0.0 0.0 0.0
# Specular color
1.0 0.0 1.0 0.0
# Emissive color
0.0 0.0 0.0 0.0
# Shininess [0,128]
50

################################################################################
# SHADER 1
################################################################################
```

 # Ambient color
0.0 0.0 1.0 1.0
 # Diffuse color
0.0 0.0 1.0 0.0
 # Specular color
1.0 1.0 1.0 1.0
 # Emissive color
0.0 0.0 0.0 0.0
 # Shininess [0,128]
50

##
 # SHADER 2
##

 # Ambient color
0.0 1.0 1.0 0.0
 # Diffuse color
1.0 0.0 1.0 0.0
 # Specular color
1.0 1.0 0.0 0.0
 # Emissive color
0.0 0.0 0.0 0.0
 # Shininess [0,128]
50

##
 # TEXTURE 0
##

textures/checker.tga
textures/wood.tga
textures/brick.tga
textures/grass.tga
textures/roof.tga
textures/sky.tga
textures/earth.tga
textures/cobra.tga
textures/bubinga.tga

##
 # VISUAL 0 - SPHERE TREE TOP - APPLE
##

 # Visual type
SPHERE

 # Center
10 12 20

 # Radius
4

 # Shader index
-1

 # Texture index
3

##
 # VISUAL 1 - TREE BODY - APPLE
##

 # Visual type
CYLINDER

 # RadiusBase
2

 # RadiusTop
2

 # Height
8

 # Slices
50

 # Stacks
30

 # Translation [x,y,z]
10 8 20

 # Rotation [x,y,z]
1 0 0

 # Shader index
-1

 # Texture index
1

##
 # VISUAL 2 - HAUSE
##

 # Visual type
CYLINDER

 # RadiusBase
7

 # RadiusTop
7

 # Height
7

 # Slices
70

 # Stacks
80

 # Translation [x,y,z]
20 7 -5

 # Rotation [x,y,z]
1 0 0

 # Shader index
-1

 # Texture index
2

##
 # VISUAL 3 - ROOF
##

 # Visual type
CYLINDER

 # RadiusBase
1

 # RadiusTop
7

 # Height
4

 # Slices
36

 # Stacks
50

 # Translation [x,y,z]
20 11 -5

 # Rotation [x,y,z]
1 0 0

 # Shader index

-1

 # Texture index
4

###
 # VISUAL 4 - SPHERE TREE TOP - APPLE
###

 # Visual type
SPHERE

 # Center
-10 12 -30

 # Radius
4

 # Shader index
-1

 # Texture index
3

###
 # VISUAL 5 - TREE BODY - APPLE
###

 # Visual type
CYLINDER

 # RadiusBase
2

 # RadiusTop
2

 # Height
8

 # Slices
50

 # Stacks
30

 # Translation [x,y,z]
-10 8 -30

 # Rotation [x,y,z]

1 0 0

 # Shader index
-1

 # Texture index
1

##
 # VISUAL 6 - TREE TOP - PINE
##

 # Visual type
CYLINDER

 # RadiusBase
1

 # RadiusTop
8

 # Height
8

 # Slices
36

 # Stacks
20

 # Translation [x,y,z]
-10 16 -5

 # Rotation [x,y,z]
1 0 0

 # Shader index
-1

 # Texture index
3

##
 # VISUAL 7 - TREE BODY - PINE
##

 # Visual type
CYLINDER

 # RadiusBase
2

 # RadiusTop
2

 # Height
8

 # Slices
36

 # Stacks
20

 # Translation [x,y,z]
-10 8 -5

 # Rotation [x,y,z]
1 0 0

 # Shader index
-1

 # Texture index
1

##
 # VISUAL 8 - TREE TOP - PINE
##

 # Visual type
CYLINDER

 # RadiusBase
1

 # RadiusTop
8

 # Height
8

 # Slices
36

 # Stacks
20

 # Translation [x,y,z]
-40 16 -30

 # Rotation [x,y,z]
1 0 0

 # Shader index
-1

 # Texture index
3

##
 # VISUAL 9 - TREE BODY - PINE
##

 # Visual type
CYLINDER

 # RadiusBase
2

 # RadiusTop
2

 # Height
8

 # Slices
36

 # Stacks
20

 # Translation [x,y,z]
-40 8 -30

 # Rotation [x,y,z]
1 0 0

 # Shader index
-1

 # Texture index
1

##
 # VISUAL 10 - SPHERE TREE TOP - APPLE
##

 # Visual type
SPHERE

 # Center
-40 12 5

 # Radius
4

 # Shader index
-1

 # Texture index
3

##
 # VISUAL 11 - TREE BODY - APPLE
##

 # Visual type
CYLINDER

 # RadiusBase
2

 # RadiusTop
2

 # Height
8

 # Slices
50

 # Stacks
30

 # Translation [x,y,z]
-40 8 5

 # Rotation [x,y,z]
1 0 0

 # Shader index
-1

 # Texture index
1

##
 # VISUAL 12 - GROUND
##

 # Visual type
POLYGON

 # Enable back face culling
1

 # Shader index
1

```
# Texture index
-1

# Vertex count
4

# Vertex data
# x y z r g b a tu tv
-500 0 -500    0.5 0.5 0.0 0.0      0 0
-500 0 500     0.5 0.5 0.0 0.0      3 0
500 0 500    0.5 0.5 0.0 0.0      3 3
500 0 -500   0.5 0.5 0.0 0.0      0 3
```

APPENDIX C

A SAMPLE CAMERACONTROLLER PLUGIN

CameraController.h

```
#ifndef __CAMERACONTROLLER_H
#define __CAMERACONTROLLER_H

#include "Simulation.h"

class CCameraController
{

public:

   virtual ~CCameraController() {}

   virtual char *GetInfo() { return "Default Camera Controller"; }
   virtual char *GetResult() { return "Default result"; }

   virtual void Tick() = 0;
   virtual void SetSimulation( CSimulation *pSimulation ) = NULL;
};

#endif
```

BasicCameraController.cpp

```
#include "../CameraController.h"

#define _PLUGIN_EXPORT __declspec( dllexport )

//////////////////////////////////////////////////////////////////////////////

class CBasicCameraController : public CCameraController
{

public:
```

```
    CSimulation *m_pSimulation;

    float m_fTime;

public:

    CBasicCameraController()
    {
        m_pSimulation = NULL;
        m_fTime = 0.0f;
    }

    virtual char *GetInfo() { return "Basic Camera Controller\x0d\x0aWritten by Fahri Tuncer"; }
    virtual char *GetResult() { return "No result"; }

    virtual void Tick();

    virtual void SetSimulation( CSimulation *pSimulation )
    {
        m_pSimulation = pSimulation;
    }
};

////////////////////////////////////////////////////////////////////////////////

// extern "C" __declspec (dllexport) void* __stdcall CreateInstance()
extern "C" __declspec (dllexport) void *CreateInstance()
{
    return new CBasicCameraController();
}

////////////////////////////////////////////////////////////////////////////////

void CBasicCameraController::Tick()
{
    float campos[3] = { 3.0f, 1.0f, 3.0f };

    campos[0] = 3.0f * cosf( m_fTime );
    campos[1] = 2.0f * cosf( m_fTime );
    campos[2] = 3.0f * sinf( m_fTime );

    m_pSimulation->SetCameraPos( campos );

    m_fTime += 0.1f;
}
```

APPENDIX D

C++ SCRIPT FOR RGB TO HSV CONVERSION

```
// r,g,b values are from 0 to 1
// h = [0,360], s = [0,1], v = [0,1]
//if s == 0, then h = -1 (undefined)
void RGBtoHSV( float r, float g, float b, float *h, float *s, float *v )
{
	float min, max, delta;
	min = MIN( r, g, b );
	max = MAX( r, g, b );
	*v = max;				// v
	delta = max - min;
	if( max != 0 )
		*s = delta / max;		// s
	else {
		// r = g = b = 0		// s = 0, v is undefined
		*s = 0;
		*h = -1;
		return;
	}
	if( r == max )
		*h = ( g - b ) / delta;		// between yellow & magenta
	else if( g == max )
		*h = 2 + ( b - r ) / delta;	// between cyan & yellow
	else
		*h = 4 + ( r - g ) / delta;	// between magenta & cyan
	*h *= 60;				// degrees
	if( *h < 0 )
		*h += 360;
}
```